UNIVERSITY OF CALIFORNIA, MERCED

INHOMOGENEOUS STRUCTURES OF ATOMIC MIXTURES IN BOX POTENTIALS

A dissertation
submitted in partial fulfillment of the requirements for the degree of
Doctor of Philosophy

by
Bishal Parajuli
2023

PhD committee members

Professor Kevin Mitchell, Chair

Professor Chih-Chun Chien

Professor Michael Scheibner

Professor Kinjal Dasbiswas

Bishal Parajuli's dissertation has been approved, and it meets the necessary quality and format standards for publication in both microfilm and electronic formats.

Chih-Chun Chien

Michael Scheibner

Kinjal Dasbiswas

Kevin Mitchell, Chair

University of California, Merced

2023

INHOMOGENEOUS STRUCTURES OF ATOMIC MIXTURES IN BOX POTENTIALS

Bishal Parajuli, Ph.D.

University of California, Merced 2023

Due to phenomenal progress in trapping and cooling of cold atoms, ultracold atoms has been a successful platform for studying fundamental physics and simulating quantum many-body systems with the advantage of tuning the parameters in real space. In this dissertation, we theoretically investigated inhomogeneous structures of different ultracold atomic mixtures in quasi-one-dimensional box potentials to explore the rich phases of atomic mixtures. The realization of uniform box potentials in experiments allows us to study inhomogeneous structures, phase diagrams and interface structures in various atomic mixtures which arise from the competition between interaction energy and kinetic energy. The presence of real space constraints like box potentials or quenching of interactions permits the extraction of characteristic length scale of the systems. We examined the characteristic lengths of spatial change such as, the healing lengths in the case of boson-fermion mixtures and correlation lengths in the case of superfluid-normal phase transition. The analyses of the healing lengths at the boson-fermion interface confirms the energy competition mechanism behind the phase-separation structures. We modelled spatially tunable inhomogeneous interactions for attractive Fermi gases to study analogs of the proximity effect and the spatial Kibble-Zurek mechanism (KZM) in a unified framework. The introduction of inhomogeneity lead to the distortion of the order parameter which is characterized by the correlation length. We extracted the correlation lengths from the pair wavefunction and correlation function to determine the penetration of the order parameter in the region where interaction vanishes. In the setup resembling the proximity effect, we found that the correlation lengths follow the BCS coherence length while only the exponent from the pair correlation function agrees to the Kibble-Zurek scaling in the case of spatial KZM setup. We also extract the critical exponent by adding a uniform bosonic background to the attractive Fermi gases and found that it does not alter the scaling behavior in the miscible phase. With recent experimental progress in the field of atomic mixtures and box potentials, our results will characterize the density profiles, correlation lengths and scaling behavior of those multi-component quantum systems.

To, one and only supreme hero I have ever known, my mom

ACKNOWLEDGEMENTS

I would like to express my heartfelt gratitude to the following people who have supported me throughout my academic journey.

First and foremost, I would like to thank my family for their unwavering support and encouragement. Their love and belief in me have been my driving force, and I am immensely grateful for their sacrifices and understanding.

I would also like to thank my friends and relatives for their constant support and encouragement. Their words of encouragement and motivation have been a source of inspiration for me.

Finally, I would like to express my sincere appreciation to my advisor Dr. Chih-Chun Chien. His guidance, support, and expertise have been invaluable to me throughout my research. His mentorship has been instrumental in shaping my research skills and has helped me achieve my academic goals. I would like to express my deep gratitude to the members of my PhD committee for their invaluable suggestions and feedback throughout the course of my degree.

I would like to express my heartfelt appreciation to everyone who has been a part of my academic journey and has made invaluable contributions. I am particularly grateful to the National Science Foundation for their generous support of my research through Grant No. PHY-2011360. Thank you for believing in my work and providing the funding that has enabled me to pursue my academic goals.

TABLE OF CONTENTS

LIST OF TABLES

LIST OF FIGURES

CHAPTER 1

INTRODUCTION

Bosonic and fermionic atoms exhibit distinct quantum mechanical properties that result from their intrinsic characteristics. Bosons have integer spins and obey Bose-Einstein statistics, which allow any number of identical bosons to occupy the same quantum state [1]. Conversely, fermions have half-odd integer spins and follow Fermi-Dirac statistics, which prohibit two identical fermions from occupying the same quantum state due to the Pauli exclusion principle [2]. These statistical differences have significant implications for the collective behavior of bosons and fermions. For example, bosonic particles tend to condense into the same quantum state at low temperatures, resulting in phenomena like superfluidity and Bose-Einstein condensation (BEC) [3]. However, BEC and superfluidity are not always correlated, as an ideal BEC may not exhibit superfluidity and a two-dimensional superfluid may not exhibit BEC [4]. Nevertheless, there are many instances where BEC and superfluidity occur together, leading to fascinating and practical properties such as coherent flow and quantized vortices. On the other hand, fermionic particles obey the Pauli exclusion principle, which results in the formation of a Fermi sea at low temperatures, where each fermion occupies energy states below the Fermi energy E_f.

Einstein in 1924 theoretically predicted that upon cooling a gas of identical bosonic atoms below a certain temperature threshold T_c, a significant proportion of the bosons tend to condense into the lowest quantum mechanical energy state, resulting in a macroscopic condensate [1, 4]. In 1995 BEC was observed experimentally in a single-component atomic gas [5–7]. The results provided the strong evidence of BEC of atoms which was characterized by the single, coherent wavefunction. Additionally, the experiments demonstrated the importance of cooling techniques, such as laser cooling and evaporative cooling, in achieving the extremely low temperatures required for BEC. Overall, the 1995 BEC experiment was a landmark achievement in the field of physics, providing strong evidence for the existence of a fundamentally new state of matter and opening up new avenues for research and technological development.

Realization of BEC in experiments broadened the interest to explore systems with two or more condensates. One of the primary motivations for studying atomic mixtures is the ability to explore the behavior of interacting many-body systems. In ultracold atomic systems, mixtures of different atomic species can exhibit a wide range of interesting and complex phenomena, including phase separation [8], superfluidity [9], and quantum magnetism [10]. It is well known that superfluid mixtures ^{3}He-^{4}He exhibit phase separation at low temperatures [9] and similarly, two-component BEC of ^{87}Rb atoms show phase separation in the presence of inter-species interactions [8]. By manipulating the interac-

tions between ultracold atoms, one can induce phase separation in the mixtures, where distinct regions of different densities and phases emerge. This allows for the study of the behavior of quantum systems under extreme conditions, such as at low temperatures or high densities, which are difficult to achieve in other experimental setups.

Furthermore, condensates in atomic boson-boson mixtures [11] and BEC of molecules in two-component Fermi gases with adjustable interactions [12, 13] have been produced by experimental groups. Those experiments involved the exploration of two-component mixtures using two hyperfine states of the same species. Subsequently, fermionic atoms were mixed with bosonic atoms in several examples, including ^{7}Li–^{6}Li mixtures [14, 15], ^{23}Na–^{6}Li mixtures [16], ^{87}Rb–^{40}K mixtures [17–19], ^{87}Rb–^{6}Li mixtures [20], ^{87}Sr–^{84}Sr mixtures [21], ^{41}K–^{6}Li mixtures [22], and ^{133}Cs–^{6}Li mixtures [23]. In general, binary atomic boson-fermion mixtures with repulsive inter-species interactions demonstrate a bosonic BEC and a single-component normal Fermi gas since pairing mechanism is not involved.

The structures of atomic mixtures have been studied theoretically, taking into account confinement effects [24–27], such as hard-wall potentials [28, 29] and mass effects [30–39]. Phase separation in one-dimensional boson-fermion mixtures [40], repulsive two-component Fermi gases [41], and repulsive boson-fermion mixtures in harmonic traps [42, 43] have been studied. These investigations have revealed that the structure of atomic mixtures is influenced by inter- and intra-species interactions. Spatial separation occurs when bosons and fermions in a binary mixture repel each other, minimizing their overlapping region [42, 43], while attraction can lead to collapse [18, 19] or droplet formation [44, 45]. Previous studies on binary fermion mixtures have revealed that phase separation is not solely determined by repulsive interactions, but also by other factors such as population imbalance [46] and additional p-wave interaction [33]. It has been suggested that phase separation of fermion mixtures in the thermodynamic limit driven by large mass imbalances is possible in all dimensions, even in the weakly interacting regime [32]. Path integral formalism has been used to study the thermodynamics and structural transitions of binary atomic boson-fermion mixtures [47]. Recent experiments have also been conducted on various atomic mixtures [48–51] and many fascinating phenomena of one-dimensional atomic mixtures have been reviewed in Ref. [52]. Although a recent review [53] covered a broad range of few-body systems in harmonic traps, including mass-imbalanced systems, the effects of mass imbalance on the structures induced by hard-wall potentials have not been thoroughly explored for many-body systems.

In the realm of ultra-cold atoms, there exists a key difference between bosons and fermions. Ultra-cold atoms, typically charge neutral, primarily interact

through two-body collisions. However, the Pauli exclusion principle dictates that identical fermionic atoms cannot occupy the same quantum state, thereby preventing them from colliding and interacting through the dominant two-body s-wave interaction [1]. Additionally, the Fermi pressure, which is dependent nonlinearly on the fermion density and related to bulk kinetic energy, introduces another distinction between bosonic and fermionic mixtures [3]. In the case of fermionic mixtures, the phase-separation structure must balance the influences of interactions, confinement-induced kinetic energy, and the Fermi pressure. Previous examinations of fermionic mixtures in harmonically trapped gases have demonstrated strong agreement with experimental results [54, 55].

The history of superconductivity dates back to 1911, when Dutch physicist Heike Kamerlingh Onnes discovered the phenomenon while studying the properties of Mercury at low temperatures [56]. In 1957, John Bardeen, Leon Cooper, and Robert Schrieffer proposed the BCS theory [56], which explains the mechanism behind superconductivity in conventional superconductors by the formation of Cooper pairs. The requirement for the formation of Cooper pairs in attractive Fermi gases is that a mixture of two different hyperfine levels of the fermions must be trapped. Studies have been conducted on Fermi gases consisting of two components that exhibit attractive forces while being confined in different potentials. Cooper pair formation has been observed in harmonically trapped Fermi gases. These observations have been reported in [57, 58]. This phenomenon has enabled researchers to investigate the BCS phase transition, as described in [57]. Additionally, the effects of changing particle numbers and interaction strengths on harmonically trapped Fermi gases have also been studied using this observation, as detailed in [58]. In fermionic superfluids with uneven spin population, phase separation has been observed between normal and superfluid transitions [59,60]. Moreover, in fermionic cold atoms that are confined in a one-dimensional optical potential, two superfluid phases have been discovered: an unconfined BCS pairing phase and a confined molecular-superfluid phase [61]. Phase separation at unitarity and mass-imbalance effects for ultracold superfluid Fermi gases in harmonic and optical potentials is discussed in Review [62].

Conventionally, harmonic potentials have been used to trap ultracold atoms which leads to spatially inhomogeneous interactions, limits the interesting features to the narrow region of densities and suffer atom loss due to its infinite size. However, the box potential imposes uniform interaction in space and confines the atoms within a finite volume. Additionally, it can be easily implemented in numerical simulations and theoretical models, since they can be discretized into a finite number of grid points. BEC of bosonic atoms have been achieved in quasi-1D [63, 64], 2D [65], and 3D [66] box traps, while homogeneous 2D [67] and 3D [68] Fermi gases have been achieved for two-component fermions. With the recent experimental advancements in atomic mixtures and

box potentials, we investigate various atomic mixtures in box potentials to uncover the underlying physics.

With above mentioned experimental progress in the study of atomic mixtures and box potentials, we envision the future combination of multi-component atomic gases and box potentials. Our investigation on various atomic mixtures in box potentials will provide theoretical understanding in the field and provide reference to those potential experiments.

In **Chapter 2**, we discuss the mean-field theories for interacting bosons and Fermi gases.

In **Chapter 3**, we investigated the impact of mass-imbalance on the structures of atomic mixtures in box potentials by implementing the many-body Gross-Pitaevskii equation for bosons and Hartree-Fock theories for fermions [3, 69, 70]. We considered boson-boson and fermion-fermion mixtures with strong inter-species repulsion confined in a quasi-1D box potential with two hard walls in the x direction. The wavefunctions were required to vanish at the hard walls, while the systems were assumed to be homogeneous in the y and z directions. Our results showed that for repulsive boson-boson mixtures, the mass-imbalance can lead to three-chunk structures compared to the two-chunk structures seen in the equal-mass case. This variation in structure arises from the interplay between the interaction energy and kinetic energies resulting from the density distortion occurring at both the hard walls and the interface of phase separation. On the other hand, repulsive fermion-fermion mixtures exhibited only two-chunk structures regardless of the mass-difference. This is due to an increase in bulk kinetic energies arising from the reduced volume of each species in phase separation.

In **Chapter 4**, we investigated boson-fermion mixtures confined in 1D box. Phase diagrams, density profiles and analyses of the interface properties are discussed for various boson-fermion mixtures. The competition between interaction and kinetic energies dictates the stable structures, which become more intricate in the presence of hard walls, mass asymmetry, and a boson-fermion interface if there is a separation between the two species. Our study allows a systematic extraction of the healing lengths of the bosons and fermions. Furthermore, the scaling of the healing lengths at the interface between bosons and fermions in the phase-separated state provides evidence for the energy-competition mechanism that underlies the phase-separation structures.

In **Chapter 5**, we study atomic Fermi gases with attractive and spatially controllable inhomgeneous interactions to revisit proximity effect and spatial Kibble-Zurek mechanism (KZM) in a unified theoretical framework. The pairing interaction will separate the superfluid phase and normal phase. We con-

sider interaction quenches in real space, step-function quench resembling proximity effect in superconductors and spatial quench depicting spatial KZM. Using Bogoliubov-de Gennes (BdG) approach [71, 72], we derived the profiles of the pair wavefunction and its correlation function to investigate their penetration into the noninteracting region. When considering a step-function quench, we observe that both correlation lengths follow the BCS coherence length and exhibit identical scaling behavior as predicted by studies of proximity effect [73–75]. However, in the case of a spatial quench, the exponents from the two correlation lengths differ, and only the exponent from the pair correlation function agrees with the Kibble-Zurek mechanism (KZM) prediction [76–78].

Lastly, we conclude our work and present some outlook in **Chapter 6**.

CHAPTER 2
ULTRACOLD ATOMIC GASES

2.1 Advancements in trapping cold atoms

Traditionally, ultracold atomic gases have been confined in harmonic potentials, resulting in non-uniform density distributions for which theoretical results relies on Local Density Approximation (LDA) methods to compare with experiments [1, 4]. However, recent advancements in the development of optical potentials have led to the creation of box potentials [63–68, 79], which simplify the comparison between experimental results and theoretical predictions. Homogeneous Bose-Einstein condensates have been achieved in quasi-1D [63, 64], 2D [65], and 3D [66] for trapped bosonic atoms, while homogeneous 2D [67] and 3D [68] Fermi gases have been achieved for two-component fermions. An optical box trap is constructed using a hollow tube beam and two sheet beams, which generate a repulsive force to confine atoms. The Rb-87 atomic cloud, after pre-cooled in a harmonic trap, is then loaded to the cylindrical box-shaped trap [66]. Similar procedures were followed to trap homogeneous Fermi gases in cylindrical box trap [68]. Moreover, dipolar dimers of non-reactive fermionic $^{23}Na^{40}K$ molecules have been experimentally realized in optical box potentials to study collisions of ultracold molecules and compare with those in dipole traps [79].

2.2 Scattering length and coupling constant

When applying the BCS theory to two component fermionic atoms, the two-body scattering length a_{3D} serves as an indicator of the interaction between atoms [1, 4], which can be tuned by a magnetic field. For many-body systems, the effective interaction may be approximated by a contact interaction with coupling constant g_{3D}. Away from resonance,

$$g_{3D} = \frac{4\pi\hbar^2 a_{3D}}{m} \tag{2.1}$$

where, a_{3D} is three-dimensional scattering length, $\hbar$ is reduced Planck's constant and m denotes the mass of an atom. The magnitude of the scattering length a_{3D} informs about the strength of the interaction whereas the sign indicates whether the interaction is repulsive or attractive.

However, Feshbach resonance has been used for studying BCS superfluids

of cold atoms and the BCS-BEC crossover [1,4]. Near a resonance, the renormalized interaction is

$$\frac{1}{g_{3D}} = \frac{m}{4\pi\hbar^2 a_{3D}} - \frac{1}{V}\sum_k \frac{1}{2\epsilon_k} \tag{2.2}$$

Here ϵ_k is the dispersion of noninteracting fermions. For fermionic superfluids of cold atoms, $a_{3D} < 0$ indicates the conventional BCS superfluid while $a_{3D} > 0$ indicates a condensate of tightly-bound pairs.

In quasi-1D Fermi gases, the 1D effective coupling constant maybe expressed as [80]

$$g_{1D} = \frac{2\hbar^2 a_{3D}}{m a_\perp^2} \frac{1}{1 - A a_{3D}/a_\perp}, \tag{2.3}$$

where A is a constant associated with the confinement induced resonance and $a_\perp$ is the characteristic length in the transverse direction. The effective interactions switch from attractive to repulsive at the confinement induced resonance $A = a_\perp/a_{3D}$. Therefore, g_{1D} may be expressed as

$$g_{1D} = -\frac{2\hbar^2}{m a_{1D}} \tag{2.4}$$

with the 1D scattering length given by $a_{1D} = -\frac{a_\perp^2}{a_{3D}}(1 - A a_{3D}/a_\perp)$.

We remark that a quasi-1D BCS-BEC crossover occurs when the chemical potential changes sign because a_{1D} is always positive. From now onwards, we drop the subscript $1D$ and write the effective 1D coupling constant for fermion-fermion interaction as $g_{ff} = \tilde{g}_{ff} E_f^0/k_f^0$, where $\tilde{g}_{ff}$ is the dimensionless coupling constant, E_f^0 and k_f^0 are Fermi energy and Fermi momentum of non-interacting Fermi gas. In Chapter 3 and 4, we utilize the coupling constant away from the resonance, while in Chapter 5 we use the expression for coupling constant near the resonance.

2.3 Mean-field theory for bosons (Gross - Pitaevskii equation)

The Gross-Pitaevskii equation (GPE) is a non-linear Schrödinger equation that describes the dynamics of a BEC at zero temperature when the scattering length a is much smaller than the mean inter-particle spacing [1,4]. At low-energy scattering, the effective interaction between two bosons is given as $g_{bb} = 4\pi\hbar^2 a/m_b$ where m_b denotes the mass of a boson.

We consider a gas of N_b identical bosons confined by external potential $V(r)$ that interacts via the contact interaction.

Gross-Pitaevskii energy functional in terms of $\psi_b(r)$ can be written as,

$$E_b[\psi] = \int dr\Big[\frac{\hbar^2}{2m_b}N_b|\nabla\psi_b(r)|^2 + N_bV(r)|\psi_b(r)|^2 + \frac{1}{2}g_{bb}N_b^2|\psi_b(r)|^4\Big] \tag{2.5}$$

Minimizing the energy functional subject to the normalization condition $\int|\psi_b(r)|^2dr = 1$,

$$\frac{\delta(E_b - \mu_bN_b)}{\delta\psi^*} = 0 \tag{2.6}$$

$$\Big[-\frac{\hbar^2}{2m_b}\nabla^2 + V(r) + g_{bb}N_b|\psi_b(r)|^2\Big]\psi_b(r) = \mu_b\psi_b(r) \tag{2.7}$$

where, μ_b is the chemical potential that imposes the particle number conservation. The non-linear term $g_{bb}N_b|\psi_b(r)|^2$ is the Hartree energy contributed by the interaction between the bosons. This self-consistent mean-field non-linear Schrödinger equation to govern the macroscopic wavefunction of BEC is called Gross-Pitaevskii equation (GPE). The dynamics of a condensate is governed by the time-dependent GPE,

$$i\hbar\frac{\partial\psi_b(r,t)}{\partial t} = \Big[-\frac{\hbar^2}{2m_b}\nabla^2 + V(r) + g_{bb}N_b|\psi_b(r,t)|^2\Big]\psi_b(r,t) \tag{2.8}$$

The time-dependence of the wavefunction is determined by the chemical potential as $\psi_b(r,t) = \psi_b(r)e^{-i\mu t/\hbar}$. The GPE provides an effective description of the macroscopic wavefunction of the BEC and works well at low temperatures in the weakly interacting regime [1, 69].

2.4 Mean-field theory for repulsive Fermi gases

The second-quantization Hamiltonian for two-component repulsive fermions labeled by $\sigma = \uparrow, \downarrow$ with an effective interaction $V_{eff} > 0$ is given by

$$\mathcal{H} = \sum_\sigma\int dr\psi_\sigma^\dagger(r)h_\sigma(r)\psi_\sigma(r) + \frac{1}{2}\sum_{\sigma,\sigma'}\iint drdr'V_{eff}(r,r')\psi_\sigma^\dagger(r)\psi_{\sigma'}^\dagger(r')\psi_{\sigma'}(r')\psi_\sigma(r).$$

Here $\psi_\sigma^\dagger(r)$ (or $\psi_\sigma(r)$) is the fermion creation (or annihilation) operator with spin σ at location r, and $h_\sigma(r) = -\frac{\hbar^2}{2m}\nabla^2 + V_{ext}(r) - \mu_\sigma$.

Performing Hartree-Fock like mean-field decoupling to the quartic interaction term for repulsive Fermi gases,

$$\begin{aligned}\psi_\uparrow^\dagger\psi_\downarrow^\dagger\psi_\downarrow\psi_\uparrow &\approx \langle\psi_\uparrow^\dagger\psi_\uparrow\rangle\psi_\downarrow^\dagger\psi_\downarrow + \langle\psi_\downarrow^\dagger\psi_\downarrow\rangle\psi_\uparrow^\dagger\psi_\uparrow - \langle\psi_\uparrow^\dagger\psi_\uparrow\rangle\langle\psi_\downarrow^\dagger\psi_\downarrow\rangle \\ &\approx n_\uparrow\psi_\downarrow^\dagger\psi_\downarrow + n_\downarrow\psi_\uparrow^\dagger\psi_\uparrow - n_\uparrow n_\downarrow\end{aligned} \tag{2.9}$$

where, $n_\sigma = \langle \psi_\sigma^\dagger \psi_\sigma \rangle$ is the density of each component. In compact matrix form, the Hamiltonian is

$$\mathcal{H}_{HF} = \int dr \begin{pmatrix} \psi_\uparrow^\dagger & \psi_\downarrow^\dagger \end{pmatrix} M \begin{pmatrix} \psi_\uparrow \\ \psi_\downarrow \end{pmatrix} \tag{2.10}$$

where,

$$M = \begin{pmatrix} h_\uparrow & V_{eff} n_\uparrow \\ V_{eff} n_\downarrow & h_\downarrow \end{pmatrix} \tag{2.11}$$

We diagonalize $\mathcal{H}_{MF}$ to obtain the eigenvalues $E_{\sigma,i}$ and eigenstates $\psi_{\sigma,i}$.

$$\begin{aligned} (-\frac{\hbar^2}{2m}\nabla^2 + V_{ext} + V_{eff} n_\downarrow - \mu_\uparrow)\psi_{\uparrow,i} &= E_{\uparrow,i}\psi_{\uparrow,i} \\ (-\frac{\hbar^2}{2m}\nabla^2 + V_{ext} + V_{eff} n_\uparrow - \mu_\downarrow)\psi_{\downarrow,i} &= E_{\downarrow,i}\psi_{\downarrow,i} \end{aligned} \tag{2.12}$$

To solve the coupled equation Eq.(2.12) self-consistently, we start with a set of trial wavefunctions ψ_σ and solve the coupled equations to get the eigenvalues and their corresponding normalized eigenvectors. From the eigenvectors, we calculate the densities at each iteration for each component using $n_\sigma = \langle \psi_\sigma^\dagger \psi_\sigma \rangle$ and employ it to solve the coupled equations Eq.(2.12) again until the desired accuracy is reached. The convergence criteria is $\int |n_\sigma^{t+1} - n_\sigma^t| dr < 10^{-5}$ for $t - th$ iteration. We utilize this technique in the case of repulsive fermion-fermion mixtures discussed in chapter 3 to obtain the density profiles.

2.5 Mean-field theory for attractive Fermi gases

In this section, we derive the Bogoliubov-de-Gennes equation for two-component Fermi gases with attractive interaction $V_{eff} < 0$ using the BCS Hamiltonian Eq.(2.14) and discuss the numerical procedures to solve them. Performing Hartree-Fock like mean-field decoupling to the quartic interaction term for attractive Fermi gases [3],

$$\psi_\uparrow^\dagger \psi_\downarrow^\dagger \psi_\downarrow \psi_\uparrow \approx \langle \psi_\uparrow^\dagger \psi_\downarrow^\dagger \rangle \psi_\downarrow \psi_\uparrow + \psi_\uparrow^\dagger \psi_\downarrow^\dagger \langle \psi_\downarrow \psi_\uparrow \rangle - \langle \psi_\uparrow^\dagger \psi_\downarrow^\dagger \rangle \langle \psi_\downarrow \psi_\uparrow \rangle \tag{2.13}$$

where, pairing correlations are considered at the mean-field level leading to the BCS Hamiltonian:

$$\begin{aligned} \mathcal{H}_{BCS} = &\sum_\sigma \int dr \psi_\sigma^\dagger(r) h_\sigma(r) \psi_\sigma(r) + \iint dr dr' (\Delta(r,r') \psi_\uparrow^\dagger(r) \psi_\downarrow^\dagger(r') + h.c) \\ &- \iint dr dr' |\Delta(r,r')|^2 / V_{eff}(r,r'). \end{aligned} \tag{2.14}$$

The gap function $\Delta(r, r')$ is defined as

$$\Delta(r,r') = -V_{eff}(r-r') \langle \psi_\uparrow(r) \psi_\downarrow(r') \rangle \tag{2.15}$$

Here $\langle O \rangle$ is the ensemble average of operator O.

Commutation relation for fermionic operators $\hat{A}$,$\hat{B}$ and $\hat{C}$ is given as:

$$[A, BC] = \{A, B\}C - B\{A, C\} \tag{2.16}$$

Using this relation, we find the commutators of fermionic field operators with the Hamiltonian.

$$\begin{aligned}
[\psi_\uparrow(r), \mathcal{H}_{\mathcal{BCS}}] &= h_\uparrow(r)\psi_\uparrow(r) + \int dr' \Delta(r, r')\psi_\downarrow^\dagger(r') \\
[\psi_\uparrow^\dagger(r), \mathcal{H}_{\mathcal{BCS}}] &= -h_\uparrow^*(r)\psi_\uparrow^\dagger(r) - \int dr' \Delta^*(r, r')\psi_\downarrow(r') \\
[\psi_\downarrow(r), \mathcal{H}_{\mathcal{BCS}}] &= h_\downarrow(r)\psi_\uparrow(r) - \int dr' \Delta(r', r)\psi_\uparrow^\dagger(r') \\
[\psi_\downarrow^\dagger(r), \mathcal{H}_{\mathcal{BCS}}] &= -h_\downarrow^*(r)\psi_\downarrow^\dagger(r) + \int dr' \Delta^*(r', r)\psi_\downarrow(r')
\end{aligned} \tag{2.17}$$

Above commutators mean to say that fermionic field operators can be expressed as a linear combination of particle and hole like quasi-particle excitations. This is the motivation for Bogoliubov canonical transformations.

2.5.1 Bogoliubov-de-Gennes equation

Bogoliubov canonical transformation is given as [71,72]:

$$\psi_\sigma(r) = \sum_n [u_{n\sigma}(r)\gamma_n - \sigma v_{n\sigma}^*(r)\gamma_n^\dagger] \tag{2.18}$$

The labels σ in the subscript refers to the spin of the particle whereas σ carries + or − sign in the second term of above canonical transformation. The quasi-particle operators satisfy the anti-commutation relations

$$\{\gamma_n, \gamma_m^\dagger\} = \delta_{nm},\ \{\gamma_n, \gamma_m\} = \{\gamma_n^\dagger, \gamma_m^\dagger\} = 0, \tag{2.19}$$

The Bogoliubov transformation diagonalizes $\mathcal{H}_{BCS}$ from Eq.(2.14) to the form

$$\mathcal{H} = \sum_n E_n \gamma_n^\dagger \gamma_n + E_g, \tag{2.20}$$

where ground state energy is given as $E_g = -\frac{|\Delta|^2}{V_{eff}} + \sum_n (\epsilon_n - E_n)$. Here ϵ_n is the non-interacting ($V_{eff} = 0$) counterpart of the excitation energy E_n. Using the

canonical transformations for $\psi_\uparrow$,$\psi_\downarrow$,$\psi_\uparrow^\dagger$ and $\psi_\downarrow^\dagger$ and the anti-commutation relations,

$$\{\mathcal{H}, \gamma_n\} = E_n\gamma_n,\ \{\mathcal{H}, \gamma_n^\dagger\} = -E_n\gamma_n^\dagger, \tag{2.21}$$

in Eqs.(2.17) and comparing the coefficients of γ_n and $\gamma_n^\dagger$, one can obtain a set of four equations in a compact form:

$$\int dr' M(r, r')\phi(r') = E_n\phi(r) \tag{2.22}$$

where,

$$M(r, r') = \begin{pmatrix} h_\uparrow(r, r') & 0 & 0 & \Delta(r, r') \\ 0 & h_\downarrow(r, r') & \Delta(r', r) & 0 \\ 0 & \Delta^*(r, r') & -h_\uparrow^*(r, r') & 0 \\ \Delta^*(r', r) & 0 & 0 & -h_\downarrow^*(r, r') \end{pmatrix} \tag{2.23}$$

and

$$\phi(r) = \begin{pmatrix} u_\downarrow^n(r) \\ u_\uparrow^n(r) \\ v_\downarrow^n(r) \\ v_\downarrow^n(r) \end{pmatrix}, h_\sigma(r, r') = h_\sigma(r)\delta(r - r'), \Delta(r, r') = \Delta(r)\delta(r - r') \tag{2.24}$$

In the absence of spin-orbit coupling, BdG equations(2.22) is block-diagonalized into two subset of equations.

$$\int dr' \begin{pmatrix} h_\uparrow(r, r') & \Delta(r, r') \\ \Delta^*(r', r) & -h_\downarrow^*(r, r') \end{pmatrix} \begin{pmatrix} u_\uparrow^{\tilde{n}1}(r') \\ v_\downarrow^{\tilde{n}1}(r') \end{pmatrix} = E_{\tilde{n}1} \begin{pmatrix} u_\uparrow^{\tilde{n}1}(r) \\ v_\downarrow^{\tilde{n}1}(r) \end{pmatrix} \tag{2.25}$$

$$\int dr' \begin{pmatrix} h_\downarrow(r, r') & \Delta(r', r) \\ \Delta^*(r', r) & -h_\uparrow^*(r, r') \end{pmatrix} \begin{pmatrix} u_\uparrow^{\tilde{n}2}(r') \\ v_\downarrow^{\tilde{n}2}(r') \end{pmatrix} = E_{\tilde{n}2} \begin{pmatrix} u_\uparrow^{\tilde{n}2}(r) \\ v_\downarrow^{\tilde{n}2}(r) \end{pmatrix} \tag{2.26}$$

where, redefined eigenstate index for quasi-particle amplitudes $\tilde{n}1$ and $\tilde{n}2$ comes from the Bogoliubov transformation as

$$\begin{aligned} \psi_\uparrow(r) &= \textstyle\sum_{\tilde{n}}[u_\uparrow^{\tilde{n}1}(r)\gamma_{\tilde{n}1} - v_\uparrow^{\tilde{n}2*}(r)\gamma_{\tilde{n}2}^\dagger] \\ \psi_\downarrow(r) &= \textstyle\sum_{\tilde{n}}[u_\downarrow^{\tilde{n}2}(r)\gamma_{\tilde{n}2} + v_\downarrow^{\tilde{n}1*}(r)\gamma_{\tilde{n}1}^\dagger] \end{aligned} \tag{2.27}$$

and the diagonalized Hamiltonian

$$\mathcal{H} = \sum_{\tilde{n}w} E_{\tilde{n}w}\gamma_{\tilde{n}w}^\dagger\gamma_{\tilde{n}w} + E_g, \tag{2.28}$$

where, $w = 1, 2$ represents the two-component of the quasi-particle operators. We see that spin-up electron-like component of the wave function $u_\uparrow$ is coupled only to the spin-down hole-like component of wave function $v_\downarrow$ and spin-down

electron-like component $u_\downarrow$ is coupled only to spin-up hole-like component $v_\uparrow$. If we take the complex conjugation of Eq.(2.25), multiplying with a minus sign and rearrange the equations, we arrive at the identical equation to Eq.(2.26) with symmetry property,

$$\begin{pmatrix} u_\downarrow^{\tilde{n}2}(r) \\ v_\uparrow^{\tilde{n}2}(r) \end{pmatrix} = \begin{pmatrix} v_\downarrow^{\tilde{n}1*}(r) \\ -u_\uparrow^{\tilde{n}1}(r) \end{pmatrix} \tag{2.29}$$

and $E_{\tilde{n}2} = -E_{\tilde{n}1}$. This symmetry property implies that instead of solving both subsets of equations (2.25,2.26), we can only solve one of these equations to calculate all the measurable quantities. The quasi-particle operators follows the statistical average

$$< \gamma_{\tilde{n}w}^\dagger, \gamma_{\tilde{m}v} >= \delta_{\tilde{n}\tilde{m}}\delta_{wv} f(E_{\tilde{n}w}), < \gamma_{\tilde{n}w}, \gamma_{\tilde{m}v} >=< \gamma_{\tilde{n}w}^\dagger, \gamma_{\tilde{m}v}^\dagger >= 0 \tag{2.30}$$

where,

$$f(E_{\tilde{n}w}) = \frac{1}{e^{E_{\tilde{n}w}/K_BT} + 1} \tag{2.31}$$

is the Fermi distribution function. Using statistical average, symmetry property and the canonical transformations, the gap function in Eq.(2.15) is given as

$$\Delta(r, r') = -V_{eff}(r - r') \sum_{\tilde{n}}{}' u_\uparrow^{\tilde{n}}(r) v_\downarrow^{\tilde{n}*}(r') \tanh(E_{\tilde{n}}/k_BT) \tag{2.32}$$

Here, we dropped the indices 1,2 from the quasi-particle wavefunctions and $\sum_{\tilde{n}}{}'$ means the summation is over the positive-energy states. The effective interaction in atomic Fermi gases is dominated by the contact interaction valid at low temperatures, so $V_{eff}(r - r') = g_{ff}(r)\delta(r - r')$. As $T \to 0$, $\tanh(\infty) = 1$ and for s-wave pairing Thus, $\Delta(r, r') = \Delta(r', r) = \Delta(r)\delta(r - r')$. At zero temperature, the gap function is given by

$$\Delta(r) = -g_{ff} \sum_{\tilde{n}}{}' u^{\tilde{n}}(r) v^{\tilde{n}*}(r). \tag{2.33}$$

We consider equal population of the two components, $N_\uparrow = N/2 = N_\downarrow$, so $\mu_\sigma = \mu$. BdG equations can be written as

$$\begin{pmatrix} -\frac{\hbar^2}{2m}\frac{\partial^2}{\partial x^2} - \mu & \Delta(x) \\ \Delta^*(x) & -(-\frac{\hbar^2}{2m}\frac{\partial^2}{\partial x^2} - \mu) \end{pmatrix} \begin{pmatrix} u_{\tilde{n}}(x) \\ v_{\tilde{n}}(x) \end{pmatrix} = E_{\tilde{n}} \begin{pmatrix} u_{\tilde{n}}(x) \\ v_{\tilde{n}}(x) \end{pmatrix} \tag{2.34}$$

For a two-component Fermi gas in a 1D box of length L, we discretize the space as $x/L = [0, 1]$ using n_x grid points. $x_j = j\delta x$, where $\delta x = L/n_x$ and $j = 0, 1, 2, ..., n_x$. The Laplacian operator is represented by using the finite-difference method. In the discretized form, the BdG equation becomes

$$\sum_j \begin{pmatrix} h_{ij} & \Delta_{ij} \\ \Delta_{ij}^* & -h_{ij} \end{pmatrix} \begin{pmatrix} u_j^{\tilde{n}} \\ v_j^{\tilde{n}} \end{pmatrix} = E_{\tilde{n}} \begin{pmatrix} u_i^{\tilde{n}} \\ v_i^{\tilde{n}} \end{pmatrix}. \tag{2.35}$$

Note that for s-wave pairing, $\Delta_{ij} = 0$ if $i \neq j$. The BdG Hamiltonian has the size of $2n_x \times 2n_x$ and we only take the positive energy eigenstates for the calculations of the gap function and density.

The fermion density of each component is $\rho_\sigma(x) = \langle \psi_\sigma^\dagger(x)\psi_\sigma(x)\rangle$, and the total density $\rho(x) = \sum_\sigma \rho_\sigma(x)$ becomes

$$\rho_f(x) = 2\sum_{\tilde{n}}{}' |v_{\tilde{n}}(x)|^2. \tag{2.36}$$

The total fermion number is $N_f = N_\uparrow + N_\downarrow = \int_0^L \rho_f(x)dx$. The gap function is given by

$$\Delta(x) - g_{ff}(x) < \psi_\downarrow\psi_\uparrow >= -g_{ff}(x)\sum_{\tilde{n}}{}' u_{\tilde{n}}(x)v_{\tilde{n}}(x). \tag{2.37}$$

Numerical procedures to solve the BdG equations is given in Appendix C.

2.6 Characteristic lengths of spatial change in quantum systems

Characteristic length scales play a crucial role in understanding the behavior of quantum systems, as they help to determine the spatial extent over which quantum mechanical effects are significant. They can have profound effects on the behavior of particles in a wide variety of physical systems and they determine the spatial extent over which particles can interact with each other. For example, the characteristic length scales of atoms in a solid determine the range of inter-atomic forces, which in turn affects the properties of the material, such as its conductivity or optical properties [81].

Another example of characteristic length can be given as healing length of bosons in case of pure BEC [1] which determines the stability of a BEC to a localized perturbation as it is dependent on the balance between kinetic energy and interaction energy, as well as the interaction strength between the particles.

$$\xi_b = \frac{\hbar}{\sqrt{2m_b g_{bb}\rho_b}} \tag{2.38}$$

More detailed analyses of the healing lengths for both bosons and fermions is given in Chapter 4.

The characteristic length scale for superconductors is the coherence length, denoted by ξ_Δ. The BCS coherence length is given as [1,3,82]

$$\xi_\Delta = \frac{\hbar v_f}{\Delta} \tag{2.39}$$

The coherence length represents the length scale over which the electron's wavefunction in a superconductor remains coherent and its superconducting behavior is preserved [56]. Practically, it gives the information on the Cooper pair size.

Quantum phase transitions are accompanied with the fundamental change in the ground state of the system when one of the parameters in the Hamiltonian is driven across the critical point [83]. In the vicinity of the quantum phase transitions, the correlation length diverges, indicating the emergence of long-range correlations between particles in the system. These long-range correlations can lead to the formation of complex patterns and structures, and they are a key characteristic of quantum critical phenomena. Near a critical point, the correlation length scales with a power law as a function of the distance to the critical point. This scaling behavior is captured by the critical exponent ν, which characterizes the rate at which the correlation length diverges as the system approaches the critical point [84]. For example, the critical exponent determines the scaling properties of various physical observable, such as the susceptibility and the correlation function. The correlation length provides a measure of how strongly correlated the particles in the system are with each other, and it can have a profound effect on the behavior of the system as it undergoes a phase transition.

Overall, the characteristic lengths of spatial change in quantum systems are important in understanding and predicting the behavior of particles, such as interactions and correlations, in various physical systems.

CHAPTER 3

BINARY ATOMIC MIXTURES OF SAME SPIN STATISTICS IN BOX POTENTIALS

The results presented here have been published in Bishal Parajuli, Daniel Pecak and Chih-Chun Chien, *Mass-imbalance-induced structures of atomic mixtures in box potentials*, Phys. Rev. A 100, 063623 [85].

In this chapter, we consider ground state structures of atomic mixtures following same spin statistics in box potentials. We simulate the many-body system using density-density interactions and compare the structures with and without mass-imbalance. The phase diagram and analyses of healing lengths at the interface for both species are reported as well.

3.1 Repulsive boson-boson mixtures in box potentials

In this study, we utilize the Gross-Pitaevskii (GP) theory, which is commonly used to describe bosonic condensates [1,69], to investigate the structures of mixtures of bosons confined in a 1D box potential. Previous experimental work on two-component bosons confined in a harmonic trap showing both the miscible and phase-separated regimes has also referenced the GP theory [86]. Therefore, we limit our focus to the weak and intermediate interaction regimes, where the GP theory is known to provide reasonable predictions. Here we consider a mixture confined by two hard-walls at $x = 0, L$ modeled by the box potential and the system is uniform in the other directions. The Gross-Pitaevskii energy functional of a boson-boson mixture is [1]

$$E = \int_0^L dx\Big[\frac{\hbar^2}{2m_1}|\partial_x\psi_1|^2 + \frac{\hbar^2}{2m_2}|\partial_x\psi_2|^2 + \frac{1}{2}\tilde{g}_{11}N_1^2|\psi_1|^4 + \frac{1}{2}\tilde{g}_{22}N_2^2|\psi_2|^4 + \tilde{g}_{12}N_1N_2|\psi_1|^2|\psi_2|^2\Big]. \tag{3.1}$$

The condensate wavefunctions are normalized by $\int_0^L dx|\psi_\alpha|^2 = 1$, where $\alpha = 1, 2$ denotes components. The mass m_α and number of particles N_α correspond to species α. The coupling constants $\tilde{g}_{11}$, $\tilde{g}_{22}$ and $\tilde{g}_{12} = \tilde{g}_{21}$ are related to the two-body s-wave scattering lengths a_{11}, a_{22} and a_{12} by

$$g_{\alpha\beta} = \frac{2\pi\hbar^2 a_{\alpha\beta}}{m_{\alpha\beta}}. \tag{3.2}$$

Here $m_{\alpha\beta} = \frac{m_\alpha m_\beta}{m_\alpha + m_\beta}$ is the reduced mass of pair of atoms and $\alpha, \beta = 1, 2$ denote the species. We focus on the repulsive case with $g_{\alpha\beta} > 0$.

The Gross-Pitaevskii equation, which describes a system's minimal-energy configuration, can be obtained by minimizing the energy functional with respect to ψ_α^* for $\alpha = 1, 2$ using the equation $\delta E/\delta\psi_\alpha^* = 0$. To find the lowest energy state of a system with a given initial configuration, we use the imaginary-time formalism given in Appendix A.

Therefore, we search for the solutions to the coupled imaginary-time evolution equations in the x-direction:

$$\begin{aligned} -\hbar\frac{\partial\psi_1}{\partial\tau} &= -\frac{\hbar^2}{2m_1}\partial_x^2\psi_1 + g_{11}N_1|\psi_1|^2\psi_1 + g_{12}\sqrt{N_1N_2}|\psi_2|^2\psi_1 \\ -\hbar\frac{\partial\psi_2}{\partial\tau} &= -\frac{\hbar^2}{2m_2}\partial_x^2\psi_2 + g_{22}N_2|\psi_2|^2\psi_2 + g_{12}\sqrt{N_1N_2}|\psi_1|^2\psi_2. \end{aligned} \tag{3.3}$$

The boundary conditions are $\psi_\alpha = 0$ at $x = 0, L$ for $\alpha = 1, 2$. We choose the units so that $\hbar = 2m_1 = 1$. The conservation of particle numbers imposes the following normalization condition of the density $\rho_\alpha = N_\alpha|\psi_\alpha|^2$. The total particle number of species $\alpha = 1, 2$ can then be obtained from

$$N_\alpha = \int_0^L dx\rho_\alpha. \tag{3.4}$$

In the weakly interacting regime and at low temperatures, the Gross-Pitaevskii (GP) equation provides an effective description of the macroscopic wavefunction of the Bose-Einstein condensate (BEC) [1,69]. For a homogeneous mixture of bosons with equal mass and repulsive inter- and intra-species interactions in the thermodynamic limit, the stability condition has been summarized in Refs. [1, 87, 88], and the system exhibits phase separation when $g_{11}g_{22} < g_{12}^2$. It is noteworthy that if any of the intra-species interactions vanish, $g_{\alpha\alpha} = 0$, the miscible phase becomes unstable against any finite inter-species interaction. In this study, we aim to investigate the effects of mass imbalance on the structure in the phase separation regime when the system is confined in a box potential. Although other methods have been proposed for obtaining density profiles of bosons or bosonic mixtures [89–92], we use the GP equation since it reasonably describes the bosonic mixture experiment reported in Ref. [86].

We use the split step Crank-Nicolson method to solve the coupled imaginary-time evolution equations [93,94] which is given in detail in Appendix B. The spatial and temporal increments are calibrated by checking against the exact solutions of nonlinear Schrödinger equations [95]. In the following, we consider the structures of boson-boson mixtures with and without mass imbalance. We use the following parameters: $\Delta\tau = 0.0001\hbar/E_0$ for the imaginary time increment. $E_0 = \hbar^2/(2m_1L^2)$ is the energy unit. $N_1 = N_2 = 50$ for the particle number of each species. By defining $g_0 = 4\pi\hbar^2/(m_1L)$, we express the coupling

constants in terms of $g_{\alpha\beta} = \tilde{g}_{\alpha\beta}\, g_0$. A 500-point grid is used to discretize the space, and we have checked the results are insensitive to a further refinement of the grid.

3.1.1 Phase diagram and density profiles

From the two-component GP equations for equal-mass boson-boson mixtures, we found a miscible phase when the repulsive inter-species interaction is weak. When the inter-species repulsion in strong, phases separation emerges and the two species congregate into two chunks. As the inter-species interaction $\tilde{g}_{12}$ increases, the overlap of the density profiles decreases leading to narrower interface width between two components. Figure 3.1 shows the phase diagram (a) and density profiles (b)-(d) of typical structures of the equal-mass case. Importantly, the phase separation into two chunks breaks the left-right parity symmetry. We remark that for the equal-mass mixture, the GP equations (3.3) are symmetric between the two components. With a perfect overlap of the initial condition and trap potentials, the system does not enter phase separation if there is no noise during the evolution. The system may enter a fragmented state [96] due the the symmetry between the two components. Imperfections in the initial condition or numerical noise in the simulations are enough to drive the system to phase separation in the strongly repulsive regime. Moreover, experiments on equal-mass bosonic mixtures in harmonic traps [86] have shown phase separation.

For boson-boson mixtures with different masses, we take the mixture of ^{7}Li and ^{87}Rb for example. The system exhibits two-chunk and three-chunk separation of the two species as the inter-species interaction increases. Figures 3.2 (a) shows the phase-diagram and (b)-(d) show the miscible phase, three-chunk phase separation and two-chunk phase separation respectively. There is an important difference between the full phase-separation structures of the equal-mass and the different-mass case in intermediate interaction regime. For the mass-imbalanced case, the system exhibits a sandwich structure (three-chunk). The lighter species does not touch either of the hard walls. This is because the kinetic-energy increase of the light species at the hard walls can lead to higher total energy, so the lowest-energy configuration has the heavier species locating at both hard-walls. In contrast, there is no such advantage in the equal-mass case, and the two species minimize the number of interfaces between them by separating into only two chunks. As a consequence of the mass imbalance, the phase-separation structure can break the parity symmetry by forming two chunks in the equal-mass case, or the system can keep the parity symmetry in the sandwich structure when the mass imbalance is large.

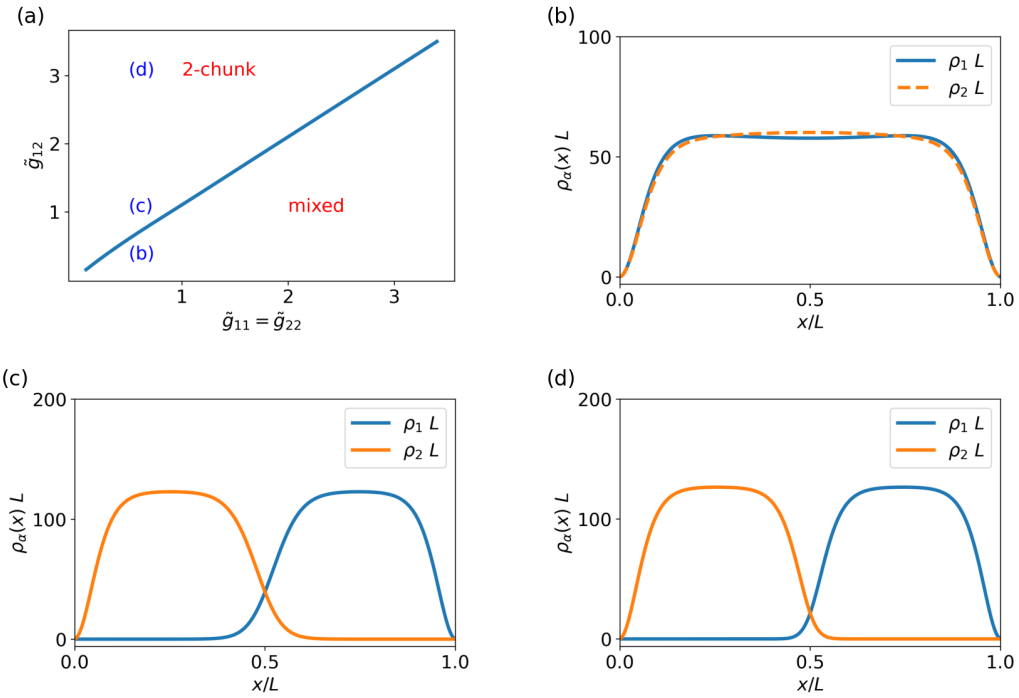

Figure 3.1: Phase diagram (a) and density profiles (b)-(d) of equal-mass boson-boson mixtures in a box potential. Here, $\tilde{g}_{11} = 0.5$ and $\tilde{g}_{22} = 0.5$ (b) Miscible phase with low inter-species repulsion $\tilde{g}_{12} = 0.3$, and phase separation due to high inter-species repulsion (c)$\tilde{g}_{12} = 0.7$ and (d) $\tilde{g}_{12} = 3.0$ with their locations labelled on (a). Here $N = 50$ for each species and $g_{\alpha\beta} = \tilde{g}_{\alpha\beta}\, g_0$.

3.1.2 Interface properties

In the phase-separation structures shown in Fig.(3.1), both species are present at the interface between the two species. The interaction energies for species 1 and 2 per particle at the interface is given as

$$\begin{aligned} IE_1 &= g_{11}\rho_1 + g_{12}\rho_2 \\ IE_2 &= g_{22}\rho_2 + g_{12}\rho_1 \end{aligned} \tag{3.5}$$

If $\xi_{b\alpha}$ denotes the healing lengths for species $\alpha = 1, 2$, then the kinetic energy per particle due to the distortion of the wavefunction is given by $KE_\alpha = \frac{\hbar^2}{2m_\alpha \xi_{b\alpha}^2}$. The healing length $\xi_{b\alpha}$ is the length scale at which kinetic energy balances the interaction energy of the bosons and can be estimated using the condition $KE_\alpha \approx$

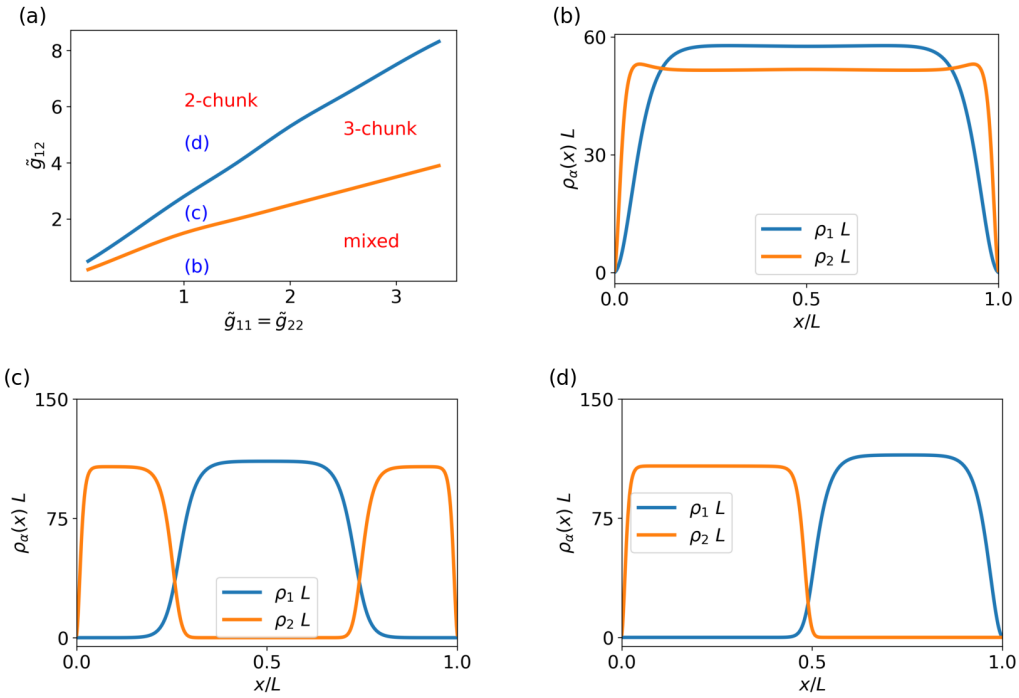

Figure 3.2: Phase diagram (a) and density profiles (b)-(d) of ^7Li-^{87}Rb boson-boson mixtures in a box potential. Here, $\tilde{g}_{11} = 1.0$ and $\tilde{g}_{22} = 1.0$ (b) Miscible phase with low inter-species repulsion $\tilde{g}_{12} = 0.1$, and phase separation due to high inter-species repulsion (c) $\tilde{g}_{12} = 0.7$ and (d) $\tilde{g}_{12} = 3.0$ with their locations labelled on (a). Here $N = 50$ for each species and $g_{\alpha\beta} = \tilde{g}_{\alpha\beta}\ g_0$.

IE_α. Explicitly for species 1 and 2 for boson-boson mixtures

$$\tilde{\xi}_{b1} \sim \frac{1}{\sqrt{8\pi}} \frac{1}{\sqrt{\tilde{g}_{11}\rho_1 L + (\frac{m_1+m_2}{2m_2})\tilde{g}_{12}\rho_2 L}} \equiv \frac{1}{\sqrt{S_{b1}}}$$
$$\tilde{\xi}_{b2} \sim \frac{1}{\sqrt{8\pi}} \frac{1}{\sqrt{\tilde{g}_{22}\rho_2 L + (\frac{m_1+m_2}{2m_1})\tilde{g}_{12}\rho_1 L}} \equiv \frac{1}{\sqrt{S_{b2}}} \tag{3.6}$$

$\tilde{\xi}_{b\alpha} = \xi_{b\alpha}/L$ is dimensionless healing length and S_{b1} and S_{b2} are dimensionless quantity to simplify the scaling analyses of the healing lengths. We remark that in the expressions of the healimg lengths, ρ_α denotes the bulk density of the corresponding species away from the hard wall or the interface. In our analyses of the healing lengths, we take the width as the distance between 95% and 5% of the value of $\sqrt{\rho_\alpha}$ at the plateau in the bulk. Taking different criteria or using functional fits to the density profiles leads to basically the same scaling behavior, which verifies the robustness of the energy-competition argument.

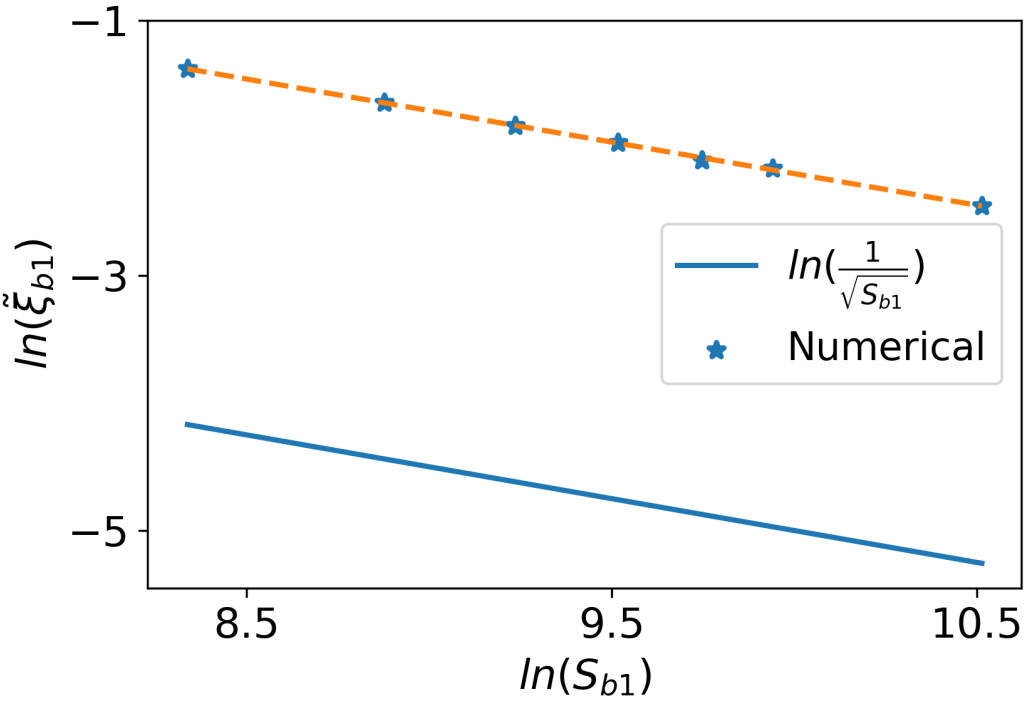

Figure 3.3: Scaling behavior of the healing lengths of species 1 at the interface of a boson-boson mixture in the two-chunk separation from the simulations and Eqs. 3.6. Here $N_1 = N_2 = 50$ and $\tilde{g}_{22} = 0.5$.

Fig.(3.3) shows the scaling behavior of species 1 of boson-boson mixtures at the interface. The agreement of the scaling behavior between the numerical results and analytical formulas confirms the energy competition argument. For equal-mass boson-boson mixtures, two-chunk structures are always symmetric and we do not need to analyze the healing length for species 2 at the interface of equal-mass boson-boson mixtures.

Fig.(3.4) show the scaling behavior of both species at the interface of ^{7}Li - ^{87}Rb mixture in two-chunk phase-separation. Similar analyses on three-chunk structures basically leads to the same scaling behavior, however, due to requirement of wide parameter range for the scaling analyses, we stick to two-chunk structures for the interface width calculations. The scaling behavior from the numerical calculations again agrees with the analytical formulas verifying that energy competition argument works well in boson-boson mixtures in quasi-one-dimensional box potential regardless of the mass ratio.

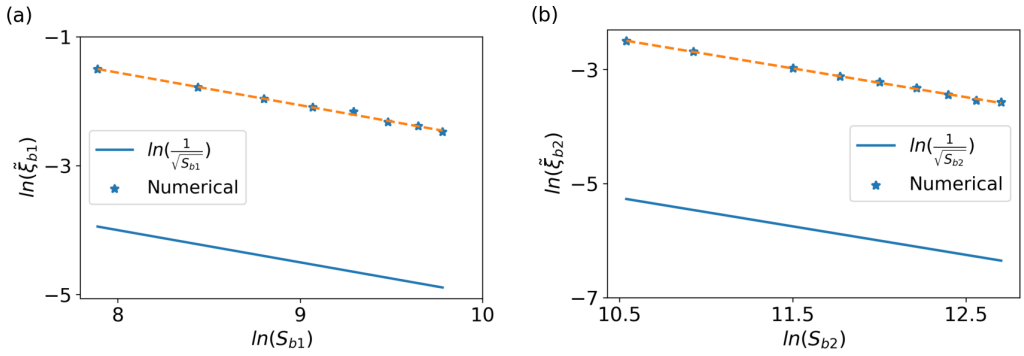

Figure 3.4: Scaling behavior of the healing lengths of species 1 (a) and species 2 at the interface of ^7Li - ^{87}Rb mixture in the two-chunk separation from the simulations and Eqs. 3.6. Here $N_1 = N_2 = 50$ and $\tilde{g}_{22} = 0.5$ in (a) and $\tilde{g}_{11} = 0.5$ in (b) .

3.2 Repulsive fermion-fermion mixtures in box potentials

Similar to the many-body approach to the bosonic mixtures, we model the interactions between fermions as density-density contact interactions except there is virtually no intra-species interaction between identical ultracold fermionic atoms due to the Pauli exclusion principle. The second-quantization Hamiltonian of a fermion-fermion mixture with repulsive interactions in a 1D box is given by

$$\hat{H}_F = \int_0^L dx \Big(\sum_{\alpha=1}^{2} \frac{\hbar^2}{2m_\alpha} |\partial_x \hat{\psi}_\alpha|^2 + g_{12} \hat{\rho}_1 \hat{\rho}_2 \Big). \tag{3.7}$$

Here m_α is the mass of the α-th species, $\hat{\rho}_\alpha = \hat{\psi}_\alpha^\dagger \hat{\psi}_\alpha$ is the density operator, $\alpha = 1, 2$. By using the Hartree-Fock approximation [3], we replace the interaction term by the expectation values $\rho_\alpha = \langle \hat{\rho}_\alpha \rangle$. Assuming the hard-wall confinement is along the x-direction, we obtain the following eigenvalue equations for the two species consistent with the stationary states of Eq. (3.7).

$$\begin{aligned} -\frac{\hbar^2}{2m_1}\frac{\partial^2}{\partial x^2}\psi_{1,n} + g_{12}\rho_2\psi_{1,n} &= E_{1,n}\psi_{1,n} \\ -\frac{\hbar^2}{2m_2}\frac{\partial^2}{\partial x^2}\psi_{2,n} + g_{12}\rho_1\psi_{2,n} &= E_{2,n}\psi_{2,n} \end{aligned} \tag{3.8}$$

where $E_{\alpha,n}$ are the eigenvalues corresponding to the eigenstates $\psi_{\alpha,n}$, which are from the decomposition of $\hat{\psi}_\alpha$. The boundary conditions are $\psi_{i,n} = 0$ at $x = 0, L$. We choose m_1, L, and $\hbar^2/(2m_1L^2)$ as the units of mass, length, and energy,

respectively. In the ground state, fermions of species $\alpha = 1, 2$, occupy the lowest N_α levels of $\psi_{\alpha,n}$. As a consequence, $\rho_\alpha = \sum_{n=1}^{N_\alpha} |\psi_{\alpha,n}|^2$. Thus, the densities satisfy

$$N_\alpha = \int_0^L dx \rho_\alpha, \tag{3.9}$$

$\alpha = 1, 2$. We will use $N_1 = N_2 = 100$ in our illustrations.

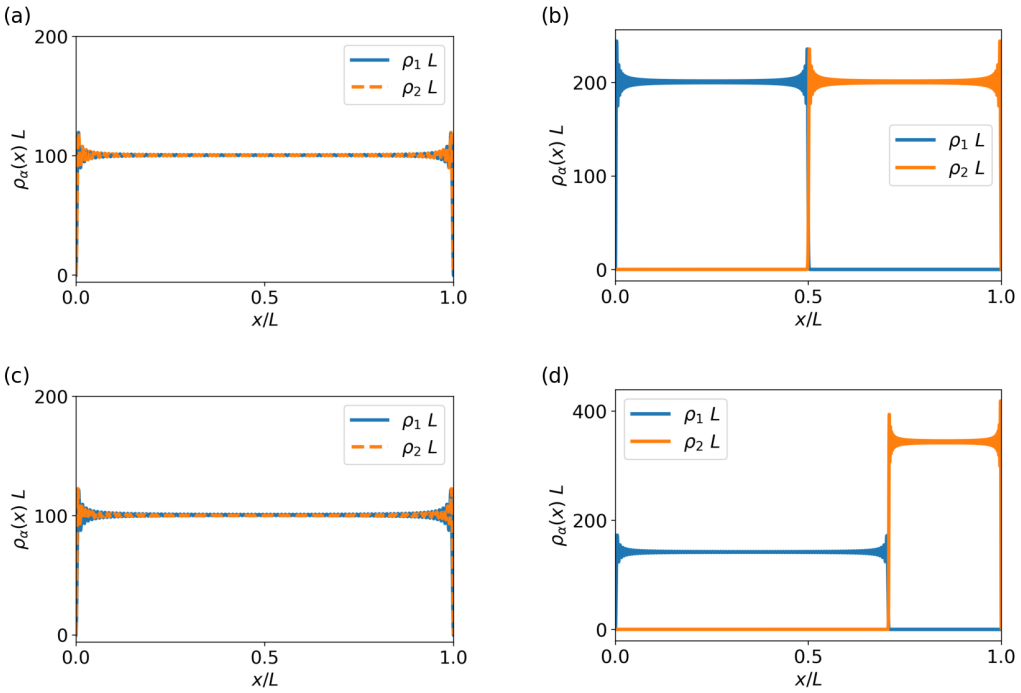

Figure 3.5: Density profiles of fermion-fermion mixtures in 1D box potentials for the case with equal mass shown in (a) and for the case with mass ratio $m_1/m_2 = 6/86$ shown in (c) and (d). The left column [(a) and (c)] shows the miscible structures in the weak repulsion regime, where the two density profiles coincide. The right column [(b) and (d)] shows the phase separation structures in the strong repulsion regime. Here $N_1 = N_2 = 100$ and the values of $\tilde{g}_{12}$ are (a) 300, (b) 5000, (c) 10 and (d) 500.

3.2.1 Density profiles

For a given value of $g_{12} = \tilde{g}_{12}\, g_0$, we use an iteration method similar to the one for solving the Bogoliubov-de Gennes equation of superconductivity [97]. We start with a set of trial density profiles and solve the coupled equations (3.8)

to obtain the eigenvalues and their normalized eigenvectors. From the eigenvectors, we calculate the iterated densities ρ_1 and ρ_2 and use them to solve the coupled equations (3.8) again. The iteration converges if ($\int_0^L |\rho_1^{\nu+1} - \rho_1^{\nu}| dx < \epsilon$ and $\int_0^L |\rho_2^{\nu+1} - \rho_2^{\nu}| dx < \epsilon$) for the ν-th iteration. In our calculation, we choose $\epsilon = 10^{-3}$ and 10^4 grid points in $x/L \in [0, 1]$. We have verified that further changing the tolerance or grid size does not lead to qualitative change as long as the grid number is much larger than the particle number, the latter condition sets a limitation of our many-body calculations. We remark that the mean-field, many-body treatment of fermions overlooks the correlation effect, and the zero-range contact interaction is not accurately incorporated. Moreover, Eqs. (3.7) and (3.8) assume continuous wavefunctions and smooths out possible local structures.

3.2.2 Interface properties

In the phase-separation structures, both species are present at the interface between the two species as shown in Figures 3.5(b) and (d). The interaction energy (IE) per particle of the fermions for species 1 and 2 can be estimated as

$$\begin{aligned} IE_1 &= E_{f1} + g_{12}\rho_2 \\ IE_2 &= E_{f2} + g_{12}\rho_1 \end{aligned} \tag{3.10}$$

For the fermions, Pauli exclusion principle may be considered as an effective (statistical) interaction, which introduces the Fermi energy $E_{f\alpha}$ to IE_α for species $\alpha = 1, 2$. If $\xi_{f\alpha}$ denotes the healing lengths for species $\alpha = 1, 2$, then the kinetic energy per particle due to the distortion of the wavefunction is again given by $KE_\alpha = \frac{\hbar^2}{2m_\alpha \xi_{f\alpha}^2}$. As discussed earlier, the healing lengths may be estimated using the conditions $KE_\alpha \approx IE_\alpha$. Explicitly, for the fermions,

$$\begin{aligned} \tilde{\xi}_{f1} &\sim \frac{1}{\sqrt{(k_{f1}L)^2 + 4\pi(\frac{m_1+m_2}{m_2})\tilde{g}_{12}\rho_2 L}} \equiv \frac{1}{\sqrt{S_{f1}}} \\ \tilde{\xi}_{f2} &\sim \frac{1}{\sqrt{(k_{f2}L)^2 + 4\pi(\frac{m_1+m_2}{m_1})\tilde{g}_{12}\rho_1 L}} \equiv \frac{1}{\sqrt{S_{f2}}} \end{aligned} \tag{3.11}$$

$\tilde{\xi}_{f\alpha} = \xi_{f\alpha}/L$ is dimensionless healing length for fermions and S_{f1} and S_{f2} are dimensionless quantity to simplify the scaling analyses of the healing lengths. We remark that in the expressions of the healing lengths, $k_{f\alpha}L = \pi\rho_\alpha/2$ where, ρ_α denotes the bulk density of the corresponding species α away from the hard wall or the interface.

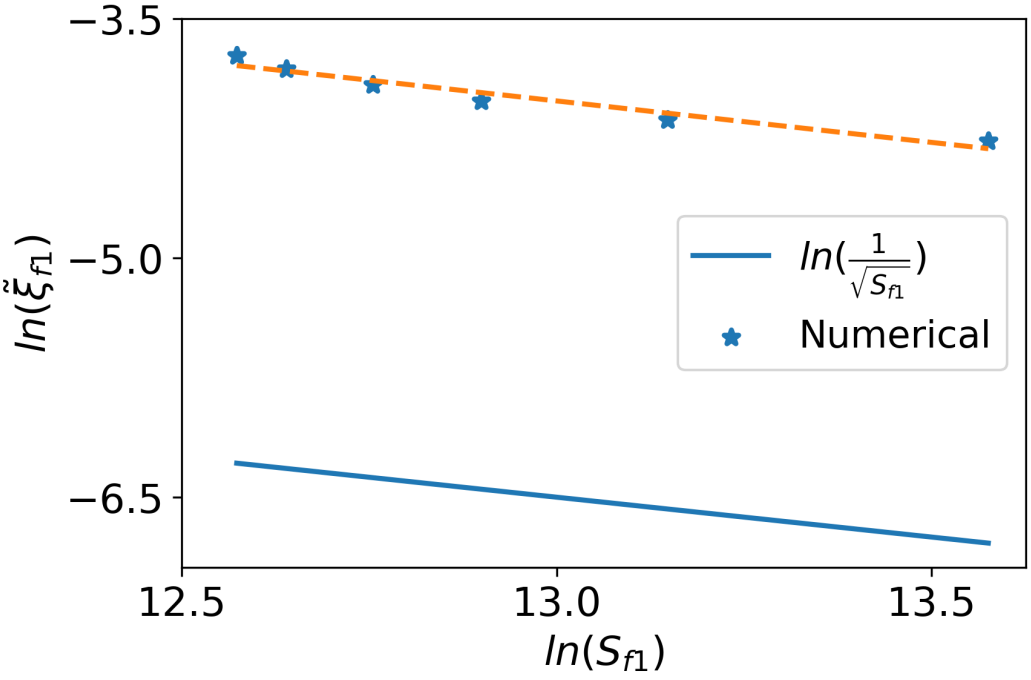

Figure 3.6: Scaling behavior of the healing lengths of species 1 at the interface of a fermion-fermion mixture in the two-chunk separation from the simulations and Eqs. 3.11. Here $N_1 = N_2 = 50$.

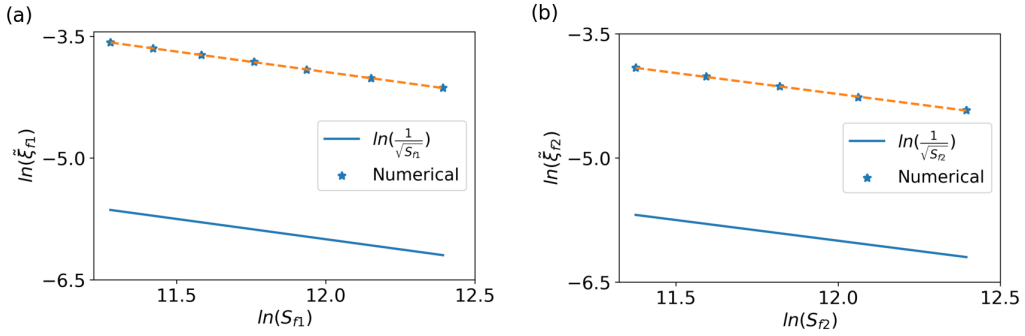

Figure 3.7: Scaling behavior of the healing lengths of species 1 (a) and species 2 at the interface of ^{6}Li - ^{86}Rb mixture in the two-chunk separation from the simulations and Eqs. 3.11. Here $N_1 = N_2 = 50$.

The scaling behavior of species 1 in fermion-fermion mixtures at the interface is demonstrated in Fig.(3.6). The agreement between the numerical outcomes and analytical formulas confirms the energy competition hypothesis. In the case of equal-mass fermion-fermion mixtures, the two-chunk structures are always symmetrical, eliminating the need to analyze the healing length for species 2 at the interface.

The scaling behavior of both species at the interface of a ^{6}Li - ^{86}Rb mixture in a two-chunk phase-separation is illustrated in Fig.(3.7). The numerical results again agree with the analytical formulas, demonstrating that the energy competition argument is effective in fermion-fermion mixtures in quasi-one-dimensional box potentials, regardless of the mass ratio.

CHAPTER 4
BINARY ATOMIC MIXTURES OF DIFFERENT SPIN STATISTICS IN BOX POTENTIALS

The results presented here have been published in Bishal Parajuli, Daniel Pecak and Chih-Chun Chien, *Atomic boson-fermion mixtures in one-dimensional box potentials: Few-body and mean-field many-body analyses*, Phys. Rev. A 107, 023308 [98].

Boson-fermion mixtures are of particular interest because the two components follow different spin-statistics, which sets them apart from purely bosonic or fermionic gases. The bosons can interact with themselves and with the fermions through two-body s-wave scattering, but identical fermionic atoms do not interact with each other due to Pauli exclusion principle that suppresses two-body s-wave scattering [1]. Here, we aim to investigate binary atomic boson-fermion mixtures in quasi-1D box potentials to better understand the complex phase diagrams, ground state properties, and interface structures.

We consider equal number of bosons and fermions $N_b = N_f = N$ confined in quasi-1D box of length L. We denote the masses of the bosons and fermions as m_b and m_f, respectively. For a binary boson-fermion mixture, there are two coupling constants from the two-body s-wave collisions: The intraspecies interactions between bosons, g_{bb}, and the interspecies interaction between bosons and fermions, g_{bf}. For single-component fermions, the Pauli exclusion principle suppresses two-body s-wave collisions between identical fermions, hence $g_{ff} = 0$. The non-vanishing coupling constants g_{bb} and g_{bf} can be respectively expressed in terms of the two-body s-wave scattering lengths a_{bb} and a_{bf} away from resonance by [1]

$$g_{b\alpha}^{3D} = 2\pi\hbar^2 a_{b\alpha}^{3D}/m_{b\alpha} \tag{4.1}$$

with the reduced mass $m_{b\alpha} = (1/m_b + 1/m_\alpha)^{-1}$, where $\alpha \in \{b, f\}$. Here $a_{b\alpha}^{3D} > 0$ (or < 0) corresponds to a repulsive (or attractive) interaction. In experiments, a magnetic field induced Feshbach resonance can be utilized to tune the 3D s-wave scattering length $a_{b\alpha}^{3D}$, leading to tunable interactions [1, 99]. In experiments, g_{bb} and g_{bf} may change together with the external magnetic field. Here we assume the two coupling constants can be tuned independently and map out the phase diagrams for selected atomic mixtures.

Quasi one-dimensional atomic gases can be realized by freezing the motion (with a tight confinement) in the transverse directions. Away from resonance, the coupling constant g_{1D} of a 1D atomic gas can be expressed in terms of a_{3D} via [100] $g_{b\alpha}^{1D} = \left(2\hbar^2 a_{b\alpha}^{3D}\right)/a_\perp^2$, where $a_\perp$ is the length scale associated with the tight confinement in the transverse directions. Hence, $g_{b\alpha}^{1D}$ can be tuned by adjusting

the ratio between $a_{b\alpha}^{3D}$ and $a_\perp$. We introduce the dimensionless parameters $\tilde{g}_{b\alpha}$ to rewrite the coupling constants as $g_{b\alpha} = \tilde{g}_{b\alpha} E_f^0 / k_f^0$.

In a mean-field treatment of many-body systems, the contact interaction is coarse-grained into a density-density interaction [1], which ignores the details of the wavefunction and only accounts for the energy change due to the overlap of the density profiles. The ground-state energy functional $E[\psi_b, \psi_{f,1}, \cdots, \psi_{f,N_f}]$ of a binary boson-fermion mixture in a 1D box potential can be written as

$$E = \int_0^L dx \Big[\frac{\hbar^2}{2m_b} N_b |\partial_x \psi_b|^2 + \frac{\hbar^2}{2m_f} \sum_{i \le N_f} |\partial_x \psi_{f,i}|^2 + \frac{1}{2} g_{bb} N_b^2 |\psi_b|^4 + g_{bf} N_b |\psi_b|^2 \sum_{i \le N_f} |\psi_{f,i}|^2 \Big] \tag{4.2}$$

Here $\sqrt{N_b}\psi_b$ is the condensate wavefunction and $\psi_{f,i}$ is the ith fermionic eigenstate. The normalization conditions $\int_0^L dx |\psi_b|^2 = 1$ and $\int_0^L dx |\psi_{f,i}|^2 = 1$ for all i are imposed.

In the mean-field description of the ground state, the condensate wavefunction describing the bosons is governed by the Gross-Pitaevskii equation [1, 69]. To find the minimal-energy configuration, we implement the imaginary-time formalism [1, 3] by searching for the stable solution to the imaginary-time evolution equation $-\partial \psi_b / \partial \tau = \delta E / \delta \psi_b^*$ in the $\tau \to \infty$ limit, starting from a trial initial configuration. The normalization $\int |\psi_b|^2 dx = 1$ is imposed at each imaginary-time increment to project out higher-energy states. Here $\tau = it$ is the imaginary time. Explicitly,

$$-\hbar \frac{\partial \psi_b}{\partial \tau} = -\frac{\hbar^2}{2m_b} \partial_x^2 \psi_b + g_{bb} \rho_b \psi_b + g_{bf} \rho_f \psi_b, \tag{4.3}$$

where, ρ_α with $\alpha \in \{b, f\}$ denotes the bosonic and fermionic density, respectively. Meanwhile, we describe the fermions by using the Hartree approximation, which leads to set of eigenvalue equations:

$$-\frac{\hbar^2}{2m_f} \frac{\partial^2 \psi_{f,i}}{\partial x^2} + g_{bf} \rho_b \psi_{f,i} = E_i \psi_{f,i}. \tag{4.4}$$

We choose the units so that $\hbar = 2m_f = 1$. The coupled equations of the bosons and fermions are then solved together to obtain a configuration for the boson-fermion mixture.

The density profiles can be obtained from the condensate wavefunction and fermion wavefunctions via

$$\rho_b = N_b |\psi_b|^2, \ \rho_f = \sum_{i \le N_f} |\psi_{f,i}|^2. \tag{4.5}$$

The total number of particles of each species is given by

$$N_\alpha = \int_0^L dx \rho_\alpha. \tag{4.6}$$

It is possible to obtain different solutions from different initial conditions that respect or violate the parity symmetry. In our numerical calculations, we have tried as many different initial states as possible and collected their final solutions. By comparing the ground-state energies via Eq. (4.2) from those different solutions, the lowest-energy state can be identified.

To quantify the homogeneity of the system, we introduce the following definition of homogeneity:

$$\mathfrak{h} = 1 - \int_0^L \frac{|\rho_b(x) - \rho_f(x)|}{N_b + N_f} dx. \tag{4.7}$$

Here the definition by construction gives $\mathfrak{h} = 0$ for the miscible (homogeneous) phase and $\mathfrak{h} = 1$ for total phase separation with no overlap between the densities of the two species.

Here we present the results from many-body mean-field theory of binary boson-fermion mixtures. The first case is with nearly equal masses, exemplified by a mixture of ^{7}Li and ^{6}Li, and then cases with larger mass imbalance will be presented, including ^{7}Li - ^{86}Rb and ^{6}Li - ^{87}Rb mixtures. Our method is general and applies to other atomic boson-fermion mixtures in 1D box potentials as well. Unless otherwise specified, we will present the results of $N_b = 50 = N_f$. We have verified that increasing the particle numbers does not introduce further features. A 1000-point grid is used to discretize the space, and we have checked the results are insensitive to a further refinement of the grid.

4.1 ^{7}Li–^{6}Li mixture

After solving the coupled equations of the binary boson-fermion mixtures in a 1D box and comparing the ground-state energies of possible solutions to pick the lowest-energy configuration, we identify the stable ground-state structures of a mixture of ^{6}Li and ^{7}Li.

4.1.1 Phase-diagram and density profiles

The $\tilde{g}_{bb}$-$\tilde{g}_{bf}$ phase diagram of the ground-state structures of a mixture of ^{6}Li and ^{7}Li is shown in Fig. 4.1(a). We also show the homogeneity $\mathfrak{h}$, defined in Eq. (4.7).

There are three possible structures: The miscible phase in the weak interspecies interaction region, two-chunk separation in the strongly interacting region, and three-chunk (or sandwich) separation in the intermediate regime. When $\mathfrak{h} \to 1$, the mixture is in the miscible phase and when $\mathfrak{h} \to 0$, the bosons and fermions are phase-separated (into either a three-chunk or two-chunk structure). Representatives of the three regimes of Fig. 4.1(a) are shown in Fig. 4.1(b), (c), and (d). In the miscible phase, there is a substantial overlap between the two species except the regions near the hard walls, where the wavefunctions are distorted by the boundary condition. In the three-chunk separation, the fermions congregate at the center, enclosed by the bosons on both sides. Finally, in the two-chunk separation, the bosons and fermions occupied opposite sides and break parity symmetry due to imperfections of the initial condition or fluctuations in the calculations. We remark that the total energies of different structures have been compared, and the most stable state is chosen for each set of parameters.

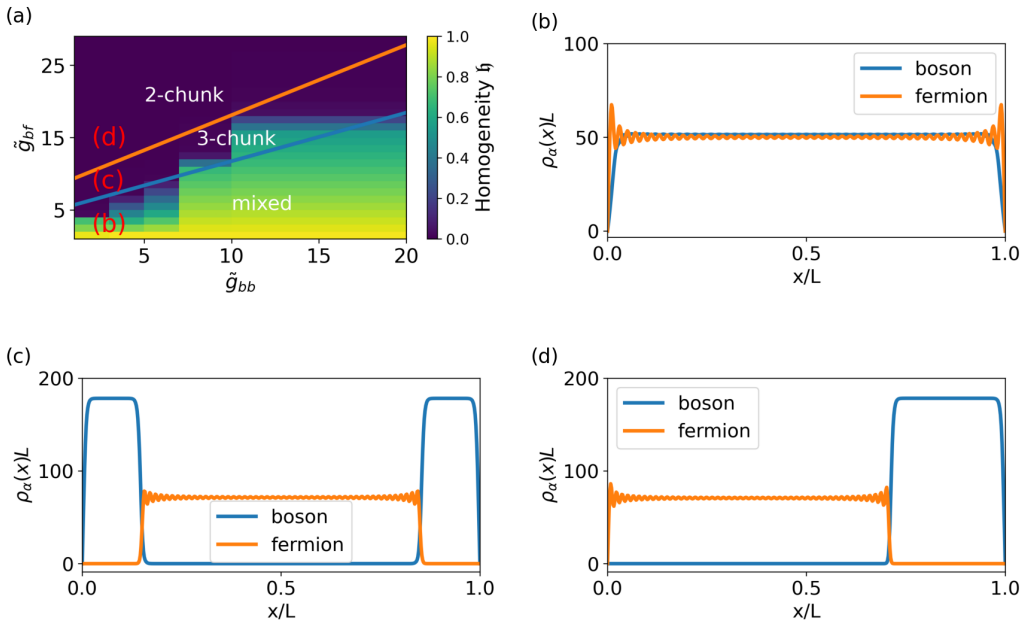

Figure 4.1: Phase diagram (a) and density profiles (b)-(d) of ^{7}Li–^{6}Li boson-fermion mixtures with mass ratio $m_b/m_f = 7/6$. Here $N_b = N_f = 50$ and $\tilde{g}_{bb} = 2$ with $\tilde{g}_{bf} = 2$ (b), $\tilde{g}_{bf} = 8$ (c), and $\tilde{g}_{bf} = 14$ (d) with their locations labelled on panel (a).

When compared to a previous analysis in an infinitely large system without boundary [47], one can see that the three-chunk structure from the mean-field calculation is only possible in the presence of the hard walls. This is because the fermions already have the main contribution to the kinetic energy from the

piling-up of the Fermi sea, so they are less sensitive to the distortion at the hard walls. On the other hand, the bosons with finite $\tilde{g}_{bf}$ can have a smoother profile when interfacing with the fermions than with the hard walls. Therefore, the mean-field result of the three-chunk structure in a box potential shows the influence of geometry on quantum systems. One may observe that the repulsive boson-boson interaction competes with the influence of the repulsive boson-fermion interaction. This is because the condensate of bosons has negligible kinetic energy, so the bosonic self-interaction plays the role of the Fermi pressure and pushes the other species.

On the other hand, a two-chunk structure breaks the parity symmetry in a box potential. If a calculation and its conditions respect the parity symmetry, two-chunk structures will not emerge in the density profile. In our few-body calculations, we analyze the correlations to reveal the underlying two-chunk structure. In our mean-field calculations, however, we use fluctuations in the initial conditions to break the parity symmetry and confirm the two-chunk structure with separating densities becomes the most stable in the strong-interaction regime. For realistic situations in experiments, fluctuations in the preparation, trapping, and manipulations of atoms in the strong-interaction regime may also break the parity symmetry and result in the stable two-chunk structure.

A closer examination of Fig. 4.1(b), (c), (d) suggests that increasing the repulsive boson-fermion interaction tends to reduce the width of the overlap between the two species. This is expected because the overlap region incurs high interaction energy. In the following, we will analyze the interface properties of the mixtures.

4.1.2 Interface properties

Let us consider pure bosons in a box of length L with hard walls, $\psi_b \to 0$ at the walls and ψ_b approaches the constant bulk value away from the boundary. The distance over which the wavefunction rises from zero at the wall to its bulk value is often referred to as the healing (or coherence) length [1, 3]. Near the wall, ψ_b is governed by a competition between the kinetic and interaction energies. If we denote the length scale of the variation of the bosons at the wall by ξ_b, the kinetic energy per particle due to the distortion of the wavefunction is given by

$$KE = \frac{\hbar^2}{2m\xi_b^2}. \tag{4.8}$$

The healing length of bosons is defined as the length scale at which the kinetic energy per particle matches the interaction energy per particle, $g_{bb}\rho_b$. This leads

to an estimation

$$\xi_b = \frac{\hbar}{\sqrt{2m_b g_{bb}\rho_b}} \tag{4.9}$$

The stability of a BEC to a localized perturbation is determined by the healing length as it is dependent on the balance between kinetic energy and interaction energy, as well as the interaction strength between the particles.

By defining $\tilde{\xi}_b = \xi_b/L$ as a dimensionless quantity, the scaling of the healing length is

$$\tilde{\xi}_b \sim \sqrt{\frac{m_f}{m_b k_f^0 L}} \frac{1}{\sqrt{\tilde{g}_{bb}\rho_b L}} \equiv \frac{1}{\sqrt{S_{bw}}}. \tag{4.10}$$

Here we define a dimensionless parameter $S_{bw} \equiv \tilde{g}_{bb}\rho_b k_f^0 L^2 m_b/m_f$ to simplify the scaling analysis. The presence of the fermionic parameters is only to fix the units.

Meanwhile, the length scale of the variation of fermions at the wall, denoted by ξ_f, may be determined by matching the kinetic energy per particle with the Fermi energy. The reason is because Pauli exclusion principle may be viewed as an effective (statistical) interaction between fermions, leading to an energy scale determined by the Fermi energy E_f. The balance $KE_f = \hbar^2/(2m_f\xi_f^2) \sim E_f$ then leads to $\xi_f \sim \frac{1}{k_f}$. Here k_f is the bulk Fermi wavevector, determined by the bulk fermion density ρ_f via $k_f = \pi\rho_f/2$. In terms of the dimensionless healing length $\tilde{\xi}_f = \xi_f/L$, we have

$$\tilde{\xi}_f \sim \frac{1}{k_f L} \equiv \frac{1}{\sqrt{S_{fw}}}. \tag{4.11}$$

Here we define another dimensionless parameter $S_{fw} \equiv (k_f L)^2$ to simplify the scaling analysis.

Now we consider two-chunk separation in the strong-interaction regime, where the bosons occupy one side of the box while the fermions occupy the other side. In such configurations, there is practically only one species near each hard wall. In our analyses of the healing lengths, we take the width as the distance between 95% and 5% of the value of $\sqrt{\rho_\alpha}$ at the plateau in the bulk. Taking different criteria or using functional fits to the density profiles leads to basically the same scaling behavior, which verifies the robustness of the energy-competition argument. Fig. 4.2 shows the scaling of the healing lengths of the bosons and fermions near the hard walls, respectively. The scaling behavior confirms the arguments based on the competition of the kinetic and interaction energies for each species. We note that the energy-competition arguments do not fix the pre-factors of the healing lengths, causing a parallel shift between the data and analytic formulas on a log-log plot.

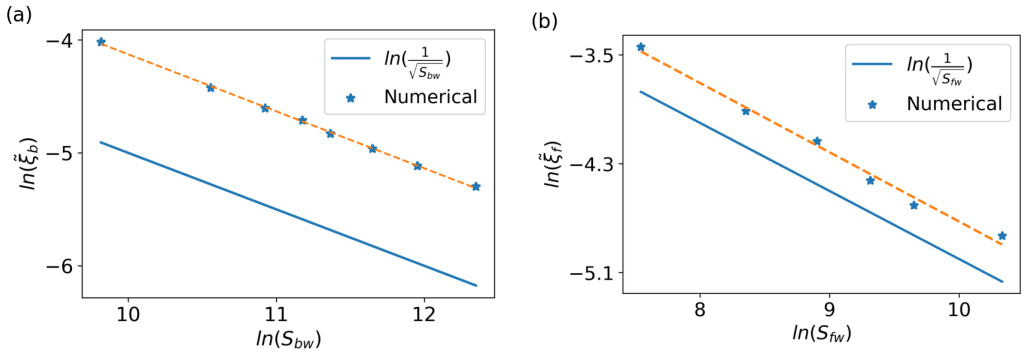

Figure 4.2: Healing lengths of (a) bosons and (b) fermions at the opposite boundaries of the box potential for a ^{7}Li–^{6}Li mixture from the simulations and Eqs. (4.10) and (4.11). Here $N_b = N_f = 50$ in (a) and (b) with $\tilde{g}_{bf} = 40$ in (a) and $\tilde{g}_{bb} = 1,\ \tilde{g}_{bf} = 10$ in (b).

In the phase-separation structures, both species are present at the interface between the two species. The interaction energy (IE) per particle of the bosons and fermions at the boson-fermion interface may be respectively estimated as

$$IE_b = g_{bb}\rho_b + g_{bf}\rho_f,\ IE_f = E_f + g_{bf}\rho_b. \tag{4.12}$$

For the fermions, Pauli exclusion principle may be considered as an effective (statistical) interaction, which introduces the Fermi energy E_f to IE_f. If ξ_α denotes the healing lengths for species $\alpha = b, f$, then the kinetic energy per particle due to the distortion of the wavefunction is again given by $KE_\alpha = \frac{\hbar^2}{2m_\alpha\xi_\alpha^2}$. As discussed earlier, the healing lengths may be estimated using the conditions $KE_\alpha \approx IE_\alpha$. Explicitly, for the bosons, $\frac{\hbar^2}{2m_b\xi_b^2} \sim g_{bb}\rho_b + g_{bf}\rho_f$, which leads to

$$\tilde{\xi}_b \sim \sqrt{\frac{m_f}{m_b k_f^0 L}}\frac{1}{\sqrt{\tilde{g}_{bb}\rho_b L + \tilde{g}_{bf}\rho_f L}} \equiv \frac{1}{\sqrt{S_{bi}}}. \tag{4.13}$$

For the fermions, $\frac{\hbar^2}{2m_f\xi_f^2} \sim \frac{\hbar^2 k_f^2}{2m_f} + g_{bf}\rho_b$, which leads to

$$\tilde{\xi}_f \sim \frac{1}{\sqrt{(k_f L)^2 + \tilde{g}_{bf}(\rho_b L)(k_f^0 L)}} \equiv \frac{1}{\sqrt{S_{fi}}}. \tag{4.14}$$

Similar to the analyses of the healing lengths at the hard walls, here we define two dimensionless parameters $S_{bi} \equiv [\tilde{g}_{bb}\rho_b L + \tilde{g}_{bf}\rho_f L]m_b k_f^0 L/m_f$ and $S_{fi} \equiv [(k_f L)^2 + \tilde{g}_{bf}\rho_b k_f^0 L^2]$ to simplify the scaling analyses of the healing lengths at the boson-fermion interface. We note that when comparing the analyses of the healing lengths at the hard walls versus those at the boson-fermion interface, the

expressions of $S_{\alpha i}$ for $\alpha = b, f$ are consistent with those of $S_{\alpha w}$ because only one species is present near each hard wall in two-chunk phase separation but both species are present at the boson-fermion interface.

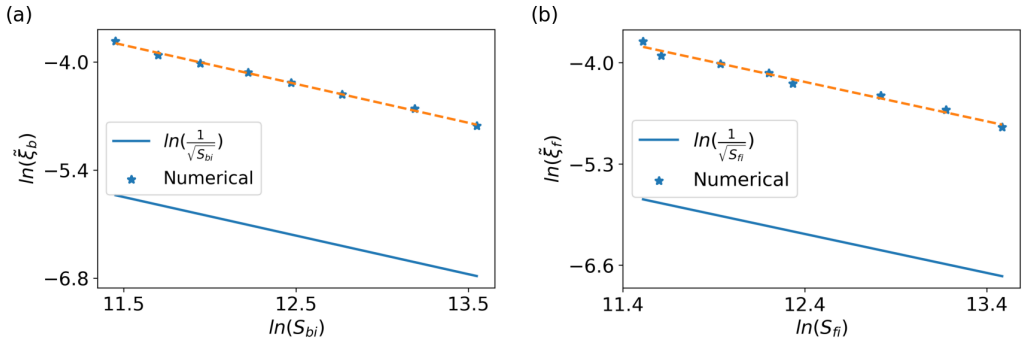

Figure 4.3: Healing lengths of (a) bosons and (b) fermions at the interface of a ^{7}Li–^{6}Li mixture in a two-chunk structure from the simulations and Eqs. (4.13) and (4.14). Here $N_b = N_f = 50$ in (a) and (b).

We remark that in the expressions of the healing lengths, ρ_α denotes the bulk density of the corresponding species away from the interface or hard wall, and $k_f^0 = \pi N_f/2L$ is the non-interacting Fermi wavevector while $k_f = \pi\rho_f/2$ is the bulk Fermi wavevector of the fermions in the mixture. The interface widths for both species from the simulation results can be obtained from the density profiles by following the same analyses as we did for the healing lengths at the hard walls. Moreover, we have verified that taking different criteria or using functional fits to the density profiles basically leads to the same scaling behavior.

Fig. 4.3 shows that the healing lengths of the bosons and fermions at the interface scale according to Eqs. (4.13) and (4.14), respectively, in the two-chunk regime shown in Fig. 4.1. Since testing the scaling behavior requires a broad range of parameters, the two-chunk regime is more appropriate because the three-chunk regime is narrow along the $\tilde{g}_{bf}$ direction. The agreement of the scaling behavior between the simulations and analytical formulas of the healing lengths verifies that the energy-competition argument works well with binary boson-fermion mixtures in a 1D box. We remark that more complicated analyses with constructions of piece-wise energy functional [101–103] may lead to refinements of the structures and interface widths, which will in turn determine the pre-factors of the healing lengths that cannot be explained by the scaling analysis. Nevertheless, the simple scaling from energy-competitions provides us the main physical meaning for explaining future experiments on atomic boson-fermion mixtures.

4.2 ^{87}Rb-^{6}Li mixture

For boson-fermion mixtures with prominent mass imbalance, we first analyze mixtures of ^{87}Rb and ^{6}Li. This system also exhibits the miscible phase, three-chunk separation, and two-chunk separation of the two species as the inter-species interaction increases.

4.2.1 Phase-diagram and density profiles

Fig. 4.4(a) shows the phase diagram of ^{87}Rb and ^{6}Li mixtures. Fig. 4.4(b), (c), and (d) show the representative density profiles of the miscible phase in the weak inter-species interaction regime, three-chunk (sandwich) separation in the intermediate interaction regime, and the two-chunk separation in the strong interaction regime, respectively. Heavier mass lowers the kinetic energy due to distortion of the density profile in a phase-separation structure because the mass appears in the denominator of the kinetic energy. To minimize the kinetic energy due to the distortion of the wavefunction in the three-chunk structure, the density of the lighter species tends to stay away from the hard walls while the heavier species tends to occupy the region there until the two-chunk structure becomes energetically more favorable than the three-chunk structure.

4.2.2 Interface properties

The healing lengths of the bosons and fermions with larger mass imbalance at the hard walls in a 1D box are found to follow the same scaling as their counterparts in the ^{7}Li–^{6}Li mixture. Hence, we do not repeat the analysis of ξ_α at the hard walls. For the interface between the two species, we found that since the three-chunk structure exists in a narrow parameter range, it is more challenging to analyze the scaling behavior. Therefore, the interface properties of the mixtures are discussed only for the two-chunk structure that extends well into the strongly interacting regime.

For ^{87}Rb - ^{6}Li mixtures, we found that the healing lengths of the bosons and fermions at their interface scale according to Eqs. (4.13) and (4.14), respectively. The scalings of the healing lengths with interactions are shown in Fig. 4.5, which confirm that the widths of the bosons and fermions at the interface are determined by competitions between the kinetic energy due to the distortion of the density and the interaction energy, which includes the inter- and intra- species interactions and the effective (statistical) interaction of fermions. Furthermore,

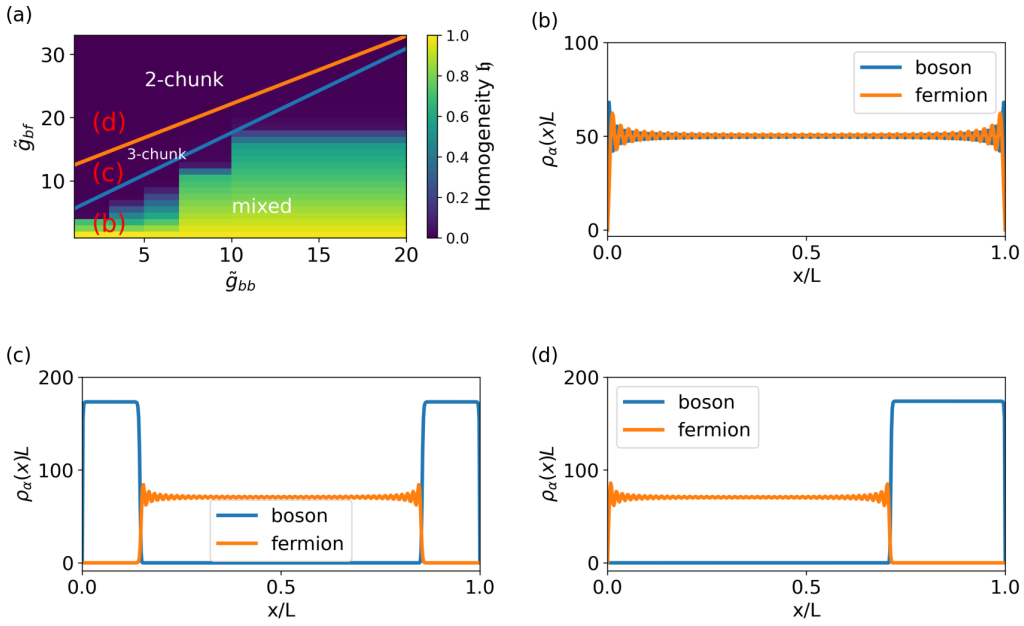

Figure 4.4: Phase diagram (a) and density profiles (b)-(d) of ^{87}Rb–^{6}Li mixtures. Here $N_b = N_f = 50$ and $\tilde{g}_{bb} = 2$ with $\tilde{g}_{bf} = 2$ (b), $\tilde{g}_{bf} = 10$ (c), and $\tilde{g}_{bf} = 18$ (d) with their locations labelled on panel (a).

the scaling analyses correctly capture the power-law dependence of the healing lengths of the bosons and fermions at the phase-separation interface and verify the energy-competition argument.

4.3 ^{7}Li-^{86}Rb mixture

4.3.1 Phase-diagram and density profiles

Here we consider a ^{7}Li-^{86}Rb mixture as an example of light bosons and heavy fermions. The phase diagram is shown in Fig. 4.6(a) with a relatively large three-chunk regime when the boson-boson interaction is weak. Interestingly, we could not reach the regime in the few-body calculations to observe two-chunk separation in ^{7}Li-^{86}Rb mixture due to the demanding computation, which implies that the parameter space for the three-chunk structure is relatively large. This is indeed the case from the many-body result.

For the three-chunk structure, the boson is now in the center of the box be-

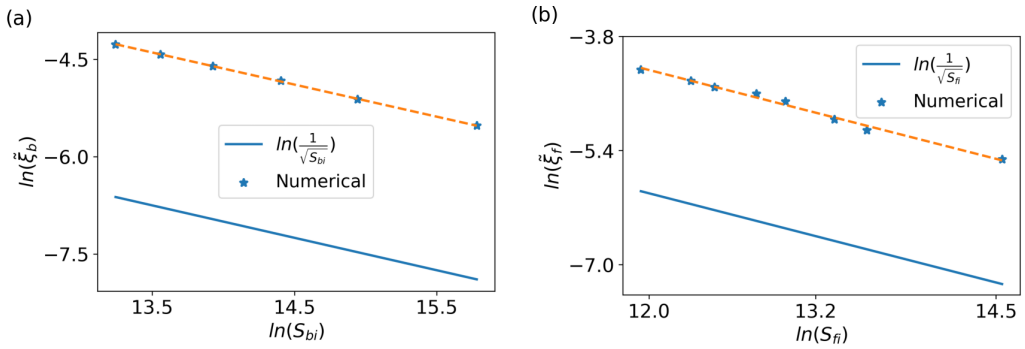

Figure 4.5: Scaling behavior of the healing lengths of (a) bosons and (b) fermions at the interface of a ^{87}Rb - ^{6}Li mixture in the two-chunk separation from the simulations and Eqs. (4.13) and (4.14). Here $N_b = N_f = 50$ in (a) and (b).

cause the kinetic energy is relatively small for the heavy fermions, which tend to stay near the hard walls and push the bosons away from the hard walls. Meanwhile, the bosons rely on the boson-boson interaction to build up pressure to push against the fermions. Hence, the three-chunk structure remains energetically more favorable than the two-chunk structure when $\tilde{g}_{bb}$ is weak and the bosons cannot repel the fermions at both hard walls. When $\tilde{g}_{bf} >> \tilde{g}_{bb}$, however, the bosons are tightly compressed by the fermions and eventually pushed to one side of the box to form a two-chunk structure with lower total energy.

4.3.2 Interface properties

Since the density profiles of the ^{7}Li - ^{86}Rb mixture in the two-chunk regime are similar to those of the ^{87}Rb - ^{6}Li mixture, the analyses of the widths that reflect the healing lengths at the phase-separation interface are also similar. We again focus on the two-chunk regime due to its broad coverage of the strong-interaction region on the phase diagram. The scaling of the healing lengths with the interactions are shown in Fig. 4.7. The same scaling analysis confirms the functional dependence of the healing lengths of the bosons and fermions described by Eqs. (4.13) and (4.14) at the phase-separation interface, showing the generality of the energy-competition argument. We mention that the scaling analyses only reveal the functional forms of the healing lengths, and the pre-factors need to be determined from simulations or direct evaluations of the energy functional for the inhomogeneous systems. Moreover, we have verified the scaling of the healing lengths with more particle numbers or grid points, and the functional forms remain the same because of the energy-competition

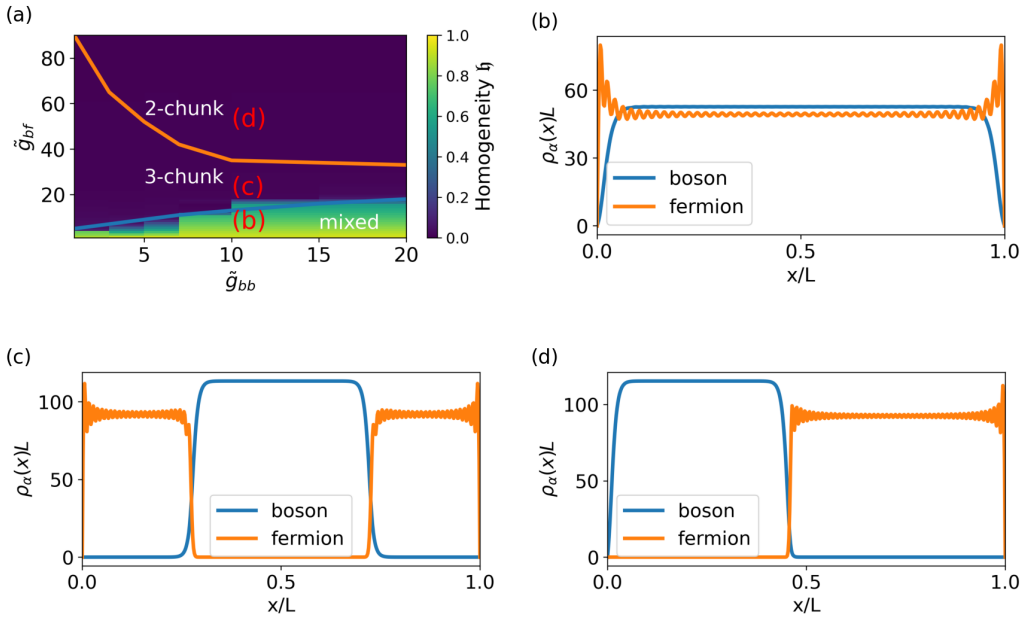

Figure 4.6: Phase diagram (a) and density profiles (b)-(d) of ^{7}Li–^{86}Rb boson-fermion mixtures. Here $N_b = N_f = 50$ and $\tilde{g}_{bb} = 10$ with $\tilde{g}_{bf} = 5$ (b), $\tilde{g}_{bf} = 20$ (c), and $\tilde{g}_{bf} = 50$ (d) with their locations labelled on panel (a).

mechanism.

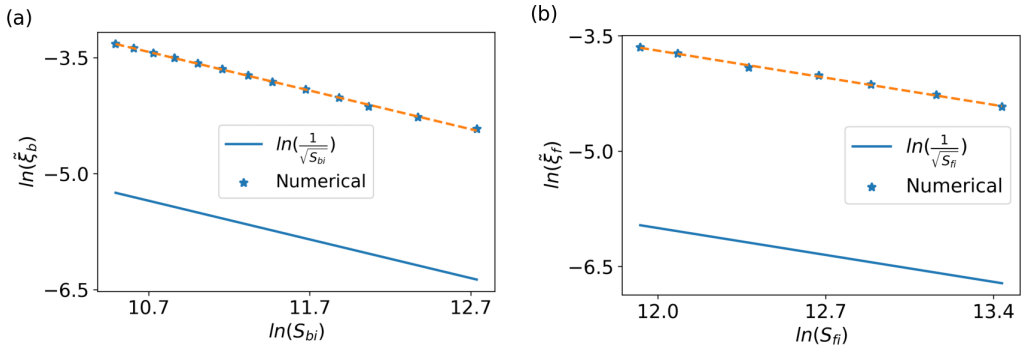

Figure 4.7: Healing length of (a) bosons and (b) fermions at the interface of a ^{7}Li - ^{86}Rb mixture in the two-chunk separation from the simulations and Eqs. (4.13) and (4.14). Here $N_b = N_f = 50$ in (a) and (b).

CHAPTER 5

PROXIMITY EFFECT AND SPATIAL KIBBLE-ZUREK MECHANISM IN ATOMIC FERMI SUPERFLUID

The results presented here have been published in Bishal Parajuli and Chih-Chun Chien, *Proximity effect and spatial Kibble-Zurek mechanism in atomic Fermi gases with inhomogeneous pairing interactions*,
https://doi.org/10.48550/arXiv.2303.11213 [104].

In this chapter, we introduce spatially controllable inhomogeneous interactions for attractive Fermi gases to study two different phenomena, proximity effect and spatial Kibble-Zurek mechanism (KZM) in a unified mean-field platform. We consider interaction quenches in real space viz step-function quench resembling proximity effect setup and spatial quench depicting spatial KZM. Bogoliubov-de-Gennes (BdG) equations were used to obtain the profiles of pair wavefunction and pair correlation function to extract the correlation lengths and explain their scaling behavior. The results are compared with the known results for both proximity effect and spatial KZM. Moreover, we discuss the relevant experimental techniques that may realize and verify the inhomogeneous phenomena.

5.1 Proximity effect in superconductors

When a superconductor (SC) is in contact with a normal metal (NM), the Cooper pairs from the SC penetrate into the NM with a characteristic length determined by the BCS coherence length [73,74], a phenomenon known as the proximity effect. The NM acquires some properties of the SC, such as a reduction in the resistance and the ability to carry a super-current [105]. The proximity effect results from a sudden change of the pairing interaction across the SC-NM interface, so it may be thought of as a phase transition in space. The proximity effect in other hetero-structures have been extensively studied, including a superconductor-quasicrystal hybrid ring [106], disordered and quasi-periodic systems [107], superconducting thin films [108] and normal metal- superconducting slab [109]. Experimental [110, 111] and theoretical [109, 112–114] studies of niobium-gold layers suggest that the proximity effect may create topological superconductivity. Moreover, transport properties were studied theoretically by the interplay between proximity effect and multiple Andreev reflections in case of superconductor-normal metal- superconductor (SNS) junctions [115]. Ref . [116] has discussed proximity effect for bi-layers that can be modified in case of random mixtures. In addition, experimental data of granular SC-NM structures are shown to agree with the theory [73] in the weak coupling limit. Investigations

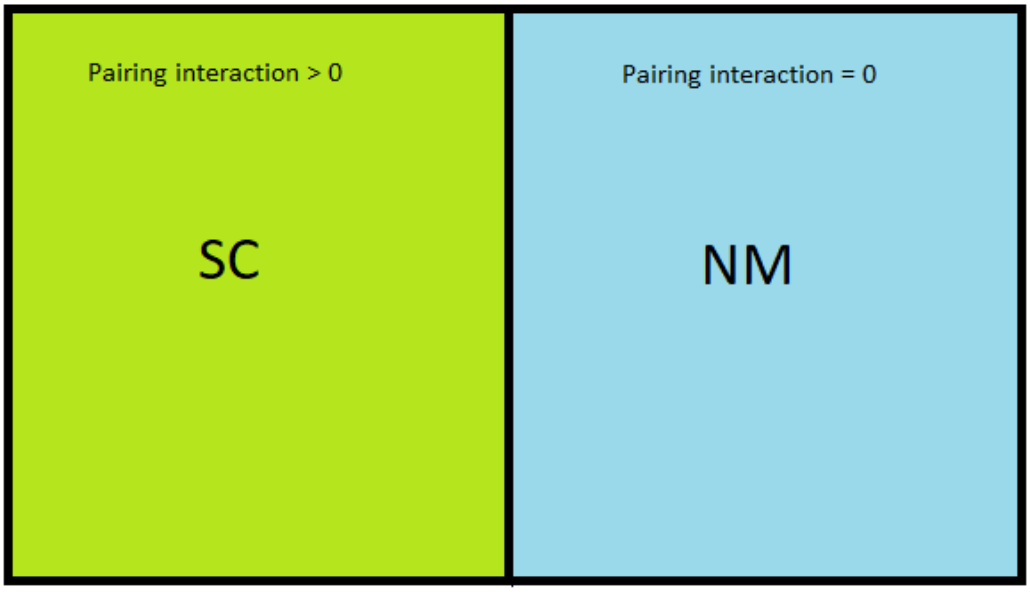

Figure 5.1: Typical setup for proximity effect in superconductors.

[117–119] of graphene mono-layers and bi-layers have shown a suppression of the critical current at the superconductor-graphene-superconductor junctions [118] and by the calculation of decaying order parameter at the interface of the junction by using tight-binding BdG formalism [117]. In addition to the proximity effect, inverse proximity effect is also considered in the investigations, for example-consequences of the inverse proximity effect from the normal metals to the superconductor and non-equilibrium heating were taken in account to determine the heat and charge transport in case of normal metal-insulator-superconductor-insulator-normal metal junctions [120]. Furthermore, there has been extensive research on the proximity effect of ferromagnet-superconductor hetero-structures [121], which may give rise to the Majorana bound state [122].

In the study of proximity effect in a SC-NM junction, the pairing interaction is assumed to vanish across the interface. Previous studies [73,74,105] modeled the leakage of Cooper pairs from the superconductor into the normal metal with a characteristic length associated with the BCS coherence length. The decay of $F(x)$ in the normal region at finite temperatures has the exponential form [73,74]

$$F(x) \sim F_0 e^{-(x-x_c)/\xi_F},\ T > 0. \tag{5.1}$$

Here ξ_F is the correlation length associated with F. However, at zero temperature, $F(x)$ is no longer decaying exponentially with the distance $y = x - x_c$ from the interface. Instead, it follows a power law $1/y$, as shown in Refs. [73–75].

Thus, the scaling behavior is

$$\frac{F(x)}{\tilde{\Delta}}\frac{1}{k_f} \sim \frac{\xi_F}{x - x_c},\ T = 0. \tag{5.2}$$

Here $\tilde{\Delta} = \Delta/E_f^0$ is the dimensionless bulk gap in the superfluid region. The scaling behavior was obtained by solving the Gor'kov equation in Refs. [73,74] and verified in SC-NM hybrid rings [107], superconducting thin films [108], niobium-gold layers [114], and normal metal on top of a superconducting slab [109]. The reason for the slower power-law decay of $F(x)$ into the normal metal at zero temperature is because thermal excitations are absent in restricting the penetration of Cooper pairs.

5.2 Phase transitions and Kibble-Zurek mechanism

The Kibble-Zurek mechanism (KZM) [123–126] studies the reaction of a system crossing a continuous phase transition. The systems can be driven by a time-dependent or time-independent ramp. The KZM has inspired a plethora of theoretical [76–78,127–144] and experimental [145–156] studies to verify or compare the KZ scaling. The majority of the investigations have focused on time-dependent quenches of the parameters, where the excitations follow a power-law dependence of the transition rate [131, 132, 134, 138], including the Bose-Hubbard model [139–143] and spinor Bose-Einstein condensates (BEC) [78,144]. As a system approaches a critical point within ϵ, the reaction time τ diverges as $\tau \sim |\epsilon|^{-\nu z}$, which determines how fast the system can react. After the system is driven into the broken-symmetry phase, the density of topological excitation reflects the frozen correlation length $\xi \sim \tau_Q^{\frac{\nu}{1+\nu z}}$, where τ_Q is the characteristic quench time, and ν and z are the critical exponents from the corresponding phase transition. Dynamics of the ground state of Fermi superfluid following a time quench has also been studied [157].

Meanwhile, the time-independent KZM, also known as the spatial KZM, considers a linear ramp of the interaction and analyzes the scaling in the vicinity of a critical point in real space separating a broken-symmetry phase and a symmetric phase. The spatial KZM has been formulated and summarized in Refs. [76–78] with applications to the quantum transverse-field Ising model [76,77] and spin-1 BEC [78]. The analysis of the order parameter or correlation function reveals the critical exponent from the theory of phase transition in uniform systems in the thermodynamic limit. In a spatial KZM, the order parameter or its correlation function penetrates into the symmetric phase. Different from the abrupt drop of the interaction in the proximity effect, the linear ramp of the interaction introduces additional length scale. The correlation length ξ

diverges near the critical point as $\xi \sim |\epsilon|^{-\nu}$ in a uniform system. In the spatial KZM, the correlation freezes out within the transition region, which in turn determines the characteristic length of the penetration into the symmetric phase. The correlation length on the symmetric phase side follows the scaling behavior $\xi \sim \alpha^{-\nu/(1+\nu)}$. Here α measures the slope of the ramp in real space, which is the counterpart of the quench rate in a time-dependent quench. Importantly, the spatial KZM keeps the whole system in equilibrium, which is very different from the nonequilibrium nature of the time-dependent KZM. The trade-off is that the spatial KZM only determines one exponent ν instead of two in the time-dependent KZM. A previous theoretical study analyzed possible structures of atomic Fermi gases with inhomogeneous pairing interactions [158] but did not explore the spatial KZM.

In the spatial KZM, one considers a dimensionless parameter ϵ to identify the distance to the critical point x_c:

$$\epsilon(x) = \alpha(x - x_c). \tag{5.3}$$

We choose $x < x_c$ to represent the broken-symmetry (superfluid) phase and $x > x_c$ to represent the symmetric (normal-gas) phase. Similar to the freezing-out of the correlation length in the time-dependent KZM, the correlation length of the spatial KZM can freeze out in the transition region when the interaction drop to zero. Near the critical point x_c, the local correlation length diverges as $\xi \approx (\alpha|x_c - x|)^{-\nu}$. Here ν is the critical exponent for correlation length [76]. Within a distance x_h from x_c, the correlation length gets to the same order as the distance: $|x_h - x_c| \approx (\alpha|x_c - x_h|)^{-\nu}$. This sets a frozen correlation length of

$$\xi \sim \alpha^{-\frac{\nu}{1+\nu}}. \tag{5.4}$$

Here ξ determines the characteristic distance over which the correlation function can adjust itself to the varying ϵ. Thus, the spatial KZM predicts that the penetration of the correlation function into the symmetric phase with a characteristic length ξ.

5.3 Quenching of interaction in real space

To study the analogues of the proximity effect and spatial KZ mechanism using atomic Fermi gases in a quasi 1D box potential of length L, we consider spatially dependent attractive interaction $g_{ff}(x)$ between the two components. We use the Fermi energy E_f^0 and Fermi wavevector k_f^0 of a noninteracting Fermi gas with the same particle number to rewrite physical quantities in dimensionless forms. For example, the dimensionless interaction strength $\tilde{g}_{ff}(x)$ is defined by $g_{ff}(x) = -\tilde{g}_{ff}(x)E_f^0/k_f^0$.

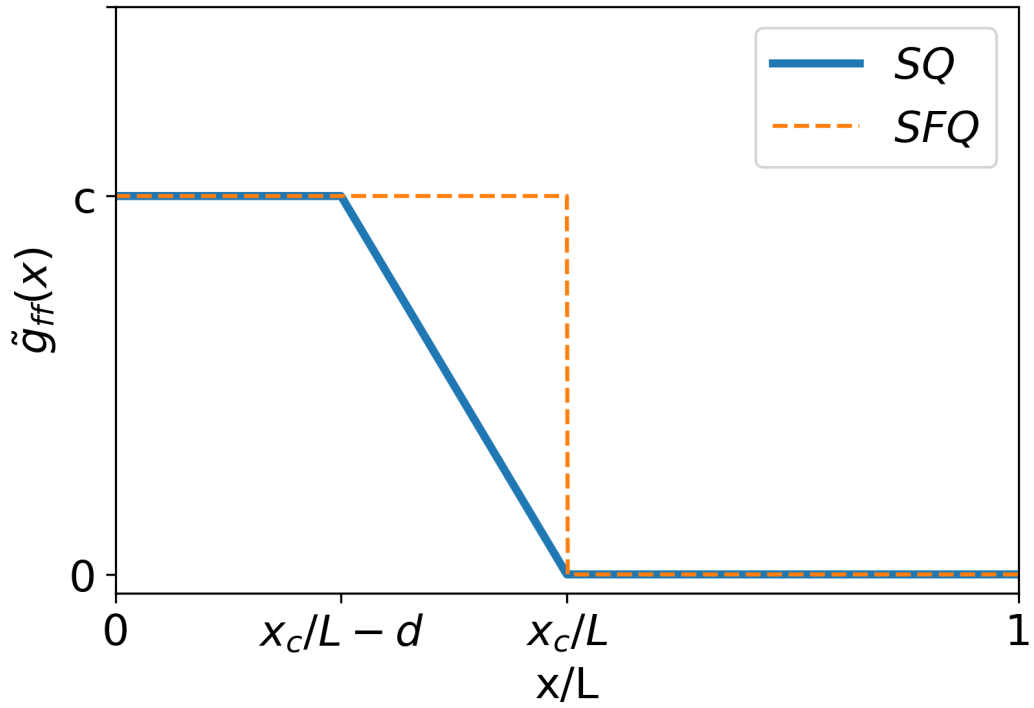

Figure 5.2: Illustrations of the spatial quench (SQ, solid line) and step-function quench (SFQ, dashed line) of the pairing interaction.

5.3.1 Step-function quench

To simulate the sudden drop in the interaction, we consider the step-function quench of the pairing interaction that vanishes suddenly at $x = x_c$. For the step-function quench,

$$\tilde{g}_{ff}(x) = \begin{cases} c, & 0 \leq x/L < x_c/L, \\ 0, & 1 > x/L > x_c/L. \end{cases} \tag{5.5}$$

We typically set $x_c = L/2$. The interaction profile is illustrated in Fig. 5.2.

5.3.2 Spatial quench

On the other hand, to investigate the spatial KZ mechanism, we consider a more general type of quench of the pairing interaction. For a spatial quench,

$$\tilde{g}_{ff}(x) = \begin{cases} c, & 0 \leq x/L < x_c/L - d, \\ -\frac{c}{d}\frac{(x-x_c)}{L}, & (x_c/L - d) \leq x/L \leq x_c/L, \\ 0, & 1 > x/L > x_c/L. \end{cases} \tag{5.6}$$

Again, we typically set $x_c = L/2$. Here c and d are dimensionless parameters. $-c/d$ is the slope of the linear ramp shown in Fig. 5.2. For the spatial quench studied here, we identify the parameter as $\alpha = \frac{c}{dL}$, so $\tilde{g}_{ff}(x) = -\alpha(x - x_c)$ in the ramp-down region and remark that the sign convention does not affect the scaling analysis.

5.4 Results and discussions

Here, we present the numerical calculation procedures and discuss the results for step-function quench and spatial quench.

5.4.1 Numerical calculations

We numerically solve the BdG equations as discussed in Chapter 2 Section 2.5.1 to find the measurable quantities from the eigenfunction solutions $\begin{pmatrix} u_{\tilde{n}} \\ v_{\tilde{n}} \end{pmatrix}$ of the BdG equations. The fermion density of each component is $\rho_\sigma(x) = \langle \psi_\sigma^\dagger(x)\psi_\sigma(x)\rangle$, and the total density $\rho_f(x) = \sum_\sigma \rho_\sigma(x)$ becomes

$$\rho_f(x) = 2\sum_{\tilde{n}}{}' |v_{\tilde{n}}(x)|^2. \tag{5.7}$$

The total fermion number is $N_f = N_\uparrow + N_\downarrow = \int_0^L \rho_f(x)dx$. The gap function is given by

$$\Delta(x) = -g_{ff}(x)\sum_{\tilde{n}}{}' u_{\tilde{n}}(x)v_{\tilde{n}}(x). \tag{5.8}$$

However, we distinguish the pairing correlations from the gap function, which is necessary in studying Fermi gases with inhomogeneous interactions. The pair wavefunction is [159]

$$F(x) = \langle \psi_\downarrow(x)\psi_\uparrow(x)\rangle = \sum_{\tilde{n}}{}' u_{\tilde{n}}(x)v_{\tilde{n}}(x). \tag{5.9}$$

The primed summation $\sum_{\tilde{n}}{}'$ in the above equations refer to the summation over positive energy states only. We also consider the pair-pair correlation function given by

$$C(r) = \overline{F(x)F(x+r)}. \tag{5.10}$$

Here the over-line denotes an average over x. The correlation function is important in defining the critical exponent in homogeneous systems [160] and extracting the exponents in systems with inhomogeneous interactions.

The number of grid points n_x to discretize the real space imposes a momentum cutoff $k_{max} = \frac{\pi n_x}{2L}$. We choose n_x large enough that the results are insensitive to further changes of n_x. Most of our calculations are for half filling with $n_x = N_f$. The results not far away from half filling are qualitatively the same. However, physical quantities may have relatively large fluctuations far way from half filling due to the small ratio of $\Delta(x)/E_f^0$.

In both step-function and spatial quenches, $\Delta(x)$ drops to zero when $g_{ff}(x) = 0$ according to Eq. (5.8). However, the pair wavefunction $F(x)$ can penetrate into the normal region with $g_{ff}(x) = 0$. We will analyze the penetration in different settings and characterize the correlation length ξ. The correlation function on the non-interacting side according to Eq. (5.10) can be evaluated by

$$C(r) = \frac{1}{n_x - r'} \sum_{n+r' \leq n_x} F(x_n) F(x_{n+r'}), \tag{5.11}$$

where $r = r'dx$, $n = 1, \cdots, n_x$ and $r' = 1, \cdots, n_x/2$ are integers.

To extract the exponents from the quench protocols, we fit $F(x)$ in the non-interacting region by the exponential form (5.1) and the power-law form (5.2). Interestingly, while the power-law fits $F(x)$ better in both step-function and spatial quenches, the exponential form may produce similar exponents even though the fitting does not faithfully go through the data. On the other hand, fitting the pair-pair correlation function $C(r)$ with a power-law similar to Eq. (5.2) results in significant deviations in both step-function and spatial quenches, but $C(r)$ can be fitted reasonably well with the exponential function $C_0 \exp(-r/\xi_C)$. We extract the correlation lengths from $F(x)$ and $C(r)$ and denote them by ξ_F and ξ_C, respectively, and introduce the dimensionless quantities $\tilde{\xi}_{C,F} = \xi_{C,F}/L$. Moreover, we evaluate the BCS coherence length [3, 159]

$$\xi_\Delta = \frac{\hbar^2 k_f}{m\Delta} \tag{5.12}$$

from the bulk value in the superfluid region. Here the bulk Fermi momentum is calculated from the local density in the superfluid region via $k_f = \pi\rho_f/2$. In general, the evaluation of ξ_Δ becomes less reliable when the bulk Δ suffers strong fluctuations in the weakly interacting regime with $c < 1$. On the other hand, there are also restrictions on the fitting of $F(x)$ and $C(r)$, as will be explained below. In our analysis, we stay within the reliable regimes for extracting the scaling behavior.

5.4.2 Results for step-function quench

In Figure 5.3, it is evident that while the density profile remains relatively uniform inside the box after a step-function quench, there is a significant change

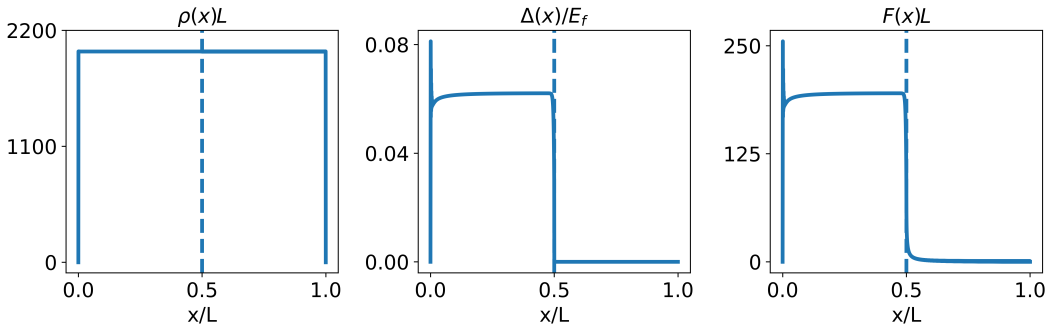

Figure 5.3: Profiles of the density (left), gap function (middle), and pair wavefunction (right) in a step-function quench. The vertical dashed lines indicate where the pairing interaction drops to zero. Here $n_x = 2000$, $N_f = 2000$, and $c = 1$.

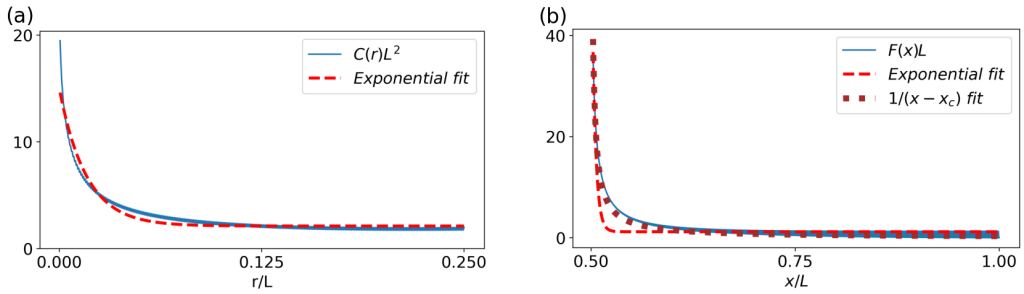

Figure 5.4: (a) The pair correlation function $C(r)$ (solid line) and its exponential fit (dashed line). (b) The pair wavefunction $F(x)$ (solid line) and its exponential fit (dashed line) and power-law fit (dotted line). In both (a) and (b) $n_x = 2000$, $N_f = 2000$ and $c = 1$.

in the order parameter across the critical point. The samples obtained through curve-fitting for the step-function quench are displayed in Figure 5.4, whereas Figure 5.5 exhibits the BCS coherence length ξ_Δ as well as the correlation lengths ξ_F and ξ_C. However, the range for c is constrained for ξ_F and ξ_C since the gap function $\Delta(x)$ experiences strong fluctuations in the superfluid region if $c < 1$. Furthermore, if $c > 3$, the correlation lengths ξ_F and ξ_C may fall below the numerical resolution, leading to observable discrepancies in the fitting results.

Research on proximity effects in SC-NM junctions [73–75] has suggested that the primary length scale governing the penetration of Cooper pairs is the BCS coherence length ξ_Δ. As the pairing interaction becomes stronger, the fermions become more strongly bound, resulting in a smaller BCS coherence length as the

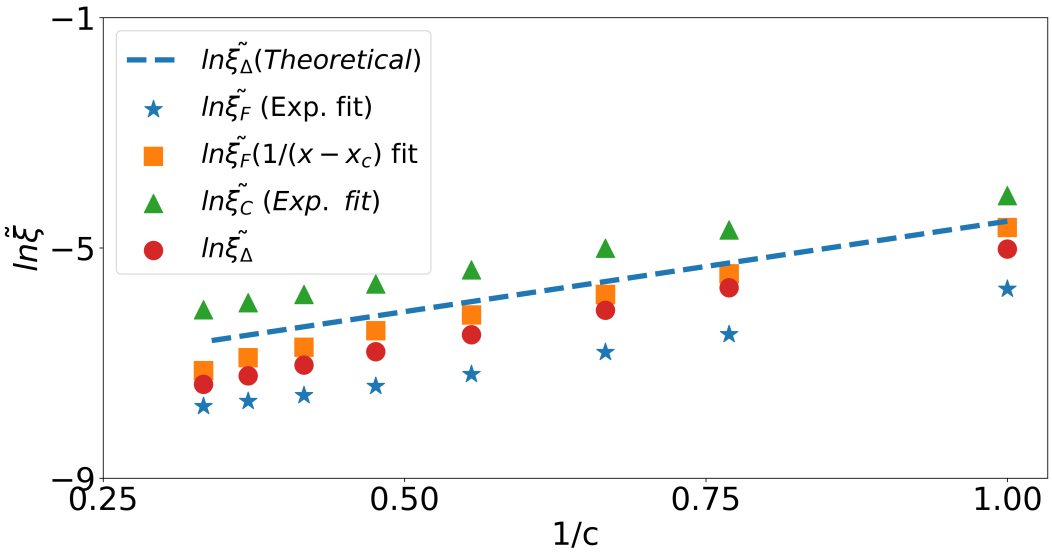

Figure 5.5: Scaling behavior with respect to $1/c$ of $\tilde{\xi}_F = \xi_F/L$ from the exponential fit (stars) and the power-law fit (squares), $\tilde{\xi}_C = \xi_C/L$ from the exponential fit (triangles), and the BCS coherence length $\xi_\Delta = \tilde{\xi}_\Delta L$ (circles). The dashed straight line represents the BCS approximation of the coherence length at zero temperature given by Eq. (5.13).Here $n_x = 2000$ and $N_f = 2000$.

pairs become more tightly bound in real space. It can also be observed that increasing the pairing interaction leads to a higher bulk Δ and a lower BCS coherence length, as per the relationship given by Eq. (5.12). In the weakly interacting limit, the gap function at zero temperature is given by [1, 3] $\Delta = \frac{8}{e^2} E_f \, e^{-1/\mathcal{N}g}$, where $\mathcal{N} = \frac{m}{\pi\hbar^2 k_f}$ is the density of states at the Fermi energy in 1D. Therefore, the BCS coherence length in the weakly interacting limit ($g \to 0$) becomes

$$\xi_\Delta = \frac{e^2}{4k_f} e^{1/\mathcal{N}g}. \tag{5.13}$$

From the results of the step-function quench, it can be inferred that the correlation lengths ξ_F and ξ_C and the BCS coherence length ξ_Δ exhibit the same scaling behavior, as shown in Figure 5.5. Consequently, our findings support the notion that the correlation lengths ξ_F and ξ_C decrease along with the BCS coherence length as the pairing interaction becomes stronger. Additionally, our results verify that ξ_Δ from the superfluid region serves as the only relevant length scale apart from the box size L in a step-function quench. The chemical potential utilized in the step-function quench study is around $\mu \sim 0.9E_f^0$, indicating that the system is still in the BCS regime. Furthermore, the correlation and coherence length follow the BCS coherence length in the weakly interacting limit,

as demonstrated in Figure 5.5. Consequently, we have presented a comprehensive comparison of the various coherence and correlation lengths in the step-function quench.

5.4.3 Results for spatial quench

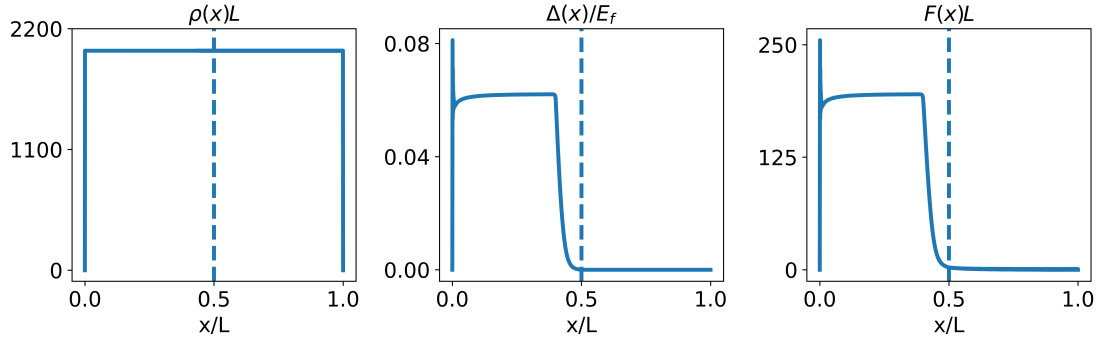

Figure 5.6: Profiles of the density (left), gap function (middle) and pair wavefunction (right) in a spatial quench. The vertical dashed lines indicate where the interaction drops to zero. Here $n_x = 2000$, $N_f = 2000$, $c = 1$, and $d = 0.1$.

For the spatial quench, the pairing interaction drops from the superfluid region to zero in the normal-gas region within a distance d. To better understand the spatial KZM, we first follow Ref. [160] and review the critical exponent of uniform superconductors described by the mean-field Ginzburg-Landau theory in the thermodynamic limit.

The correlation function for a uniform system is derived from the free-energy functional. For BCS superfluid in terms of a field $\phi(x)$ proportional to the order parameter [3], the free-energy functional is given by

$$\mathcal{F} = \int d^d x [\frac{1}{2} a |\nabla \phi|^2 + \frac{1}{2} b \phi^2 + \lambda \phi^4] \tag{5.14}$$

with coefficients a, b and λ. The inverse of the correlation function $C(x, x')$ of a uniform system is given by

$$C^{-1}(x, x') = \frac{\delta^2 \mathcal{F}}{\delta \phi(x) \delta \phi(x')} = (b + 12\lambda\phi^2 - a\nabla^2)\delta(x - x') \tag{5.15}$$

Near the critical point, $\phi \approx 0$, and a Fourier transform gives

$$C(q) = \frac{1}{a} \frac{\xi^2}{1 + (q\xi)^2}, \tag{5.16}$$

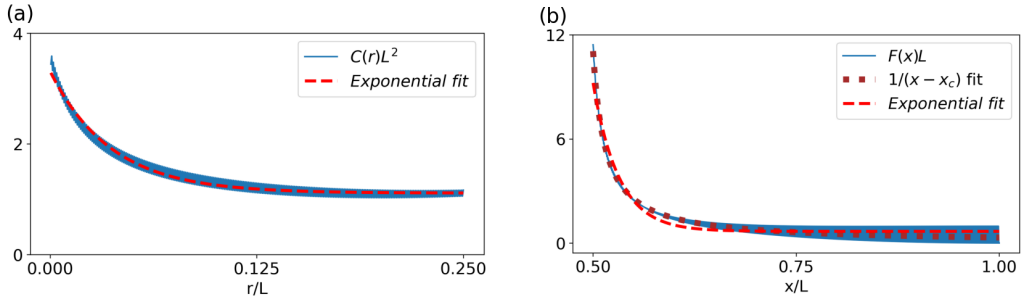

Figure 5.7: (a) $C(r)$ (solid line) and its exponential fit (dashed line). (b) $F(x)$ (solid line) and its exponential fit (dashed line) and power-law fit (dotted line). Here $n_x = 2000$, $N_f = 2000$, $c = 5$, and $d = 0.1$.

where $\xi^2 = a/b$. The coefficient b corresponds to g_{ff} of the BCS superfluid studied here while a is proportional to $\hbar^2/m$ according to Eq. (2.9). Therefore, $\xi^2 \propto \frac{\hbar^2}{m g_{ff}}$ diverges near the critical point as $g_{ff} \to g_{ff}^c = 0$ and gives the exponent $\nu = 1/2$ for the correlation length ξ in a uniform system. Since the BdG equation is based on the mean-field BCS treatment [72], the exponents from our calculations are expected to agree with the prediction from the spatial KZM based on the Ginzburg-Landau theory. The exponent $\nu = 1/2$ of the uniform system leads to $\xi \sim \alpha^{-1/3}$, where $\nu/(1+\nu) = 1/3$, for the spatial KZM. Here $\alpha L = c/d$ represents the slope of the interaction ramp, or the transition rate in real space. The pair wavefunction $F(x)$ and pair correlation function $C(r)$ along with their fitting curves in a selected case of the spatial quench are shown in Fig. 5.7. For $F(x)$, the power-law form Eq.(5.2) again fits better, but the exponential form Eq.(5.1) gives close answers despite more significant deviations. In contrast, the power-law form cannot reasonably fit to $C(r)$ while the exponential form fits reasonably well, as shown in Fig. 5.7. Fig. 5.8 shows the scaling behavior of ξ_F and ξ_C with respect to α, which allows us to extract their exponents as summarized in Table 5.1. Different from the step-function quench, here we have a large window to establish the power-law dependence of the correlation lengths on α for the spatial quench. The exponent from $C(r)$ is close to the prediction $1/3$ from the spatial KZM. In contrast, the exponents from $F(x)$ are twice or larger when compared to the spatial KZM prediction. We have checked the scaling behavior of the correlation lengths independently for the parameters c and d and confirmed the consistency with the scaling with respect to $\alpha = c/(dL)$. For the range of α tested in our study, the chemical potential is around $\mu \sim 0.9E_f^0$, again indicating the system is in the BCS regime with half filling. However, the chemical potential can change for lower filling as α changes.

On the other hand, the bulk value of Δ on the superfluid side is only dependent on the parameter c but insensitive to d as long as a plateau of Δ is

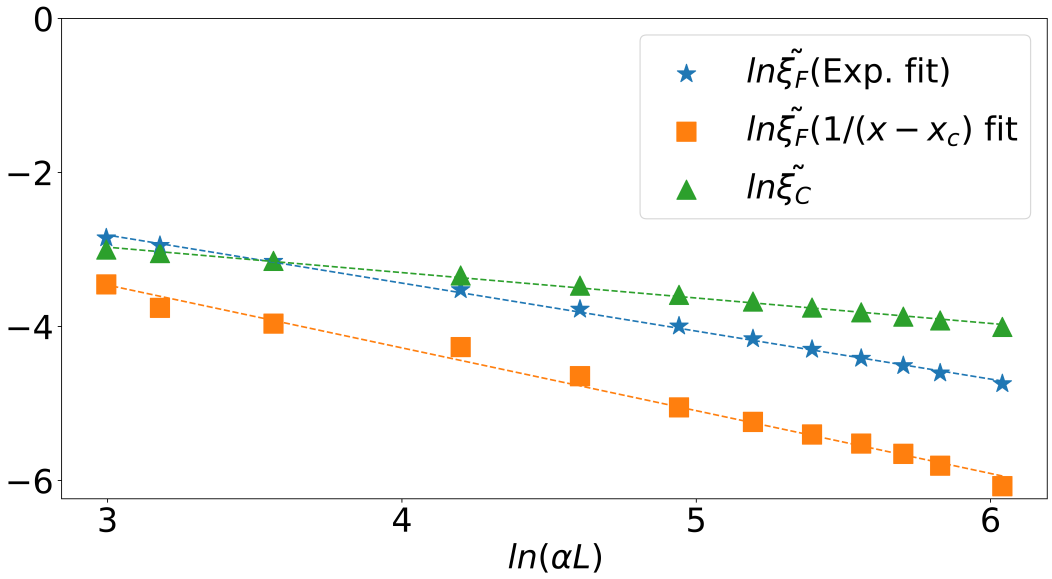

Figure 5.8: Scaling behavior with respect to αL for $\tilde{\xi}_F = \xi_F/L$ from the exponential fit (circles) and the power-law fit (squares) and $\tilde{\xi}_C = \xi_C/L$ (triangles). Here $n_x = 2000$ and $N_f = 2000$.

n_x	N_f	e5	e6	e7
2000	2000	-0.62	-0.82	-0.33
1000	1000	-0.60	-0.79	-0.31

Table 5.1: Exponents of the correlation lengths with respect to $\alpha = c/(dL)$ in the spatial quench. Here $e5$=Exponent of ξ_F from the exponential fit, $e6$=Exponent of ξ_F from the power-law fit, and $e7$=Exponent of ξ_C from the exponential fit. The spatial KZM predicts an exponent of $-1/3$.

observable on the superfluid side. Hence, the BCS coherence length ξ_Δ shown in Eq. (5.12) is only dependent on the parameter c because the density change that affects k_f is virtually non-observable as d changes in our study. As a consequence, it is not meaningful to analyze the scaling of ξ_Δ against $\alpha L = c/d$ in the case of the spatial quench. We thus focus on the correlation lengths from the pair wavefunction and its correlation function when discussing the spatial KZM of BCS superfluid.

As Table 5.1 shows, the exponent from the pair correlation function implies $\nu_C \sim 1/2$, which agrees with the mean-field prediction of a uniform BCS superfluid. However, the exponent from the pair wavefunction gives $\nu_F \sim 2$ by the

exponential fit and $\nu_F \sim 4$ by the power law fit. For the step-function quench, the exponents from F and C are close and follow the trend of the BCS coherence length. In contrast, the spatial quench differentiates the scaling behavior of F and C. Moreover, the spatial KZM scaling only applies to the pair correlation function $C(r)$ but not the pair wavefunction F. This is expected because the value of $\nu = 1/2$ for uniform BCS superfluid is derived from the correlation function, as shown by Eq. (5.16) and its discussion. Therefore, the Fermi gases impose some constraints on the spatial KZM and differentiate the pair wavefunction from its correlation function. Moreover, the additional length scale d invalidates the scaling analysis of the BCS coherence length in the spatial KZM.

5.5 Quenching of fermions with uniform bosonic background

After discussing the step-function and spatial quenches of Fermi gases, we consider the quenches in the presence of a uniform bosonic background, which may come from sympathetic cooling [161] or boson-fermion superfluid mixtures [162]. In a simple setting, we consider fermions with two components and bosons in the same quasi-1D box of length L. There is attraction between fermions with opposite spins but repulsion between bosons and between fermions and bosons. As a first attempt to address the mixture, we only consider the inhomogeneous pairing interaction $g_{ff}(x)$ between the fermions while keeping the other parameters uniform. By using the fermionic parameters as units, the boson-boson and boson-fermion coupling constants can be written in terms of dimensionless quantities as $g_{bb} = \tilde{g}_{bb} E_f^0/k_f^0$ and $g_{bf} = \tilde{g}_{bf} E_f^0/k_f^0$, respectively.

Previous studies [47, 98] have shown that bosons and fermions in a binary mixture can form miscible mixtures when the inter-species interaction is relatively weak or the densities are low. However, phase-separation structures with inhomogeneous densities start to emerge as the inter-species interaction and densities increase. Moreover, the pressure of bosons is mainly from the boson-boson interactions, which competes with the Fermi pressure of the fermions. Since we focus on the impact of the bosonic background on the quenches of fermions, we concentrate on the regime when the mixture is in the miscible phase. Instead of a full analysis of various atomic boson-fermion mixtures, we check a specific case of ^{7}Li - ^{6}Li mixtures with equal population of all species. The conditions $\tilde{g}_{bf} << \tilde{g}_{bb}$ and half-filling are sufficient to maintain a miscible phase for the selected case. However, the formalism presented here is generic and can be applied to atomic boson-fermion mixtures in general.

The total ground-state energy functional of a mixture of bosons and fermions in a quasi-1D box of length L, assuming the fermions form a BCS superfluid, is

given by

$$E_{mix} = E_g + E_b + g_{bf} \int_0^L dx \rho_b(x) \rho_f(x). \tag{5.17}$$

Here, E_g is the BCS ground-state energy shown in Eq. 2.20, and the energy of the bosons is

$$E_b = \int_0^L dx [\frac{\hbar^2}{2m_b} |\partial_x \psi_b|^2 + \frac{1}{2} g_{bb} |\psi_b|^4]. \tag{5.18}$$

In the mean-field description of the ground state, the condensate wavefunction of the bosons is governed by the Gross-Pitaevskii (GP) equation [1, 69]. To find the minimal-energy configuration, we implement the imaginary-time formalism [1, 3] by searching for the stable solution to the imaginary-time evolution equation $-\partial \psi_b / \partial \tau = \delta E_{mix} / \delta \psi_b^*$ in the $\tau \to \infty$ limit, starting from a trial initial configuration. The normalization $\int |\psi_b|^2 dx = N_b$ is imposed at each imaginary-time increment to project out higher-energy states. Here $\tau = it$ is the imaginary time. Explicitly,

$$-\hbar \frac{\partial \psi_b}{\partial \tau} = -\frac{\hbar^2}{2m_b} \partial_x^2 \psi_b + g_{bb} \rho_b \psi_b + g_{bf} \rho_f \psi_b, \tag{5.19}$$

The fermions are described by the BdG equation (2.35) with the replacement of the discretization of $h(x) = -\frac{\hbar^2}{2m} \frac{\partial^2}{\partial x^2} - \mu_f + g_{bf} \rho_b$. The bosonic density is $\rho_b(x) = |\psi_b(x)|^2$ while $\rho_f(x) = 2 \sum_{\tilde{n}}' |v_{\tilde{n}}(x)|^2$ for the fermions as before.

For a uniform and miscible mixture of bosons and fermions, the mean-field treatment shifts the chemical potential of the fermions by $g_{bf} \rho_b$, which only shows up in the diagonal of the BdG equation. Therefore, the gap function is not affected directly by the bosons. This implies that the scaling of the fermionic correlation functions are insensitive to the bosonic background as long as the mixture remains uniform and miscible. However, the presence of step-function or spatial quench of boson-fermion mixtures in a quasi-1D box may introduce complications due to the inhomogeneous pairing interaction and confining potential. We numerically solve the coupled BdG and GP equations for a miscible boson-fermion mixtures in a quasi-1D box to verify if the exponents of the fermionic correlation lengths ξ_F and ξ_C are affected by the bosonic background.

To solve the coupled BdG and GP equations by self-consistent iteration with given numbers of the bosons N_b and fermions N_f, we begin with trial chemical potential μ_f, boson wavefunction ψ_b, and gap function $\Delta(x)$ and first solve the BdG equation following the procedure implemented in the previous sections. The gap function $\Delta(x)$ and fermionic density $\rho_f(x)$ are then obtained from the eigenfunctions $u_{\tilde{n}}(x)$ and $v_{\tilde{n}}(x)$. Next, we evolve the imaginary-time evolution equation (5.19) to get the ground-state bosonic density $\rho_b(x)$. We continue the iterations between the BdG and GP equations until the final convergence of the gap function $\Delta(x)$ and the bosonic density $\int_0^L |\rho_b^{old}(x) - \rho_b^{new}(x)| dx < 10^{-5}$ is reached.

During the iterations, we also adjust the chemical potential μ_f for the BdG equation to meet the fixed number of total fermions. Similar to the case with only fermions, different initial states have been used to confirm the ground state for both species by checking the ground-state energy using Eq. (5.17). Since we focus on the case with a uniform bosonic background, we confine our parameters to $\tilde{g}_{bf} << \tilde{g}_{bb}$, where the convergence to the miscible phase is found in all our trials of the initial states. Similar to the procedures of step-function and spatial quenches discussed above, we calculated the pair wavefunction $F(x)$ and correlation function $C(r)$ to extract the corresponding correlation lengths ξ_F and ξ_C, respectively.

Samples of the profiles of the density, gap function, and pair wavefunction of the step-function and spatial quenches of fermions in a boson-fermion mixture are shown in Fig. 5.9. For the step-function quench, we also evaluate the BCS coherence length ξ_Δ from the bulk values on the superfluid side. From our numerical results, we found that the inclusion of a bosonic background with uniform parameters does not alter the scaling behavior of ξ_F and ξ_C of the fermions. All the exponents from the step-function and spatial quenches of boson-fermion mixtures are within numerical accuracy the same as those without the bosons, which have been shown in Table 5.1. As shown in Fig. 5.9, this is mainly because the density profile of bosons becomes quite flat already at relatively small $\tilde{g}_{bb}$, making the bosonic background basically uniform and does not further complicate the behavior of the fermions.

Nevertheless, the phase-separation structures of boson-fermion mixtures can exhibit various inhomogeneous profiles already for binary mixtures in the presence of uniform interactions [47, 98]. Adding inhomogeneous interactions to the fermions, such as the step-function or spatial quench of the pairing interaction studied here, is expected to lead to richer structures. Extracting the correlation lengths in such highly inhomogeneous setups will be a challenge and await future research.

5.6 Inhomogeneous interactions in cold atoms and quantum gas microscopes

Experimentally, ultracold atoms have been usually subject to uniform interactions due to the small cloud size compared to the magnetic field for tuning Feshbach resonance [1, 99]. There have been several ways for inducing inhomogeneous interactions in cold atoms. One approach is to use optical techniques to control the interactions between atoms. Examples include optical Feshbach resonance [163–165] and optically controlled magnetic Feshbach reso-

nance [166,167]. There have been theoretical studies of inhomogeneous condensates in which investigations on non-linear excitations in quasi-1D Bose-Einstein condensates were carried out in presence of spatially varying atomic scattering length [168–171]. Refs. [167, 172] demonstrate spatial modulation of the interaction in BEC [167] and ^{6}Li fermions [172] by optical controls with high speed and precision. Optical techniques may suffer atom loss and heating, so they are more suitable for changing the interaction with short length or time scale. Another approach is based on magnetic Feshbach resonance and magnetic field gradient [173], which allows for longer observation time. Thus, the inhomogeneous interactions for realizing the step-function and spatial quenches may become feasible with the rapid developments in manipulating ultracold atoms.

Recent progress in quantum gas microscopy allows mapping of site-resolved density- or spin- correlations of the Fermi Hubbard model [174–176]. Ref. [177] demonstrates site-resolved location and spin of each fermion in the attractive Fermi Hubbard system using a bilayer quantum-gas microscope and reveals the formation and spatial ordering of fermion pairs. In addition, radio-frequency (rf) spectroscopy has been used to measure the excitation energy that reveals the pairing gap in atomic Fermi gases [178–181]. Future developments may allow spatial resolution of the rf spectroscopy for cold atoms. Those spatially resolved measurements of the pairing correlation of atomic Fermi gases are promising for observing the scaling behavior of the step-function and spatial quenches analyzed here.

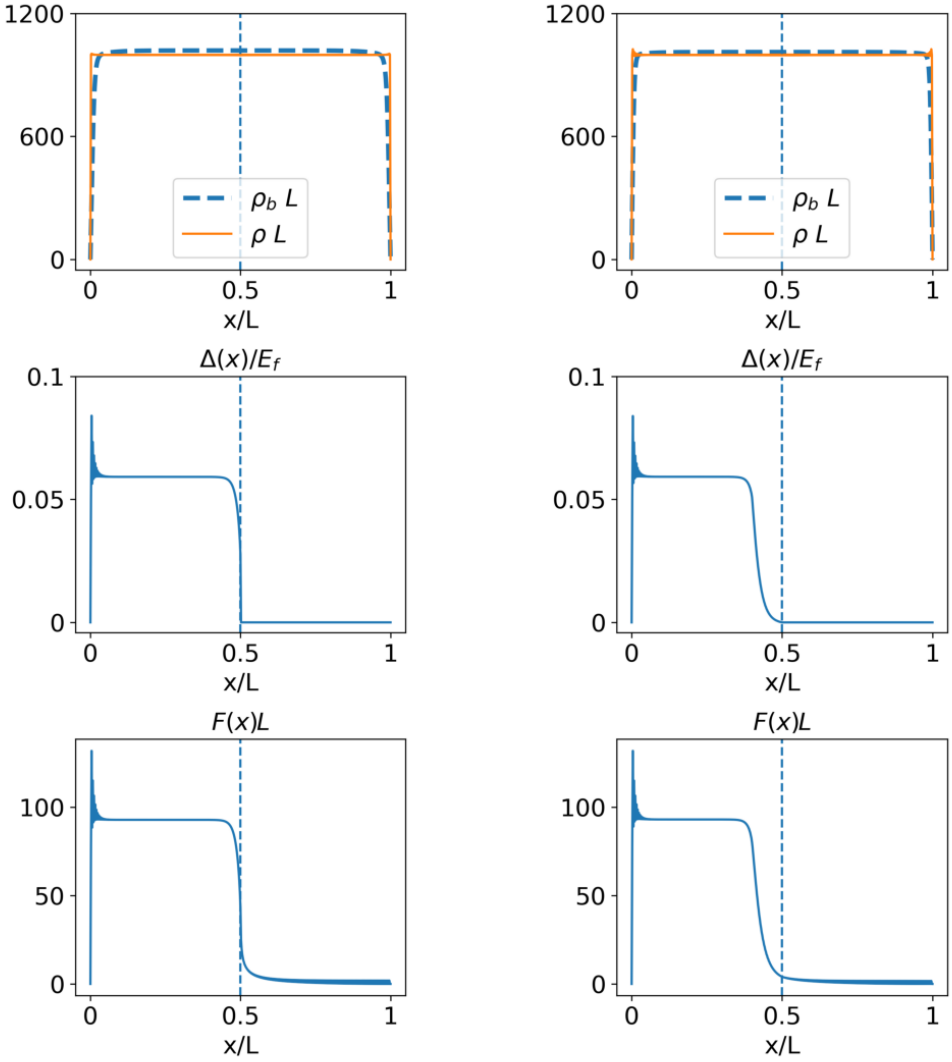

Figure 5.9: Profiles of the density (top row), gap function (middle row), and pair wavefunction (bottom row) of the step-function quench (left column) and spatial quench (right column) of ^{6}Li in a ^{6}Li-^{7}Li mixture. For the step-function quench, $n_x = 1000$, $N = N_b = 1000$, and $c = 1$. For the spatial quench, $n_x = 1000$, $N = N_b = 1000$, $c = 1$, and $d = 0.1$. For both cases, $\tilde{g}_{bb} = 0.1$ and $\tilde{g}_{bf} = 0.05$.

CHAPTER 6
CONCLUSION

In conclusion, this dissertation has investigated the properties of various ultracold atomic mixtures in box potentials. We have shown that these systems are versatile platforms for exploring a wide range of phenomena, including mixtures of same spin statistics [85], mixtures of different spin statistics [98], and atomic Fermi superfluid [104]. By employing both analytical and numerical techniques, we have characterized the ground-state properties of these systems, such as phase-diagrams, density profiles, and correlation functions. We have also explored the effects of various parameters, such as the interaction strength and mass asymmetry, and the role of spin statistics on the properties of the mixtures.

In the study of repulsive boson-boson and fermion-fermion mixtures in 1D box potentials, we have shown the structural difference in the ground-state structures induced by the mass-imbalance of the species. The difference is the influence of the box potential arising from the competition of interaction energy and kinetic energy due to the density distortion at the hard walls and phase-separation interface. Since mass is inversely proportional to the kinetic energy, our results will guide experiments to choose right species to observe the phase-separation structures. Additionally, we presented the rich phase-diagrams, density profiles and interface structures arising from the mass-asymmetry for repulsive boson-fermion mixtures. Our main contribution in this study is the analyses of the scaling behavior of the healing lengths at the interface based on the energy-competition argument. Importantly, the inclusion of Fermi energy E_f as the effective interaction in the healing length analysis is crucial to reproduce the correct scaling behavior.

Our research has demonstrated that atomic Fermi gases with adjustable interactions in real space are a highly effective tool for simulating the analogs of the proximity effect and spatial KZM. By conducting numerical calculations utilizing a step-function or spatial quench of the pairing interaction, we characterize the extent to which the pair wavefunction and pair correlation penetrate the non-interacting region. In the case of the step-function quench, the correlation lengths conformed to the BCS coherence length and cannot differentiate the pair wavefunction from its correlation function. Conversely, in the spatial quench, the correlation lengths of the pair wavefunction and pair correlation function generated different exponents, with only the exponent derived from the pair correlation function aligning with the spatial KZ scaling of mean-field Fermi superfluid. Our contribution in this study is the extraction of different length scales from the pair wavefunction and correlation function. Our results are different from the study of spatial KZM for transverse-field quantum Ising model where correlation lengths from order parameter (spontaneous magnetization)

and spin-spin correlation function leads to same scaling behavior. Therefore, KZ scaling is more selective in our case of quasi-1D Fermi superfluid.

Overall, this dissertation has contributed to the understanding of ultracold atomic mixtures in box potentials and provides a foundation for merging of ultracold mixtures and box potential experiments in future. Given the versatility of cold atoms experiments and the insights gained from this work, it can potentially inform the design and realization of new experiments, such as analogs of Ferromagnet-Superconductor heterostuctures, which has the ability to host Majorana bound states [121], utilizing atomic mixtures to study the proximity effect. This can be done by choosing the right species that behaves as a superconductor and as a ferromagnet, preparing the atomic mixture using cooling techniques, confining in a box trap and finally, tuning the interaction between the species. Our investigation on boson-fermion mixtures was done for uniform interactions in space. With the experimental demonstration of spatially dependent interactions for ultracold atoms, such inhomogeneous interactions can be applied to boson-fermion mixtures to observe the resulting structures of the mixture. The aim of such experiments would be to gain insights into the complex interplay between different species and to explore the possibility of new structures.

APPENDIX A
IMAGINARY-TIME FORMALISM

To find the minimal-energy configuration for the solutions of GPE, we can implement the imaginary-time formalism [3] by searching for the solution to the imaginary-time evolution equations in the $\tau \to \infty$ limit with the normalization $\int |\psi|^2 dx = 1$ imposed at each imaginary-time increment. Here $\tau = it$ is the imaginary time. Schrödinger equation in imaginary time is given as

$$-\hbar \frac{\partial \psi}{\partial \tau} = H\psi \tag{A.1}$$

The wavefunction can be decomposed into the sum of eigenfunctions ϕ_i.

$$\psi = \sum_i c_i \phi_i \tag{A.2}$$

where, c_i are constants. For each eigenfunctions, the solution to Schrödinger equation is given by

$$\phi_i(\tau) = e^{-E_i \tau/\hbar} \phi_i(0) \tag{A.3}$$

The solution ψ in terms of eigenfunctions ϕ_i is given as

$$\psi(\tau) = \sum_i c_i e^{-E_i \tau/\hbar} \phi_i(0) \tag{A.4}$$

Upon the successive iterations and for $\tau \to \infty$ limit , the excited states contribution to the solution decays and the solution tends to the ground state.

APPENDIX B

SPLIT-STEP CRANK-NICOLSON SCHEME

To solve the Gross-Pitaevskii equation which consists of a non-linear term, we use split-step Crank-Nicolson scheme [93, 94].

$$-\frac{\partial\psi}{\partial\tau} = -\frac{\partial^2\psi}{\partial x^2} + V\psi + gN_b|\psi|^2\psi = H\psi \tag{B.1}$$

where, Hamiltonian H is given as,

$$H = -\frac{\partial^2}{\partial x^2} + V + gN_b|\psi|^2 \tag{B.2}$$

Hamiltonian includes kinetic energy term $-\frac{\partial^2}{\partial x^2}$, external potential $V(x)$ and interaction term $gN_b|\psi|^2$ which is non-linear. In this scheme, we split Hamiltonian into two parts, non-linear and spatial derivative.

$H = H_1 + H_2$ with $H_1 = V(x) + gN_b|\psi|^2$ and $H_2 = -\frac{\partial^2}{\partial x^2}$. Splitting Hamiltonian we also split (B.1) into two equations.

$$\frac{\partial\psi}{\partial\tau} = -H_1\psi \tag{B.3}$$

$$\frac{\partial\psi}{\partial\tau} = -H_2\psi \tag{B.4}$$

Here, space is discretized in n steps of Δx and time is discretized in t steps of $\Delta\tau$. Basically we write

$$\psi(x_i, \tau_j) = \psi_{i,j}$$

$$x_i = i\Delta x; \qquad i = 0, 1, 2, ..., n.$$

$$\tau_j = j\Delta\tau; \qquad j = 0, 1, 2, ...t.$$

First of all, we solve (A3) with initial $\psi(x, \tau = 0)$ to get intermediate solution at $\tau = \Delta\tau/2$. If $\psi_{i,j}$ is the initial wavefunction, then intermediate solution is given as,

$$\psi_{i,j+1/2} = \psi_{i,j}\ \ e^{-H_1\Delta\tau/2} \tag{B.5}$$

After finding intermediate solution, we use this solution to solve (A4) by using semi-implicit Crank-Nicolson method.

$$\frac{\partial\psi}{\partial\tau} = \frac{\partial^2\psi}{\partial x^2}$$

or,

$$\frac{\psi_{i,j+1} - \psi_{i,j+1/2}}{\Delta\tau} = \frac{\partial^2}{\partial x^2}\left(\frac{\psi_{i,j+1} + \psi_{i,j+1/2}}{2}\right)$$

$$\begin{aligned}\frac{\psi_{i,j+1} - \psi_{i,j+1/2}}{\Delta\tau} =& \frac{1}{2(\Delta x)^2}\Big(\psi_{i+1,j+1} - 2\psi_{i,j+1} \\ &+ \psi_{i-1,j+1} + \psi_{i+1,j+1/2} \\ &- 2\psi_{i,j+1/2} + \psi_{i-1,j+1/2}\Big)\end{aligned} \tag{B.6}$$

Simplifying the equation with $\alpha = \frac{\Delta\tau}{2(\Delta x)^2}$ we get tri-diagonal set of equations in $\psi_{i+1,j+1}$, $\psi_{i,j+1}$ and $\psi_{i-1,j+1}$ at time τ_{j+1} which is solved using proper boundary conditions.

$$\begin{aligned}&\alpha\psi_{i+1,j+1} - (2\alpha+1)\psi_{i,j+1} + \alpha\psi_{i-1,j+1} \\ &= -\alpha\psi_{i+1,j+1/2} + (2\alpha-1)\psi_{i,j+1/2} - \alpha\psi_{i-1,j+1/2}\end{aligned} \tag{B.7}$$

ψ's on left hand side are unknowns and those on right hand side are known.

$$A_1 1\psi_{unknown} = A_2\psi_{known} \tag{B.8}$$

where, A_1 and A_2 are the band-diagonal matrices given by

$$A_1 = \begin{pmatrix} -(2\alpha+1) & \alpha & \dots & \dots & \dots & \dots \\ \alpha & -(2\alpha+1) & \alpha & \dots & \dots & \dots \\ \dots & \alpha & -(2\alpha+1) & \alpha & \dots & \dots \\ \dots & \dots & \dots & \dots & \dots & \dots \\ \dots & \dots & \dots & \alpha & -(2\alpha+1) & \alpha \\ \dots & \dots & \dots & \dots & \alpha & -(2\alpha+1) \end{pmatrix} \tag{B.9}$$

$$A_2 = \begin{pmatrix} (2\alpha-1) & -\alpha & \dots & \dots & \dots & \dots \\ -\alpha & (2\alpha-1) & -\alpha & \dots & \dots & \dots \\ \dots & -\alpha & (2\alpha-1) & -\alpha & \dots & \dots \\ \dots & \dots & \dots & \dots & \dots & \dots \\ \dots & \dots & \dots & -\alpha & (2\alpha-1) & -\alpha \\ \dots & \dots & \dots & \dots & -\alpha & (2\alpha-1) \end{pmatrix} \tag{B.10}$$

We use numpy.linalg.solve python package to solve the equation B.8.

APPENDIX C
NUMERICAL PROCEDURES TO SOLVE *BdG* EQUATION

To solve the BdG equation,

- We begin with chemical potential μ and an initial trial for $\Delta(x)$.
- Find the eigenvalues and eigenfunctions from the BdG equation. We use numpy.linalg python package to obtain the eigenvalues and eigenfunctions.
- Assemble $\Delta(x)$ from the eigenfunctions using Eq. (2.37).
- The new gap function is used in the BdG equation to find the new eigenvalues and eigenfunctions.
- Continue the iteration until the consistency condition $\int |\Delta^{old} - \Delta^{new}| dx < 10^{-5}$ is met.
- Adjust μ and repeat the above steps until we meet the condition $N_f = \int \rho_f(x) dx$ using Eq. (2.36).

BIBLIOGRAPHY

[1] C. J. Pethick and H. Smith, *Bose–Einstein Condensation in Dilute Gases*. Cambridge University Press, 2 ed., 2008.

[2] J. Sakurai and J. Napolitano, *Modern Quantum Mechanics*. Cambridge University Press, 2017.

[3] A. Fetter and J. Walecka, *Quantum Theory of Many-Particle Systems*. Dover Books on Physics, Dover Publications, 2012.

[4] M. Ueda, *Fundamentals and New Frontiers of Bose-Einstein Condensation*. WORLD SCIENTIFIC, 2010.

[5] M. H. Anderson, J. R. Ensher, M. R. Matthews, C. E. Wieman, and E. A. Cornell, "Observation of bose-einstein condensation in a dilute atomic vapor," *Science*, vol. 269, no. 5221, pp. 198–201, 1995.

[6] C. C. Bradley, C. A. Sackett, J. J. Tollett, and R. G. Hulet, "Evidence of bose-einstein condensation in an atomic gas with attractive interactions," *Phys. Rev. Lett.*, vol. 75, pp. 1687–1690, Aug 1995.

[7] K. B. Davis, M. O. Mewes, M. R. Andrews, N. J. van Druten, D. S. Durfee, D. M. Kurn, and W. Ketterle, "Bose-einstein condensation in a gas of sodium atoms," *Phys. Rev. Lett.*, vol. 75, pp. 3969–3973, Nov 1995.

[8] D. S. Hall, M. R. Matthews, J. R. Ensher, C. E. Wieman, and E. A. Cornell, "Dynamics of component separation in a binary mixture of bose-einstein condensates," *Phys. Rev. Lett.*, vol. 81, pp. 1539–1542, Aug 1998.

[9] E. G. D. Cohen, "Quantum statistics and liquid helium-3—helium-4 mixtures," *Science*, vol. 197, no. 4298, pp. 11–16, 1977.

[10] M. L. Wall, K. R. A. Hazzard, and A. M. Rey, "Quantum magnetism with ultracold molecules," in *From Atomic to Mesoscale*, pp. 3–37, WORLD SCIENTIFIC, jun 2015.

[11] C. J. Myatt, E. A. Burt, R. W. Ghrist, E. A. Cornell, and C. E. Wieman, "Production of two overlapping bose-einstein condensates by sympathetic cooling," *Phys. Rev. Lett.*, vol. 78, pp. 586–589, Jan 1997.

[12] M. W. Zwierlein, C. A. Stan, C. H. Schunck, S. M. F. Raupach, S. Gupta, Z. Hadzibabic, and W. Ketterle, "Observation of bose-einstein condensation of molecules," *Phys. Rev. Lett.*, vol. 91, p. 250401, Dec 2003.

[13] M. Greiner, C. A. Regal, and D. S. Jin, "Emergence of a molecular bose-einstein condensate from a fermi gas," *Nature*, vol. 426, no. 6966, pp. 537–540, 2003.

[14] A. G. Truscott, K. E. Strecker, W. I. McAlexander, G. B. Partridge, and R. G. Hulet, "Observation of fermi pressure in a gas of trapped atoms," *Science*, vol. 291, no. 5513, pp. 2570–2572, 2001.

[15] F. Schreck, L. Khaykovich, K. L. Corwin, G. Ferrari, T. Bourdel, J. Cubizolles, and C. Salomon, "Quasipure bose-einstein condensate immersed in a fermi sea," *Phys. Rev. Lett.*, vol. 87, p. 080403, Aug 2001.

[16] Z. Hadzibabic, C. A. Stan, K. Dieckmann, S. Gupta, M. W. Zwierlein, A. Görlitz, and W. Ketterle, "Two-species mixture of quantum degenerate bose and fermi gases," *Phys. Rev. Lett.*, vol. 88, p. 160401, Apr 2002.

[17] G. Roati, F. Riboli, G. Modugno, and M. Inguscio, "Fermi-bose quantum degenerate ^{40}K–^{87}Rb mixture with attractive interaction," *Phys. Rev. Lett.*, vol. 89, p. 150403, Sep 2002.

[18] C. Ospelkaus, S. Ospelkaus, K. Sengstock, and K. Bongs, "Interaction-driven dynamics of ^{40}K –^{87} *Rb* fermion-boson gas mixtures in the large-particle-number limit," *Phys. Rev. Lett.*, vol. 96, p. 020401, Jan 2006.

[19] G. Modugno, G. Roati, F. Riboli, F. Ferlaino, R. J. Brecha, and M. Inguscio, "Collapse of a degenerate fermi gas," *Science*, vol. 297, no. 5590, pp. 2240–2243, 2002.

[20] B. Deh, C. Marzok, C. Zimmermann, and P. W. Courteille, "Feshbach resonances in mixtures of ultracold ^{6}Li and ^{87}Rb gases," *Phys. Rev. A*, vol. 77, p. 010701, Jan 2008.

[21] M. K. Tey, S. Stellmer, R. Grimm, and F. Schreck, "Double-degenerate bose-fermi mixture of strontium," *Phys. Rev. A*, vol. 82, p. 011608, Jul 2010.

[22] X.-C. Yao, H.-Z. Chen, Y.-P. Wu, X.-P. Liu, X.-Q. Wang, X. Jiang, Y. Deng, Y.-A. Chen, and J.-W. Pan, "Observation of coupled vortex lattices in a mass-imbalance bose and fermi superfluid mixture," *Phys. Rev. Lett.*, vol. 117, p. 145301, Sep 2016.

[23] B. J. DeSalvo, K. Patel, J. Johansen, and C. Chin, "Observation of a degenerate fermi gas trapped by a bose-einstein condensate," *Phys. Rev. Lett.*, vol. 119, p. 233401, Dec 2017.

[24] M. A. García-March, B. Juliá-Díaz, G. E. Astrakharchik, J. Boronat, and A. Polls, "Distinguishability, degeneracy, and correlations in three harmonically trapped bosons in one dimension," *Phys. Rev. A*, vol. 90, p. 063605, 2014.

[25] A. G. Volosniev, D. V. Fedorov, A. S. Jensen, M. Valiente, and N. T. Zinner, "Strongly interacting confined quantum systems in one dimension," *Nat. Comm.*, vol. 5, p. 5300, 2014.

[26] F. F. Bellotti, A. S. Dehkharghani, and N. T. Zinner, "Comparing numerical and analytical approaches to strongly interacting two-component mixtures in one dimensional traps," *Eur. Phys. J. D*, vol. 71, p. 37, Feb 2017.

[27] A. Dehkharghani, A. Volosniev, J. Lindgren, J. Rotureau, C. Forssen, D. Fedorov, A. Jensen, and N. Zinner, "Quantum magnetism in strongly inter-

acting one-dimensional spinor Bose systems," *Sci. Rep.*, vol. 5, p. 10675, June 2015.

[28] Y. Hao, Y. Zhang, X.-W. Guan, and S. Chen, "Ground-state properties of interacting two-component bose gases in a hard-wall trap," *Phys. Rev. A*, vol. 79, p. 033607, Mar 2009.

[29] Y. Hao, Y. Zhang, X. W. Guan, and S. Chen, "Ground-state properties of interacting two-component bose gases in a hard-wall trap," *Phys. Rev. A*, vol. 79, p. 033607, 2009.

[30] M. Iskin and C. A. R. Sá de Melo, "Mixtures of ultracold fermions with unequal masses," *Phys. Rev. A*, vol. 76, p. 013601, Jul 2007.

[31] M. Olshanii and S. G. Jackson, "An exactly solvable quantum four-body problem associated with the symmetries of an octacube," *New J. Phys.*, vol. 17, p. 105005, 2015.

[32] X. Cui and T.-L. Ho, "Phase separation in mixtures of repulsive fermi gases driven by mass difference," *Phys. Rev. Lett.*, vol. 110, p. 165302, Apr 2013.

[33] Y. Kang, Z. Sun, Y. Kang, Y. Li, and S. Tan, "Spontaneous separation in trapped fermi gas with p-wave interactions: Due to the mass-imbalance," *J. Low Temp. Phys.*, vol. 190, pp. 225–235, Mar 2018.

[34] N. Takemori and A. Koga, "Low-temperature properties of the fermionic mixtures with mass imbalance in optical lattice," *J. Phys. Soc. Jpn.*, vol. 81, p. 063002, 2012.

[35] C. W. von Keyserlingk and G. J. Conduit, "Itinerant ferromagnetism in an interacting fermi gas with mass imbalance," *Phys. Rev. A*, vol. 83, p. 053625, 2011.

[36] J. Han and M. Tsubota, "Phase separation of quantized vortices in two-component miscible Bose - Einstein condensates in a two-dimensional box potential," 2019. arXiv: 1901.01020.

[37] D. Pecak, M. Gajda, and T. Sowinski, "Two-flavour mixture of a few fermions of different mass in a one-dimensional harmonic trap," *New J. Phys.*, vol. 18, no. 1, p. 013030, 2016.

[38] X. Cui and T. L. Ho, "Phase separation in mixtures of repulsive fermi gases driven by mass difference," *Phys. Rev. Lett.*, vol. 110, p. 165302, 2013.

[39] D. Pecak, M. Gajda, and T. Sowinski, "Two-flavour mixture of a few fermions of different mass in a one-dimensional harmonic trap," *New J. Phys.*, vol. 18, no. 1, p. 13030, 2016.

[40] F. F. Bellotti, A. S. Dehkharghani, and N. T. Zinner, "Comparing numerical and analytical approaches to strongly interacting two-component mixtures in one dimensional traps," *Eur. Phys. J. D*, vol. 71, no. 2, pp. 1–10, 2017.

[41] M.-I. Trappe, P. Grochowski, M. Brewczyk, and K. Rzazewski, "Ground-state densities of repulsive two-component fermi gases," *Phys. Rev. A*, vol. 93, p. 023612, Feb 2016.

[42] K. Mølmer, "Bose condensates and fermi gases at zero temperature," *Phys. Rev. Lett.*, vol. 80, pp. 1804–1807, Mar 1998.

[43] N. Nygaard and K. Mølmer, "Component separation in harmonically trapped boson-fermion mixtures," *Phys. Rev. A*, vol. 59, pp. 2974–2981, Apr 1999.

[44] D. Rakshit, T. Karpiuk, P. Zin, M. Brewczyk, M. Lewenstein, and M. Gajda, "Self-bound bose–fermi liquids in lower dimensions," *New J. Phys.*, vol. 21, no. 7, p. 073027, 2019.

[45] T. Karpiuk, M. Gajda, *et al.*, "Bistability of bose–fermi mixtures," *New J. Phys.*, vol. 22, no. 10, p. 103025, 2020.

[46] M. W. Zwierlein, A. Schirotzek, C. H. Schunck, and W. Ketterle, "Fermionic superfluidity with imbalanced spin populations," *Science*, vol. 311, no. 5760, pp. 492–496, 2006.

[47] T. Kim and C.-C. Chien, "Thermodynamics and structural transition of binary atomic bose-fermi mixtures in box or harmonic potentials: A path-integral study," *Phys. Rev. A*, vol. 97, p. 033628, Mar 2018.

[48] M. Cetina, M. Jag, R. S. Lous, I. Fritsche, J. T. Walraven, R. Grimm, J. Levinsen, M. M. Parish, R. Schmidt, M. Knap, *et al.*, "Ultrafast many-body interferometry of impurities coupled to a fermi sea," *Science*, vol. 354, pp. 96–99, 2016.

[49] C. Ravensbergen, V. Corre, E. Soave, M. Kreyer, E. Kirilov, and R. Grimm, "Production of a degenerate fermi-fermi mixture of dysprosium and potassium atoms," *Phys. Rev. A*, vol. 98, p. 063624, Dec 2018.

[50] R. S. Lous, I. Fritsche, M. Jag, F. Lehmann, E. Kirilov, B. Huang, and R. Grimm, "Probing the interface of a phase-separated state in a repulsive bose-fermi mixture," *Phys. Rev. Lett.*, vol. 120, p. 243403, Jun 2018.

[51] F. Serwane, G. Zürn, T. Lompe, T. Ottenstein, A. Wenz, and S. Jochim, "Deterministic preparation of a tunable few-fermion system," *Science*, vol. 332, pp. 336–8, 2011.

[52] T. Sowiński and M. A. Garcia-March, "One-dimensional mixtures of several ultracold atoms: a review," *Rep. Prog. Phys.*, vol. 82, p. 104401, 2019.

[53] T. Sowinski and M. A. Garcia-March, "One-dimensional mixtures of several ultracold atoms: a review," 2019. arXiv:1903.12189.

[54] M.-I. Trappe, P. Grochowski, M. Brewczyk, and K. Rzazewski, "Ground-state densities of repulsive two-component fermi gases," *Physical Review A*, vol. 93, no. 2, p. 023612, 2016.

[55] G. Valtolina, F. Scazza, A. Amico, A. Burchianti, A. Recati, T. Enss, M. Inguscio, M. Zaccanti, and G. Roati, "Exploring the ferromagnetic behaviour of a repulsive fermi gas through spin dynamics," *Nature Physics*, vol. 13, no. 7, p. 704, 2017.

[56] M. Tinkham, *Introduction to superconductivity*. New York: McGraw-Hill, 2 ed., 1996.

[57] M. Houbiers and H. T. C. Stoof, "Cooper-pair formation in trapped atomic fermi gases," *Phys. Rev. A*, vol. 59, pp. 1556–1561, Feb 1999.

[58] G. M. Bruun and H. Heiselberg, "Cooper pairing and single-particle properties of trapped fermi gases," *Phys. Rev. A*, vol. 65, p. 053407, Apr 2002.

[59] P. F. Bedaque, H. Caldas, and G. Rupak, "Phase separation in asymmetrical fermion superfluids," *Phys. Rev. Lett.*, vol. 91, p. 247002, Dec 2003.

[60] M. W. Zwierlein, A. Schirotzek, C. H. Schunck, and W. Ketterle, "Fermionic superfluidity with imbalanced spin populations," *Science*, vol. 311, no. 5760, pp. 492–496, 2006.

[61] P. Lecheminant, E. Boulat, and P. Azaria, "Confinement and superfluidity in one-dimensional degenerate fermionic cold atoms," *Phys. Rev. Lett.*, vol. 95, p. 240402, Dec 2005.

[62] S. Giorgini, L. P. Pitaevskii, and S. Stringari, "Theory of ultracold atomic fermi gases," *Rev. Mod. Phys.*, vol. 80, pp. 1215–1274, Oct 2008.

[63] J. J. P. van Es, P. Wicke, A. H. van Amerongen, C. Rétif, S. Whitlock, and N. J. van Druten, "Box traps on an atom chip for one-dimensional quantum gases," *J. Phys. B: At. mol. Opt. Phys.*, vol. 43, p. 155002, jul 2010.

[64] M. Tajik, B. Rauer, T. Schweigler, F. Cataldini, J. ao Sabino, F. S. Møller, S.-C. Ji, I. E. Mazets, and J. Schmiedmayer, "Designing arbitrary one-dimensional potentials on an atom chip," *Opt. Express*, vol. 27, pp. 33474–33487, Nov 2019.

[65] L. Chomaz, L. Corman, T. Bienaime, R. Desbuquois, C. Weitenberg, S. Nascimbene, J. Beugnon, and J. Dalibard, "Emergence of coherence via transverse condensation in a uniform quasi-two-dimensional bose gas," *Nat. Comm.*, vol. 6, no. 1, pp. 6162–6162, 2015.

[66] A. L. Gaunt, T. F. Schmidutz, I. Gotlibovych, R. P. Smith, and Z. Hadzibabic, "Bose-einstein condensation of atoms in a uniform potential," *Phys. Rev. Lett.*, vol. 110, p. 200406, May 2013.

[67] K. Hueck, N. Luick, L. Sobirey, J. Siegl, T. Lompe, and H. Moritz, "Two-dimensional homogeneous fermi gases," *Phys. Rev. Lett.*, vol. 120, p. 060402, Feb 2018.

[68] B. Mukherjee, Z. Yan, P. B. Patel, Z. Hadzibabic, T. Yefsah, J. Struck, and M. W. Zwierlein, "Homogeneous atomic fermi gases," *Phys. Rev. Lett.*, vol. 118, p. 123401, Mar 2017.

[69] L. Pitaevskii and S. Stringari, *Bose-Einstein Condensation*. International Series of Monographs on Physics, Clarendon Press, 2003.

[70] A. Minguzzi, S. Succi, F. Toschi, M. P. Tosi, and P. Vignolo, "Numerical methods for atomic quantum gases with applications to bose-einstein condensates and to ultracold fermions," *Phys. Rep. 395*, p. 223, 2004.

[71] N. Bogoliubov, "On the theory of superfluidity," *J. Phys*, vol. 11, no. 1, p. 23, 1947.

[72] J.-X. Zhu, *Bogoliubov-de Gennes Method and Its Applications*. Lecture Notes in Physics, 924, Cham: Springer International Publishing, 1st ed. 2016. ed., 2016.

[73] G. Deutscher and P. de Gennes, "Proximity effects," *pp 1005-34 of Superconductivity. Vols. 1 and 2. Parks, R. D. (ed.). New York, Marcel Dekker, Inc., 1969*, 1969.

[74] D. S. Falk, "Superconductors with plane boundaries," *Phys. Rev.*, vol. 132, pp. 1576–1590, Nov 1963.

[75] W. Silvert, "Spatial dependence of pair correlation functions in nonhomogeneous superconductors," *Rev. Mod. Phys.*, vol. 36, pp. 251–253, Jan 1964.

[76] W. H. Zurek and U. Dorner, "Phase transition in space: how far does a symmetry bend before it breaks?," *Philosophical transactions of the Royal Society of London. Series A: Mathematical, physical, and engineering sciences*, vol. 366, no. 1877, pp. 2953–2972, 2008.

[77] J. Dziarmaga and M. M. Rams, "Dynamics of an inhomogeneous quantum phase transition," *New journal of physics*, vol. 12, no. 5, pp. 055007–, 2010.

[78] B. Damski and W. H. Zurek, "Quantum phase transition in space in a ferromagnetic spin-1 bose–einstein condensate," *New Journal of Physics*, vol. 11, p. 063014, jun 2009.

[79] R. Bause, A. Schindewolf, R. Tao, M. Duda, X.-Y. Chen, G. Quéméner, T. Karman, A. Christianen, I. Bloch, and X.-Y. Luo, "Collisions of ultracold molecules in bright and dark optical dipole traps," *Phys. Rev. Research*, vol. 3, p. 033013, Jul 2021.

[80] M. Olshanii, "Atomic scattering in the presence of an external confinement and a gas of impenetrable bosons," *Phys. Rev. Lett.*, vol. 81, pp. 938–941, Aug 1998.

[81] G. P. Parravicini and G. Grosso, *Solid state physics*. Academic Press, 2013.

[82] A. J. Leggett, *Quantum Liquids: Bose Condensation and Cooper Pairing in Condensed-Matter Systems*. Oxford: Oxford university press, 2008.

[83] S. Sachdev, *Quantum Phase Transitions*. Cambridge University Press, 2 ed., 2011.

[84] P. Chaikin and T. Lubensky, *Principles of Condensed Matter Physics*. Cambridge University Press, 1995.

[85] B. Parajuli, D. Pecak, and C.-C. Chien, "Mass-imbalance-induced structures of binary atomic mixtures in box potentials," *Phys. Rev. A*, vol. 100, p. 063623, Dec 2019.

[86] D. S. Hall, M. R. Matthews, J. R. Ensher, C. E. Wieman, and E. A. Cornell, "Dynamics of component separation in a binary mixture of bose-einstein condensates," *Phys. Rev. Lett.*, vol. 81, pp. 1539–1542, Aug 1998.

[87] E. Timmermans, "Phase separation of bose-einstein condensates," *Phys. Rev. Lett.*, vol. 81, pp. 5718–5721, Dec 1998.

[88] P. Ao and S. T. Chui, "Binary bose-einstein condensate mixtures in weakly and strongly segregated phases," *Phys. Rev. A*, vol. 58, pp. 4836–4840, Dec 1998.

[89] E. B. Kolomeisky, T. J. Newman, J. P. Straley, and X. Qi, "Low-dimensional bose liquids: Beyond the gross-pitaevskii approximation," *Phys. Rev. Lett.*, vol. 85, p. 1146, 2000.

[90] M. A. Garcia-March and T. Busch, "Quantum gas mixtures in different correlation regimes," *Phys. Rev. A*, vol. 87, p. 063633, 2013.

[91] B. Tanatar and K. Erkan, "Strongly interacting one-dimensional bose-einstein condensates in harmonic traps," *Phys. Rev. A*, vol. 62, p. 053601, 2000.

[92] M. D. Girardeau and E. M. Wright, "Comment on 'Strongly interacting one-dimensional Bose-Einstein condensates in harmonic traps'," 2000. arxiv/cond-mat/0010457.

[93] P. Muruganandam and S. Adhikari, "Fortran programs for the time-dependent gross–pitaevskii equation in a fully anisotropic trap," *Comput. Phys. Commun.*, vol. 180, no. 10, pp. 1888 – 1912, 2009.

[94] T. R. Taha and M. I. Ablowitz, "Analytical and numerical aspects of certain nonlinear evolution equations. ii. numerical, nonlinear schrödinger equation," *J. Comput. Phys.*, vol. 55, no. 2, pp. 203 – 230, 1984.

[95] F. Cooper, A. Khare, and U. Sukhatme, "Periodic solutions of nonlinear equations obtained by linear superposition," *Journal of Physics A: Mathematical and General*, vol. 35, no. 47, p. 10085, 2002.

[96] E. J. Mueller, T. L. Ho, M. Ueda, and G. Baym, "Fragmentation of bose-einstein condensates," *Phys. Rev. A*, vol. 74, p. 033612, 2006.

[97] J. Zhu, *Bogoliubov-de Gennes Method and Its Applications*. Lecture Notes in Physics, Springer International Publishing, 2016.

[98] B. Parajuli, D. Pecak, and C.-C. Chien, "Atomic boson-fermion mixtures in one-dimensional box potentials: Few-body and mean-field many-body analyses," *Phys. Rev. A*, vol. 107, p. 023308, Feb 2023.

[99] C. Chin, R. Grimm, P. Julienne, and E. Tiesinga, "Feshbach resonances in ultracold gases," *Rev. Mod. Phys.*, vol. 82, pp. 1225–1286, Apr 2010.

[100] M. Olshanii, "Atomic scattering in the presence of an external confinement and a gas of impenetrable bosons," *Phys. Rev. Lett.*, vol. 81, pp. 938–41, 1998.

[101] B. Van Schaeybroeck, P. Navez, and J. O. Indekeu, "Interface potential and line tension for bose-einstein condensate mixtures near a hard wall," *Phys. Rev. A*, vol. 105, p. 053309, 01 2022.

[102] T. N. De Silva and E. J. Mueller, "Surface tension in unitary fermi gases with population imbalance," *Phys. Rev. Lett.*, vol. 97, p. 070402, Aug 2006.

[103] S. K. Baur, S. Basu, T. N. DeSilva, and E. J. Mueller, "Theory of the normal/superfluid interface in population imbalanced fermi gases," *Phys. Rev. A*, vol. 79, p. 063628, 02 2009.

[104] B. Parajuli and C.-C. Chien, "Proximity effect and spatial kibble-zurek mechanism in atomic fermi gases with inhomogeneous pairing interactions," 2023.

[105] J. CLARKE, "The proximity effect between superconducting and normal thin films in zero field," *Journal de Physique Colloques*, vol. 29, no. C2, pp. C2–3–C2–16, 1968.

[106] G. Rai, S. Haas, and A. Jagannathan, "Proximity effect in a superconductor-quasicrystal hybrid ring," *Phys. Rev. B*, vol. 100, p. 165121, Oct 2019.

[107] G. Rai, S. Haas, and A. Jagannathan, "Superconducting proximity effect and order parameter fluctuations in disordered and quasiperiodic systems," *Phys. Rev. B*, vol. 102, p. 134211, Oct 2020.

[108] R. L. Kobes and J. P. Whitehead, "Proximity effect and the thermodynamic properties of superconducting thin films," *Phys. Rev. B*, vol. 36, pp. 121–140, Jul 1987.

[109] C.-K. Chiu, W. S. Cole, and S. Das Sarma, "Induced spectral gap and pairing correlations from superconducting proximity effect," *Phys. Rev. B*, vol. 94, p. 125304, Sep 2016.

[110] H. Yamazaki, N. Shannon, and H. Takagi, "Interplay between superconductivity and ferromagnetism in epitaxial Nb(110)Au(111)Fe(110) trilayers," *Phys. Rev. B*, vol. 73, p. 094507, Mar 2006.

[111] H. Yamazaki, N. Shannon, and H. Takagi, "Interplay between superconductivity and ferromagnetism in epitaxial nb(110)/au(111)/co(0001) trilayers," *Phys. Rev. B*, vol. 81, p. 094503, Mar 2010.

[112] G. Csire, B. Újfalussy, J. Cserti, and B. Győrffy, "Multiple scattering theory for superconducting heterostructures," *Phys. Rev. B*, vol. 91, p. 165142, Apr 2015.

[113] G. Csire, J. Cserti, I. Tüttő, and B. Újfalussy, "Prediction of superconducting transition temperatures of heterostructures based on the quasiparticle spectrum," *Phys. Rev. B*, vol. 94, p. 104511, Sep 2016.

[114] G. Csire, J. Cserti, and B. Újfalussy, "First principles based proximity effect of superconductor–normal metal heterostructures," *Journal of Physics: Condensed Matter*, vol. 28, p. 495701, oct 2016.

[115] J. C. Cuevas, J. Hammer, J. Kopu, J. K. Viljas, and M. Eschrig, "Proximity effect and multiple andreev reflections in diffusive superconductor–normal-metal–superconductor junctions," *Phys. Rev. B*, vol. 73, p. 184505, May 2006.

[116] I. Sternfeld, V. Shelukhin, A. Tsukernik, M. Karpovski, A. Gerber, and A. Palevski, "Proximity effect in granular superconductor–normal metal structures," *Phys. Rev. B*, vol. 71, p. 064515, Feb 2005.

[117] A. M. Black-Schaffer and S. Doniach, "Self-consistent solution for proximity effect and josephson current in ballistic graphene sns josephson junctions," *Phys. Rev. B*, vol. 78, p. 024504, Jul 2008.

[118] K. Komatsu, C. Li, S. Autier-Laurent, H. Bouchiat, and S. Gueron, "Superconducting proximity effect in long superconductor/graphene/superconductor junctions: From specular andreev reflection at zero field to the quantum hall regime," *Phys. Rev. B*, vol. 86, p. 115412, Sep 2012.

[119] C. Ojeda-Aristizabal, M. Ferrier, S. Guéron, and H. Bouchiat, "Tuning the proximity effect in a superconductor-graphene-superconductor junction," *Phys. Rev. B*, vol. 79, p. 165436, Apr 2009.

[120] V. J. Kauppila, H. Q. Nguyen, and T. T. Heikkilä, "Nonequilibrium and proximity effects in superconductor–normal metal junctions," *Phys. Rev. B*, vol. 88, p. 075428, Aug 2013.

[121] A. I. Buzdin, "Proximity effects in superconductor-ferromagnet heterostructures," *Rev. Mod. Phys.*, vol. 77, pp. 935–976, Sep 2005.

[122] L. Fu and C. L. Kane, "Superconducting proximity effect and majorana fermions at the surface of a topological insulator," *Phys. Rev. Lett.*, vol. 100, p. 096407, Mar 2008.

[123] T. W. B. Kibble, "Topology of cosmic domains and strings," *Journal of Physics A: Mathematical and General*, vol. 9, p. 1387, aug 1976.

[124] T. Kibble, "Some implications of a cosmological phase transition," *Physics Reports*, vol. 67, no. 1, pp. 183–199, 1980.

[125] W. H. Zurek, "Cosmological experiments in superfluid helium?," *Nature (London)*, vol. 317, no. 6037, pp. 505–508, 1985.

[126] W. Zurek, "Cosmological experiments in condensed matter systems," *Physics Reports*, vol. 276, pp. 177–221, nov 1996.

[127] P. Laguna and W. H. Zurek, "Density of kinks after a quench: When symmetry breaks, how big are the pieces?," *Phys. Rev. Lett.*, vol. 78, pp. 2519–2522, Mar 1997.

[128] P. Laguna and W. H. Zurek, "Critical dynamics of symmetry breaking: Quenches, dissipation, and cosmology," *Phys. Rev. D*, vol. 58, p. 085021, Sep 1998.

[129] J. R. Anglin and W. H. Zurek, "Vortices in the wake of rapid bose-einstein condensation," *Phys. Rev. Lett.*, vol. 83, pp. 1707–1710, Aug 1999.

[130] G. J. Stephens, L. M. A. Bettencourt, and W. H. Zurek, "Critical dynamics of gauge systems: Spontaneous vortex formation in 2d superconductors," *Phys. Rev. Lett.*, vol. 88, p. 137004, Mar 2002.

[131] J. Dziarmaga, "Dynamics of a quantum phase transition: Exact solution of the quantum ising model," *Phys. Rev. Lett.*, vol. 95, p. 245701, Dec 2005.

[132] J. Dziarmaga, M. M. Rams, and W. H. Zurek, "Coherent many-body oscillations induced by a superposition of broken symmetry states in the wake of a quantum phase transition," *Physical Review Letters*, vol. 129, dec 2022.

[133] J. Dziarmaga, "Dynamics of a quantum phase transition and relaxation to a steady state," *Advances in physics*, vol. 59, no. 6, pp. 1063–1189, 2010.

[134] D. Jaschke, K. Maeda, J. D. Whalen, M. L. Wall, and L. D. Carr, "Critical phenomena and kibble–zurek scaling in the long-range quantum ising chain," *New Journal of Physics*, vol. 19, p. 033032, mar 2017.

[135] A. Polkovnikov, "Universal adiabatic dynamics in the vicinity of a quantum critical point," *Phys. Rev. B*, vol. 72, p. 161201, Oct 2005.

[136] B. Damski, "The simplest quantum model supporting the kibble-zurek mechanism of topological defect production: Landau-zener transitions from a new perspective," *Phys. Rev. Lett.*, vol. 95, p. 035701, Jul 2005.

[137] G. L. Warner and A. J. Leggett, "Quench dynamics of a superfluid fermi gas," *Phys. Rev. B*, vol. 71, p. 134514, Apr 2005.

[138] W. H. Zurek, U. Dorner, and P. Zoller, "Dynamics of a quantum phase transition," *Phys. Rev. Lett.*, vol. 95, p. 105701, Sep 2005.

[139] K. Shimizu, Y. Kuno, T. Hirano, and I. Ichinose, "Dynamics of a quantum phase transition in the bose-hubbard model: Kibble-zurek mechanism and beyond," *Phys. Rev. A*, vol. 97, p. 033626, Mar 2018.

[140] F. M. Cucchietti, B. Damski, J. Dziarmaga, and W. H. Zurek, "Dynamics of the bose-hubbard model: Transition from a mott insulator to a superfluid," *Phys. Rev. A*, vol. 75, p. 023603, Feb 2007.

[141] J. Dziarmaga, M. Tylutki, and W. H. Zurek, "Quench from mott insulator to superfluid," *Phys. Rev. B*, vol. 86, p. 144521, Oct 2012.

[142] B. Gardas, J. Dziarmaga, and W. H. Zurek, "Dynamics of the quantum phase transition in the one-dimensional bose-hubbard model: Excitations and correlations induced by a quench," *Phys. Rev. B*, vol. 95, p. 104306, Mar 2017.

[143] Y. Machida and K. Kasamatsu, "Application of the inhomogeneous kibble-zurek mechanism to quench dynamics in the transition from a mott insulator to a superfluid in a finite system," *Phys. Rev. A*, vol. 103, p. 013310, Jan 2021.

[144] M. Anquez, B. A. Robbins, H. M. Bharath, M. Boguslawski, T. M. Hoang, and M. S. Chapman, "Quantum kibble-zurek mechanism in a spin-1 bose-einstein condensate," *Phys. Rev. Lett.*, vol. 116, p. 155301, Apr 2016.

[145] R. Monaco, J. Mygind, and R. J. Rivers, "Zurek-kibble domain structures: The dynamics of spontaneous vortex formation in annular josephson tunnel junctions," *Phys. Rev. Lett.*, vol. 89, p. 080603, Aug 2002.

[146] S. Ulm, J. Rossnagel, G. Jacob, C. Deguenther, S. T. Dawkins, U. G. Poschinger, R. Nigmatullin, A. Retzker, M. B. Plenio, F. Schmidt-Kaler, and K. Singer, "Observation of the kibble-zurek scaling law for defect formation in ion crystals," *Nature communications*, vol. 4, no. 1, pp. 2290–2290, 2013.

[147] K. Pyka, J. Keller, H. L. Partner, R. Nigmatullin, T. Burgermeister, D. M. Meier, K. Kuhlmann, A. Retzker, M. B. Plenio, W. H. Zurek, A. del Campo, and T. E. Mehlstaeubler, "Topological defect formation and spontaneous symmetry breaking in ion coulomb crystals," *Nature communications*, vol. 4, no. 1, pp. 2291–2291, 2013.

[148] N. Navon, A. L. Gaunt, R. P. Smith, and Z. Hadzibabic, "Critical dynamics of spontaneous symmetry breaking in a homogeneous bose gas," *Science*, vol. 347, no. 6218, pp. 167–170, 2015.

[149] S. Braun, M. Friesdorf, S. S. Hodgman, M. Schreiber, J. P. Ronzheimer, A. Riera, M. del Rey, I. Bloch, J. Eisert, and U. Schneider, "Emergence of coherence and the dynamics of quantum phase transitions," *Proceedings of the National Academy of Sciences*, vol. 112, no. 12, pp. 3641–3646, 2015.

[150] D. Chen, M. White, C. Borries, and B. DeMarco, "Quantum quench of an atomic mott insulator," *Phys. Rev. Lett.*, vol. 106, p. 235304, Jun 2011.

[151] A. Keesling, A. Omran, H. Levine, H. Bernien, H. Pichler, S. Choi, R. Samajdar, S. Schwartz, P. Silvi, S. Sachdev, P. Zoller, M. Endres, M. Greiner, V. Vuletic, and M. D. Lukin, "Quantum kibble-zurek mechanism and critical dynamics on a programmable rydberg simulator," *Nature*, vol. 568, no. 7751, pp. 207–211, 2019.

[152] M. Anquez, B. A. Robbins, H. M. Bharath, M. Boguslawski, T. M. Hoang, and M. S. Chapman, "Quantum kibble-zurek mechanism in a spin-1 bose-einstein condensate," *Phys. Rev. Lett.*, vol. 116, p. 155301, Apr 2016.

[153] B. W. Li, Y. K. Wu, Q. X. Mei, R. Yao, W. Q. Lian, M. L. Cai, Y. Wang, B. X. Qi, L. Yao, L. He, Z. C. Zhou, and L. M. Duan, "Probing critical behavior of long-range transverse-field ising model through quantum kibble-zurek mechanism," 2022.

[154] S. Deutschländer, P. Dillmann, G. Maret, and P. Keim, "Kibble–zurek mechanism in colloidal monolayers," *Proceedings of the National Academy of Sciences*, vol. 112, no. 22, pp. 6925–6930, 2015.

[155] B. Ko, J. W. Park, and Y. Shin, "Kibble-zurek universality in a strongly interacting fermi superfluid," *Nature physics*, vol. 15, no. 12, pp. 1227–1231, 2019.

[156] X.-P. Liu, X.-C. Yao, Y. Deng, Y.-X. Wang, X.-Q. Wang, X. Li, Q. Chen, Y.-A. Chen, and J.-W. Pan, "Dynamic formation of quasicondensate and spontaneous vortices in a strongly interacting fermi gas," *Phys. Rev. Res.*, vol. 3, p. 043115, Nov 2021.

[157] C. C. Chien and B. Damski, "Dynamics of a quantum quench in an ultracold atomic bcs superfluid," *Phys. Rev. A*, vol. 82, p. 063616, 2010.

[158] C. C. Chien, "Spatially varying interactions induced in ultra-cold atoms by optical feshbach resonance," *Phys. Lett. A*, vol. 376, p. 729, 2012.

[159] A. J. Leggett, "Diatomic molecules and Cooper pairs," in *Modern Trends in the Theory of Condensed Matter*, (Berlin), pp. 13–27, Springer-Verlag, 1980.

[160] P. M. Chaikin and T. C. Lubensky, *Principles of Condensed Matter Physics*. Cambridge: Cambridge University Press, 1995.

[161] R. Onofrio, "Cooling and thermometry of atomic fermi gases," *Phys.-Uspekhi.*, vol. 59, pp. 1129–1153, nov 2016.

[162] I. Ferrier-Barbut, M. Delehaye, S. Laurent, A. T. Grier, M. Pierce, B. S. Rem, F. Chevy, and C. Salomon, "A mixture of bose and fermi superfluids," *Science*, vol. 345, no. 6200, pp. 1035–1038, 2014.

[163] P. O. Fedichev, Y. Kagan, G. V. Shlyapnikov, and J. T. M. Walraven, "Influence of nearly resonant light on the scattering length in low-temperature atomic gases," *Phys. Rev. Lett.*, vol. 77, pp. 2913–2916, Sep 1996.

[164] F. K. Fatemi, K. M. Jones, and P. D. Lett, "Observation of optically induced feshbach resonances in collisions of cold atoms," *Phys. Rev. Lett.*, vol. 85, pp. 4462–4465, Nov 2000.

[165] M. Theis, G. Thalhammer, K. Winkler, M. Hellwig, G. Ruff, R. Grimm, and J. H. Denschlag, "Tuning the scattering length with an optically induced feshbach resonance," *Phys. Rev. Lett.*, vol. 93, p. 123001, Sep 2004.

[166] D. M. Bauer, M. Lettner, C. Vo, G. Rempe, and S. Dürr, "Control of a magnetic feshbach resonance with laser light," *Nature Physics*, vol. 5, pp. 339–342, apr 2009.

[167] L. W. Clark, L.-C. Ha, C.-Y. Xu, and C. Chin, "Quantum dynamics with spatiotemporal control of interactions in a stable bose-einstein condensate," *Phys. Rev. Lett.*, vol. 115, p. 155301, Oct 2015.

[168] G. Theocharis, P. Schmelcher, P. G. Kevrekidis, and D. J. Frantzeskakis, "Matter-wave solitons of collisionally inhomogeneous condensates," *Phys. Rev. A*, vol. 72, p. 033614, Sep 2005.

[169] G. Theocharis, P. Schmelcher, P. G. Kevrekidis, and D. J. Frantzeskakis, "Dynamical trapping and transmission of matter-wave solitons in a collisionally inhomogeneous environment," *Phys. Rev. A*, vol. 74, p. 053614, Nov 2006.

[170] P. Niarchou, G. Theocharis, P. G. Kevrekidis, P. Schmelcher, and D. J. Frantzeskakis, "Soliton oscillations in collisionally inhomogeneous attractive bose-einstein condensates," *Phys. Rev. A*, vol. 76, p. 023615, Aug 2007.

[171] A. S. Rodrigues, P. G. Kevrekidis, M. A. Porter, D. J. Frantzeskakis, P. Schmelcher, and A. R. Bishop, "Matter-wave solitons with a periodic, piecewise-constant scattering length," *Phys. Rev. A*, vol. 78, p. 013611, Jul 2008.

[172] N. Arunkumar, A. Jagannathan, and J. E. Thomas, "Designer spatial control of interactions in ultracold gases," *Phys. Rev. Lett.*, vol. 122, p. 040405, Feb 2019.

[173] A. Di Carli, G. Henderson, S. Flannigan, C. D. Colquhoun, M. Mitchell, G.-L. Oppo, A. J. Daley, S. Kuhr, and E. Haller, "Collisionally inhomogeneous bose-einstein condensates with a linear interaction gradient," *Phys. Rev. Lett.*, vol. 125, p. 183602, Oct 2020.

[174] D. Mitra, P. T. Brown, E. Guardado-Sanchez, S. S. Kondov, T. Devakul, D. A. Huse, P. Schauss, and W. S. Bakr, "Quantum gas microscopy of an attractive fermi-hubbard system," *Nature physics*, vol. 14, no. 2, pp. 173–177, 2018.

[175] J. Koepsell, S. Hirthe, D. Bourgund, P. Sompet, J. Vijayan, G. Salomon, C. Gross, and I. Bloch, "Robust bilayer charge pumping for spin- and density-resolved quantum gas microscopy," *Phys. Rev. Lett.*, vol. 125, p. 010403, Jul 2020.

[176] T. Hartke, B. Oreg, N. Jia, and M. Zwierlein, "Doublon-hole correlations and fluctuation thermometry in a fermi-hubbard gas," *Phys. Rev. Lett.*, vol. 125, p. 113601, Sep 2020.

[177] T. Hartke, B. Oreg, C. Turnbaugh, N. Jia, and M. Zwierlein, "Direct observation of non-local fermion pairing in an attractive fermi-hubbard gas," *arXiv preprint arXiv:2208.05948*, 2022.

[178] S. Gupta, Z. Hadzibabic, M. W. Zwierlein, C. A. Stan, K. Dieckmann, C. H. Schunck, E. G. M. van Kempen, B. J. Verhaar, and W. Ketterle, "Radio-

frequency spectroscopy of ultracold fermions," *Science*, vol. 300, no. 5626, pp. 1723–1726, 2003.

[179] C. H. Schunck, Y. Shin, A. Schirotzek, M. W. Zwierlein, and W. Ketterle, "Pairing without superfluidity: The ground state of an imbalanced fermi mixture," *Science*, vol. 316, no. 5826, pp. 867–870, 2007.

[180] B. Mukherjee, P. B. Patel, Z. Yan, R. J. Fletcher, J. Struck, and M. W. Zwierlein, "Spectral response and contact of the unitary fermi gas," *Phys. Rev. Lett.*, vol. 122, p. 203402, May 2019.

[181] Z. Yan, P. B. Patel, B. Mukherjee, R. J. Fletcher, J. Struck, and M. W. Zwierlein, "Boiling a unitary fermi liquid," *Phys. Rev. Lett.*, vol. 122, p. 093401, Mar 2019.